GLACIAL-INTERGLACIAL CLIMATE VARIABILITY IN THE NORTH AMERICAN

SOUTHERN GREAT PLAINS FROM STABLE ISOTOPES IN

A TEXAS STALAGMITE

A Thesis

by

ELLEN ROSEMARY BARTOW-GILLIES

Submitted to the Office of Graduate and Professional Studies of
Texas A&M University
in partial fulfillment of the requirements for the degree of

MASTER OF SCIENCE

Chair of Committee,	E. Brendan Roark
Committee Members,	Franco Marcantonio
	Robert Korty
Head of Department,	David Cairns

August 2018

Major Subject: Geography

ABSTRACT

In the US Southern Great Plains (SGP), projections of changes in rainfall under future warming scenarios differ greatly in their sign and intensity. The lack of continuous, well-dated paleoclimate records before the Last Glacial Maximum (LGM) hinders a comprehensive understanding of past variability in regional hydroclimate patterns. We present three absolutely U/Th-dated oxygen and carbon isotope records from a calcite stalagmite collected near Georgetown, Texas (Cobbs Cavern at 30°N, 98°W), spanning 350 to 3800 years before present (BP), 98 to 130 kyr BP, and 179 to 208 kyr BP. Based on our two-year dataset of central Texas precipitation and Cobbs Cavern dripwaters, we interpret the oxygen isotopic composition of the stalagmite to reflect variability in regional rainwater $\delta^{18}O$ composition through time, which we determine is largely driven by amount of precipitation and storm structure. There is no evidence for kinetic isotope effects in the stalagmite, so we conclude that more negative $\delta^{18}O$ values reflect wetter conditions with larger and more organized storms, whereas more positive $\delta^{18}O$ values reflect drier conditions with unorganized, sporadic storms. Stalagmite $\delta^{13}C$ variations may be driven by shifts in overlying vegetation type, soil bioproductivity, karst flow rate variability, and prior calcite precipitation such that more negative $\delta^{13}C$ values reflect increased moisture availability in the region. The stalagmite records include Marine Isotope Stage (MIS) 5e, a period where global temperatures may have been as much as 2°C warmer and sea level 4-6 m higher than present. Thus, our $\delta^{18}O$ record provides context for how SGP hydroclimate may respond to future warming. Prominent features in the $\delta^{18}O$ record, including a wet MIS 5e appear to be paced by precession, with the timing of $\delta^{18}O$ minima (maxima) broadly consistent with that of maxima (minima) in summer insolation at 30°N. Our SGP stalagmite records shed light on the

fundamental character of SGP hydroclimate response to glacial-interglacial forcings, and provide

evidence for increased precipitation and persistent convective storm activity under past warming

conditions.

DEDICATION

To Grandmama, who taught me how to balance grit with grace.

ACKNOWLEDGEMENTS

CONTRIBUTORS AND FUNDING SOURCES

NOMENCLATURE

SGP   Southern Great Plains

BP   Before Present

LMWL   Local Meteoric Water Line

GoM   Gulf of Mexico

NH   Northern Hemisphere

MCS   Mesoscale Convective System

MIS   Marine Isotope Stage

IPCC   Intergovernmental Panel on Climate Change

EAM   East Asian Monsoon

NARCCAP   North American Regional Climate Change Assessment Program

GCM   Global Circulation Model

NOAA   National Oceanic and Atmospheric Administration

LLJ   Low-Level Jet

GPLLJ   Great Plains Low-Level Jet

ENSO   El Niño Southern Oscillation

PDO   Pacific Decadal Oscillation

ITCZ   Intertropical Convergence Zone

MAT   Mean Annual Temperature

LGM   Last Glacial Maximum

PCP   Prior Calcite Precipitation

RSL   Relative Sea Level

TABLE OF CONTENTS

LIST OF FIGURES

LIST OF TABLES

CHAPTER I

INTRODUCTION AND OBJECTIVES

1.1 Introduction

In the US Southern Great Plains (SGP), long-term rainfall variability beyond the instrumental record remains poorly understood due to a lack of regional paleoclimate archives. The future health and success of this region, which is home to a substantial number of major metropolitan areas as well as important agricultural and grazing lands, depends on a clearer understanding of the mechanisms driving regional hydroclimate variability. Water stress is already an imminent threat to the region due to rapid depletion of aquifers and the limited irrigation systems already in place (Kunkel et al. 2013). Understanding crop sensitivity to a range of climatic conditions requires a better grasp of regional climate patterns to avoid economic disaster and mitigate the potentially deleterious effects of a changing climate. The last ~150 years of the instrumental climate record do not provide enough data to fully understand regional hydroclimate variability over decadal and longer time scales. Furthermore, the scarcity of paleoclimate information from the SGP that is available before the Last Glacial Maximum (LGM) limits our understanding of regional climate responses to changes in mean climate state and forcing. Despite the socio-economic significance of the SGP, changes in precipitation patterns resulting from variations in mean state and anthropogenic climate change are not well constrained, yet the sustained ecological and economic success of this region depends on a better understanding of natural variations in the region's climate.

Based on the Palmer Drought Severity Index, in 2011 the Great Plains region experienced the most severe drought ever recorded in the region (NOAA 2011), and the 2011 summer in

Texas was the warmest and driest on record (Kunkel et al. 2013). The SGP often experiences intense flooding, often a result of hurricane systems from the Gulf of Mexico or major convective storms that release huge amounts of precipitation in a short amount of time, thus overwhelming infrastructure (Kunkel et al. 2013). Texas averages about 0.8 tropical storms on its coastline each year; half of which are hurricane systems, and the other half are tropical storms (Roth 2010). These tropical cyclone systems that originate from the Gulf of Mexico can penetrate into the Great Plains region and trigger massive rainfall events over large areas (Kunkel et al. 2013). Flooding can also result from winter snowmelt or long-lasting heavy precipitation that induces river overflow (Kunkel et al. 2013). These flood events are costly, as Wang et al. (2015) attributed over $45 million in property and agricultural damages to the 2015-2016 SGP floods. From 1980 to 2003, six major drought and flooding events in the Great Plains contributed to a total loss of $131.7 billion (Basara et al. 2013). These weather events triggered price surges ultimately borne by American consumers. Understanding climate variability in this region is vital to preparing for a safe, stable, and productive future.

Studying the stable oxygen isotopic makeup of rainfall can reveal information on past variability in the hydrologic cycle of a region (Dansgaard 1964; Merlivat and Jouzel 1979). A plethora of potential climate-based proxy archives exist, ranging from tree rings to sediment cores to speleothem records. The karst geology present throughout the SGP lends itself to the use of cave deposit records as a means of studying past hydroclimate patterns in the region. Uranium-thorium (U/Th) dating can be used to date speleothems, and the isotopic composition of these cave deposits can then be tied to a high-resolution chronology to reveal past variations in climate conditions (Lachniet 2009; Shen et al. 2002).

We have generated a long-term speleothem record in tandem with complementary local rainfall records in order to fill the long-term paleorainfall data gap that exists in the SGP region. In Chapter 2, we present an oxygen ($\delta^{18}O$) and deuterium (δD) stable isotope analysis of Cobbs Cavern dripwater and ~2 years of rainwater from nearby Austin to constrain the climatic interpretation of our speleothem record. We used the Austin precipitation dataset to investigate the relationship between $\delta^{18}O$ and δD to air temperature and the amount of precipitation. This allowed us to determine what is a principal driver of large changes of $\delta^{18}O$ variability in Texas rainwater, and ultimately, speleothem-forming dripwater.

In Chapter 3, we examined the paleoclimate history of the SGP using three U-series dated speleothem oxygen and carbon records from an undisturbed, closed-system cave, Cobbs Cavern, nestled in the Edwards Plateau limestone of central Texas. The U/Th dates indicate speleothem growth from 350 to 3800 years before present (BP), from 98,000 to 130,000 years BP, and from 179,000 to 209,000 years BP. In this study we chose to emphasize the Eemian Interglacial, known as Marine Isotope Stage 5e (MIS 5e), which peaked ~125,000 years BP. During MIS 5e, global temperatures were as much as 2°C warmer, (Shackleton 2002), sea level was 4-6m higher (Bard et al. 1990), and ice sheets were less extensive (Cuffey and Marshall 2000) than present. MIS 5e could thus serve as an analogue for future warming scenarios, highlighted in the Fifth IPCC Report (IPCC 2014) in the SGP region. We used our long-term, paleorainfall speleothem record to compare past rainfall variability during interglacial conditions to modern climate conditions to contribute to the body of knowledge that may aid climate modelers as they work to generate models on how SGP hydroclimate may vary under future conditions of climate change.

1.2 Research objectives

Three temporally distinct stalagmite records from Cobbs Cavern in the central Texas are used in this project. The first, oldest record extends from 209 to 179 kyr BP, the second spans 130 to 98 kyr BP while the youngest record is from the late Holocene and extends from ~3800 to 350 yrs BP. The stalagmite isotopic records, complemented by a 2-year record of local rainfall analysis, are generally interpreted within the context of variations in climate, such that the speleothem oxygen isotopic composition reflects variations in precipitation.

In Chapter 2, we identified what drives $\delta^{18}O$ variability in Texas rainwater and determine if cave dripwater isotopic makeup reflects that of the local precipitation. We also worked to clarify modern hydroclimate dynamics of the SGP and the potential isotope effects that may influence $\delta^{18}O$ variability in Texas precipitation, including the amount of rainfall, air temperature, altitude, continentality, seasonality, storm type, and global ice volume effects. In Chapter 3, we first ensured that our stalagmite calcite is reliably recording dripwater $\delta^{18}O$ and ultimately rainwater $\delta^{18}O$ values. We then investigated the potential controls on variability in the $\delta^{18}O$ of our speleothem record and how this variability has changed throughout different temporal intervals over the last 209 kyr BP. Finally, we compared modern conditions (~350 yr BP) to past interglacial (MIS 5e) conditions in order to consider how rainfall variability may change in the region in response to predicted anthropogenic warming and calculated rises in Northern Hemisphere (NH) insolation.

1.3 References

Bard, E., Hamelin, E., and R.G. Fairbanks. 1990. U-Th ages obtained by mass spectrometry in corals from Barbados: sea level during the past 130,000 years, *Nature* 346: 456-58.

Basara, J. B., J. N. Maybourn, C. M. Peirano, J. E. Tate, P. J. Brown, J. D. Hoey, and B. R. Smith. 2013. Drought and associated impacts in the Great Plains of the United States—A review, *International Journal of Geosciences* 4: 72–81.

Cuffey, K.M. and S.J. Marshall. 2000. Substantial contribution to sea-level rise during the last interglacial from the Greenland ice sheet, *Nature* 404: 591-94.

Dansgaard, W. 1964. Stable isotopes in precipitation, *Tellus* 16(4): 436–468.

IPCC, 2014: Climate Change 2014: Synthesis Report. Contribution of Working Groups I, II and III to the Fifth Assessment Report of the Intergovernmental Panel on Climate Change [Core Writing Team, R.K. Pachauri and L.A. Meyer (eds.)]. IPCC, Geneva, Switzerland, 151 pp.

Kunkel, K. E. et al. 2013. Regional Climate Trends and Scenarios for the U.S. National Climate Assessment Part 4. Climate of the U.S. Great Plains, NOAA Technical Report NESDIS 142-4: 1–91.

Lachniet, M. S. 2009. Climatic and environmental controls on speleothem oxygen isotope values, *Quaternary Science Reviews* 28(5-6): 412–432.

Merlivat, L. and Jouzel, J. 1979. Global climatic interpretation of the deuterium-oxygen 18 relationship for precipitation, *Journal of Geophysical Research* 84: 5029-33.

NOAA. 2011. State of the Climate: Drought August 2011, available online at http://www.ncdc.noaa.gov/sotc/drought/2011/8.

Roth, D. 2010. Texas Hurricane History. National Weather Service Report.

Shackleton, N. J., F. Sánchez-Goñi, D. Pailler, and Y. Lancelot. 2002. Marine Isotope Substage 5e and the Eemian Interglacial, *Global and Planetary Change* 36:151-155.

Shen, C.-C., Edwards, R.L., Cheng, H., Dorale, J.A., Thomas, R.B., Bradley Moran, S., Weinstein, S.E., and H.N. Edmonds. 2002. Uranium and thorium isotopic and concentration measurements by magnetic sector inductively coupled plasma mass spectrometry, *Chemical Geology* 185: 165–178.

Wang, S. S., W. R. Huang, and H. H. Hsu (2015), Role of the strengthened El Niño t eleconnection in the May 2015 floods over the southern Great Plains, *Geophysical Research Letters* 1944-8007.

CHAPTER II

MODERN TEXAS RAINWATER AND CAVE DRIPWATER RECORDS

2.1 Introduction

Oxygen and hydrogen isotopes in water leave an identifiable signature on water mass movement, and can be used as natural tracers of the hydrologic cycle. Cave deposits, known as speleothems, can serve as recorders of past rainfall isotope variability because speleothem calcite $\delta^{18}O$ values are controlled by dripwater $\delta^{18}O$ under conditions of equilibrium deposition. Consequently, cave dripwater isotopic composition is a reflection of rainwater isotopic composition influenced by identifiable isotope effects. Clarifying the potential isotopic effects, including amount, temperature, seasonality, and continentality, that are at play in a particular region can help identify what drives local precipitation $\delta^{18}O$ variability. In mid-latitudes such as the Southern Great Plains (SGP), the amount of precipitation in a particular rain event is a known driver of $\delta^{18}O$ isotope variability in rainfall (Wong et al. 2015). This study seeks to further investigate drivers of $\delta^{18}O$ variability in central Texas rainwater.

Longitudinal stable isotope studies of rainfall are needed to constrain how the hydrologic system of the SGP has changed in the past. This data will reinforce paleoclimate interpretations by establishing a link between the modern and the past. Here we analyze ~2 years of collected rainfall data from Austin, Texas, a location that acts as a good analog for rainfall at the nearby Cobbs Cavern. Furthermore, this chapter complements the next chapter ("Late Pleistocene and Holocene Climate Inferred from Stable Isotopes in a Texas Stalagmite"), because rainwater percolates through the overlying karst area to ultimately form speleothem calcite, which then reflects the isotopic makeup of the precipitation (Lachniet 2009). Therefore, speleothem records

are an important paleoclimate archive that, when paired with a high-resolution time series, allow

for the long-term reconstructions of hydroclimate variability.

Our Austin rainfall and Cobbs Cavern dripwater data is used to interpret the climatological

controls on variability in rainfall $\delta^{18}O$ at the study site. By clarifying what drives $\delta^{18}O$ variability

in Texas and the greater SGP region rainfall, we can then provide a more detailed and robust

interpretation of past SGP hydroclimate variability from our speleothem record. Elucidating past

variability of rainfall patterns in this region of tremendous economic and agricultural importance

will improve predictions of future extreme weather events in a changing climate.

2.2 Background and setting

2.2.1 Texas setting and hydroclimate

Both Cobbs Cavern and our Austin rainfall collection site are located on the Edwards

Plateau in Central Texas, which forms the base of the SGP. The entire Great Plains region

experiences a wide range of precipitation variability, with the southern half experiencing greater

precipitation variability than the northern half of the Great Plains (Kunkel et al. 2013). In Texas,

there is a general pattern of seasonality in rainfall amount despite a high degree of interannual

rainfall variability. Likewise, Texas temperatures generally peak in the late summer months and

are distinctly seasonal; peak precipitation occurs in late boreal spring (May) and fall (Sept to

Oct) (**Figure 2.1**).

Bimodal peaks in rainfall amount generally occur in rainy years, but are not typically

observed in dry or drought years (**Figure 2.2**). In rainy years, rainwater soaks into the ground

and eventually makes its way down into the karst system. The isotopic makeup of speleothems is

likely driven by rainy years in which large, organized storms including mesoscale convective systems (MCSs) and multicell line storms (squall lines) deliver the largest amounts of precipitation to the SGP. MCSs account for 30 to 70% of yearly warm season precipitation to the Great Plains region (Fritsch et al. 1986).

Several mechanisms fuel convective system formation in the SGP. During spring and fall, cold dry air is pulled into central Texas by the polar jet stream, which can deliver fronts to the region (**Figure 2.3**). This dry air mass collides with humid Gulf of Mexico air, which is funneled onto land by the western arm of the Bermuda High system. This mixing of humid and dry air masses generates severe convective storms that release large amounts of rainfall onto the SGP region, with moisture derived from the Gulf of Mexico (Nativ and Riggio, 1990). A second mechanism is due to elevation-based differential cooling between the Rocky Mountains and the SGP, which leads to the formation of the Great Plain low-level jet (LLJ) from differences in pressure. Air is forced up in elevation during transit from the flat Great Plains region to the Rocky Mountains, resulting in decreased atmospheric stability and increased chances of surface convergence, which often results in MCS formation (Kumjian 2006). These mechanisms of storm generation result in peak precipitation amounts in late spring and early fall (**Figure 2.1**).

In the summer, a strong, largely stationary mid and upper level anticyclone sits over the region, which reduces instability in the region and generally prevents rain events, except for the occasional tropical or subtropical disturbance. In Northern Hemisphere (NH) winter, humid air from the Gulf of Mexico is less pervasive and there is less precipitation. Year-round moisture comes from the Gulf of Mexico because a strong high-pressure area exists just west of the SGP, which, combined with the western border of the Rocky Mountains, prevents Pacific moisture from reaching the region (Elliot 1949). Furthermore, the lack of topographic barriers in the SGP

and a common source of SGP moisture from the Gulf of Mexico largely explain the similarity

among SGP rainfall events (Nielsen-Gammon 2011) because air masses can easily travel through

the SGP region. Thus, precipitation variability that occurs in south central Texas is highly

correlated with rainfall variability that occurs in the broader SGP region. The spatial correlation

of modern precipitation throughout the SGP suggests that our speleothem record will be a robust

recorder of past hydroclimate variability for the entire SGP region.
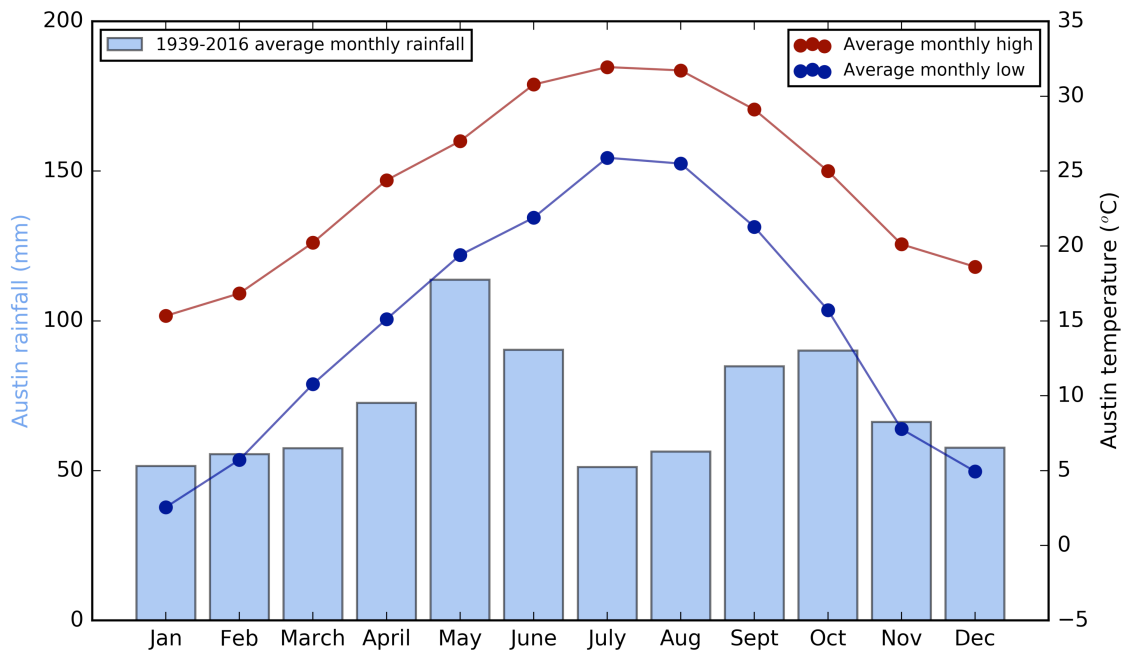
Figure 2.1. Monthly Texas precipitation (blue bars) and temperature (red and blue points). 1939-2016 monthly dataset from Camp Mabry in Austin, TX (Western Regional Climate Center 2017).
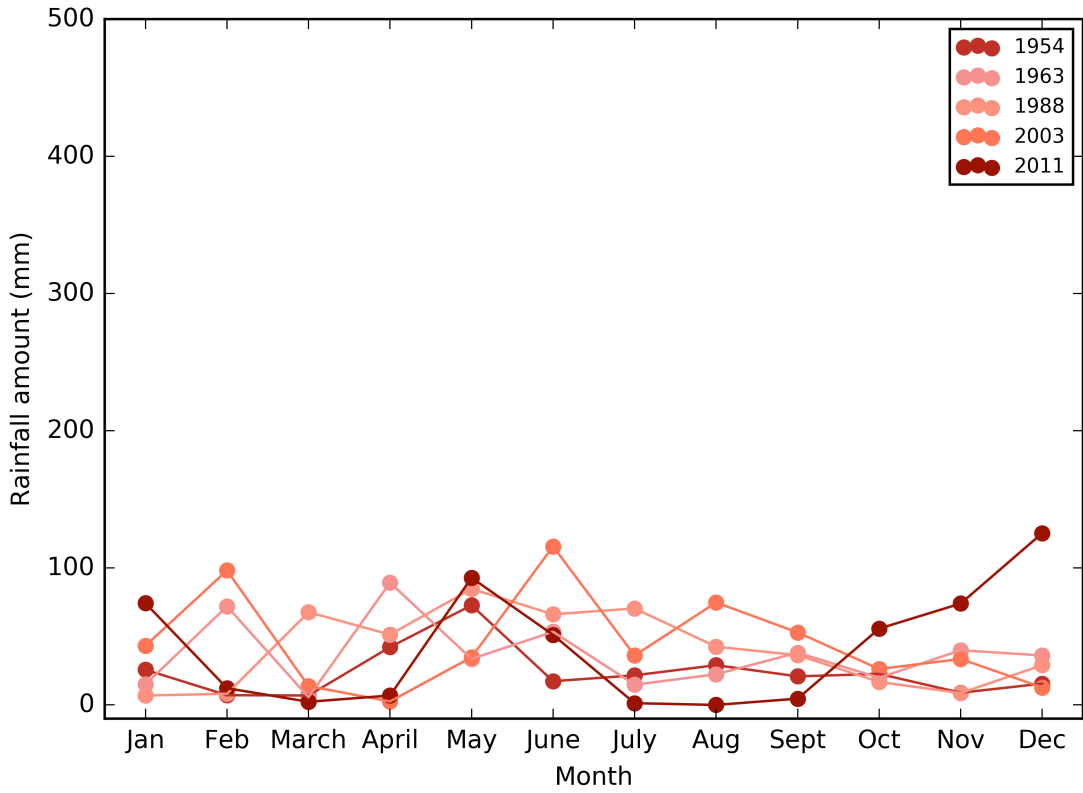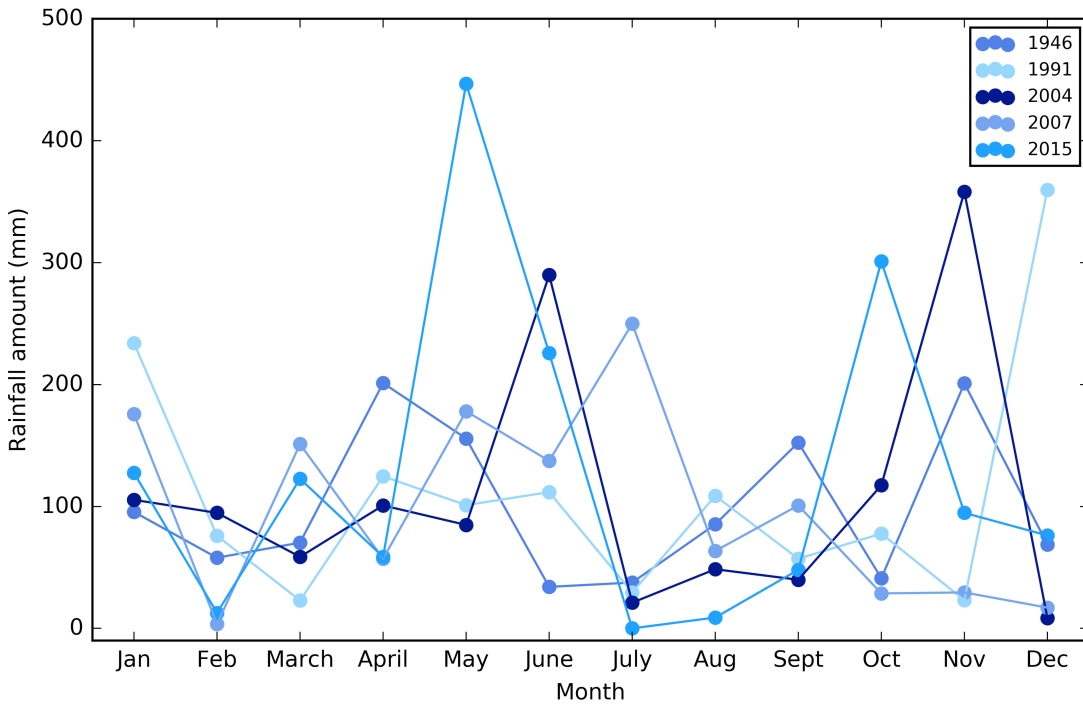
Figure 2.2. Bimodal Texas rainfall. Monthly rainfall amount of the 5 driest years with no observable bimodal peaks (A) and 5 wettest years with observable peaks in late spring and fall (B) from the Camp Mabry precipitation dataset (Western Regional Climate Center, 2017).

10
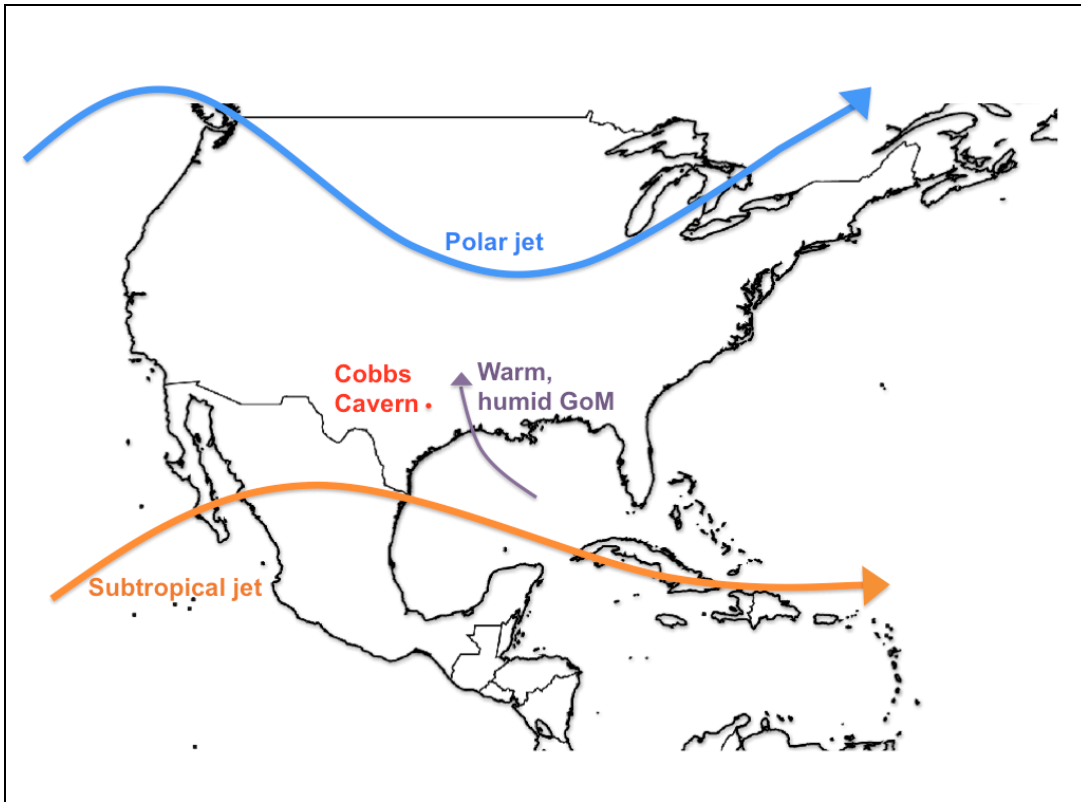
Figure 2.3. Southern Great Plains (SGP) climate schematic. The polar jet (blue) delivers cold, dry air masses to the SGP that lift humid air from the Gulf of Mexico (purple) to form convective storms. The Gulf of Mexico air is funneled onto land by the western branch of the Bermuda High.

2.2.2 Cobbs Cavern in central Texas

Cobbs Cavern, located in Williamson County Texas (**Figure 2.4**, 30.5° N, 97.75° W), 30 miles north of Austin, is a part of the Balcones Escarpment on the Edwards Plateau, which forms the base of the Great Plains region. The Edwards Plateau is sandwiched between the Texas High Plains and ultimately the Rocky Mountains to the west, and the Mississippi River Valley to the east. At Cobbs Cavern, the water that infiltrates the cave and forms speleothems is primarily sourced from SGP rainwater that has soaked into the ground above the karst area rather than from regional groundwater.

11
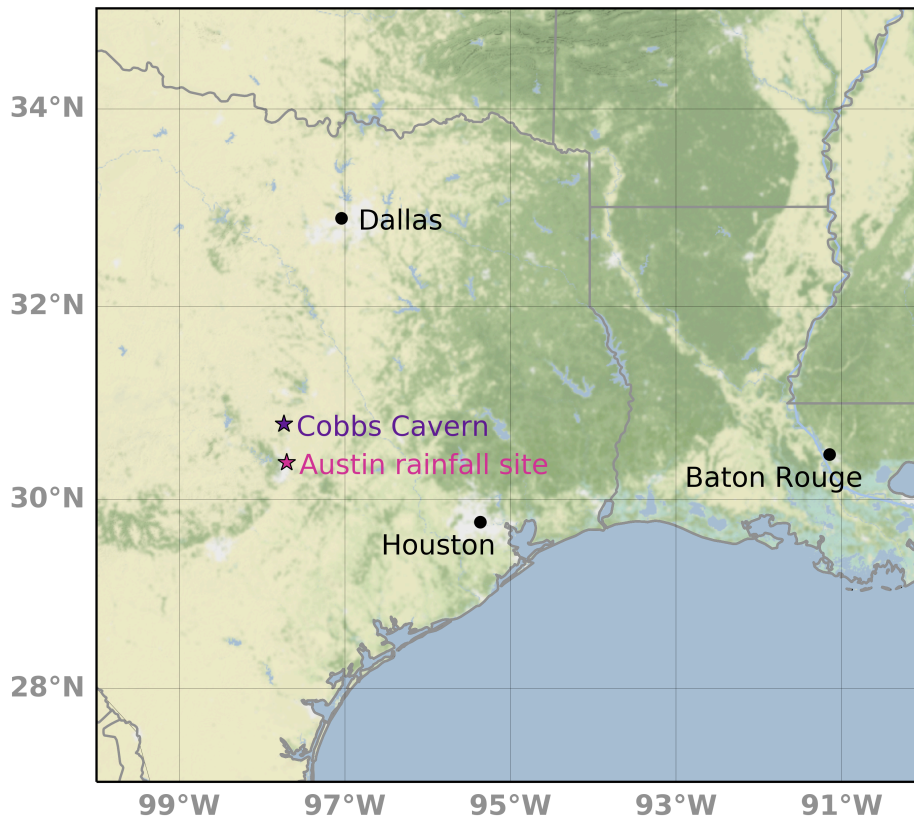
Figure 2.4. Location of study area. Cobbs Cavern shown in purple and Austin rainfall collection site in south central Texas.

2.2.3 Stable isotopes in rainwater and dripwater

The stable isotopes of deuterium (D), oxygen-18 (^{18}O) and oxygen-16 (^{16}O) can be used to track water as it moves through the water cycle. The abundance of each isotope is measured and expressed relative to an established standard in per mil (‰) units. The original standard was called "standard mean ocean water," or SMOW (Craig 1961) but has since been updated to Vienna SMOW (VSMOW). The ratio of stable water isotopes is denoted as δD for deuterium, the ratio of $H_2{}^{16}O$ to $^2H_2{}^{16}O$, and $δ^{18}O$ for oxygen, the ratio of the heavier oxygen isotope (^{18}O) to the lighter (^{16}O). The most abundant oxygen isotope is ^{16}O, which makes up 99.76% of all

stable oxygen isotopes; with a relative proportion of 0.2%, ^{18}O is the second most abundant

oxygen isotope followed by ^{17}O at 0.04% (Bradley 2015). ^{17}O is not useful for the purposes of

this study and is thus left out of further discussion. With the hydrogen component, there are two

stable isotopes. ^{1}H is most abundant at 99.984% followed by ^{2}H (deuterium) at 0.016% (Bradley

2015).

As water evaporates from a body of water, the vapor is more depleted in deuterium and

^{18}O (the heavier isotopes) than the water left behind, which is now relatively enriched in

deuterium and ^{18}O. Yet as this vapor condenses, the lower vapor pressure of the heavier isotopes

means they will preferentially be converted from vapor to liquid state than H_2O comprising the

lighter isotopes; thus, relative to the vapor, the condensation will be enriched in deuterium and

^{18}O (Dansgaard 1961). This process continues such that repeated cooling will produce

condensate with lower and lower heavy isotope concentrations than the initial concentrations.

This is known as Rayleigh distillation (Dansgaard 1964). Therefore, mass differences due to

potential combinations of oxygen and hydrogen isotopes result in distinct fractionation rates that

can reveal clues about the history and origin of rainwater.

2.2.4 Relevance of precipitation composition to speleothem science

To investigate what controls δ^{18}O variability in our records, we must first determine what

drives δ^{18}O variability in Texas precipitation, which is the source of our cave dripwater. If

speleothem calcite forms in isotopic equilibrium, its δ^{18}O value likely reflects rainwater δ^{18}O and

cave temperature (Lachniet 2009). A range of factors can influence the δ^{18}O of precipitation,

including rainfall amount, air temperature, latitude, altitude, and seasonality of precipitation. Due

to the range of factors that can influence the δ^{18}O value of rainwater, a relationship between local

precipitation and same-day climate variables is needed to establish a strong paleoclimate interpretation of the record of interest.

A local meteoric water line (LMWL) is needed to determine vapor source origins and evaporative conditions for our site. The $\delta^{18}O$ and δD values of global rainfall exhibit a linear correlation with an R^2 greater than 0.95, known as the global meteoric water line (GMWL) (Craig 1961). The fractionation of these isotopes during phase changes follows the GMWL formula given by $\delta D = 8 \times \delta^{18}O + 10$ (Craig 1961; Dansgaard 1964). In the GMWL equation, the slope expresses the ratio of equilibrium fractionation factors between ^{18}O and ^2H and varies by location. The y-intercept value (10) is known as the deuterium excess (d-excess) and is useful in determining what kinetic conditions may have been at play during evaporation that led to changes in the meteoric water line equation (Dansgaard 1964; Merlivat and Jouzel 1979). For example, under conditions of increased wind speeds or high relative humidity, both of which may increase evaporation rates, the kinetic effect is reduced and deuterium values of rainwater will decrease such that the y-intercept will deviate from 10 (Jouzel et al. 1982). Most influences on d-excess values involve the conditions present at the water vapor source and the phase change history of the water mass before it precipitates out (Clark and Fritz 1997; Froehlich et al. 2002).

2.2.5 Potential controls on oxygen isotopic composition of rainwater

To investigate what might control oxygen isotope variability in Texas rainwater, we analyzed ~2 years of rainfall samples from Austin, Texas. In mid-latitudes such as our central Texas site, temperature and the amount of rainfall are generally considered the two main drivers of oxygen isotope variability in rainwater. Other potential drivers of $\delta^{18}O$ variability could be altitude,

latitude, and seasonality of precipitation. On glacial-interglacial timescales, the $\delta^{18}O$ value of the ocean, related to the global ice volume on the earth, could also exert control on rainfall $\delta^{18}O$.

The so-called "amount effect", in which increased precipitation totals in a particular storm correspond with more negative isotope values of rainwater, is generally observed in the tropics and sub-tropics, including Texas. The heavy isotopes are preferentially rained out before the lighter ones, and the incorporation of recycled, lighter water vapor from storm downdrafts contributes to a more negative isotopic value in large convective storm systems (Dansgaard 1964; Lachniet 2009; Kurita 2013). Related to this effect is the phenomenon that the type of storm system that forms a particular rainfall event can also leave a fingerprint on its isotopic composition, such that stratiform clouds produce precipitation that is less depleted in $\delta^{18}O$ than rainfall from a convective storm system (Gedzelman and Lawrence 1982; Gedzelman 1988). This signature results from the structure of an MCS in which depleted vapor becomes entrenched in a cycle of downdraft recycling, leading to continual isotopic depletion of this stratiform rainfall (Kurita 2013).

A second dominant isotope effect at middle latitudes is the temperature effect, or the observed positive relationship between mean annual temperature (MAT) and the average $\delta^{18}O$ rainfall value (Dansgaard 1964; Fricke and O'Neil 1999). Kim and O'Neil (1997) determined the equilibrium $\delta^{18}O$ fractionation between water and calcite as a function of temperature, ranging from 0.18‰/°C at 35°C to 0.23‰/°C at 5°C. By combining the known temperature dependent fractionation gradient of oxygen isotope in calcite with seasonal $\delta^{18}O$ temperature fluctuations, speleothem $\delta^{18}O$ records from mid-latitude regions may reflect local paleo-temperature variations (Bar-Mathews et al. 1999; Lachniet 2008).

Other influences on rainfall $\delta^{18}O$ values include altitude, latitude, and seasonality. The altitude effect is the observed decline in $\delta^{18}O$ values with an increase in elevation, where decreased temperatures are a component of increased altitude (Rozanski et al. 1993; Clark and Fritz 1997; Lachniet 2009). As an air mass rises over an orographic barrier, condensation temperatures decrease and progressive Rayleigh distillation causes lighter isotopes to evaporate faster than heavier ones (Lachniet 2009). The continental, or latitude, effect explains the reduction in $\delta^{18}O$ values with distance from the moisture source, the ocean (Dansgaard, 1964; Rozanski et al., 1993; Clark and Fritz, 1997). There exists a sustained depletion of $\delta^{18}O$ as the amount of water vapor is reduced as an air mass travels over the continent. Heavier isotopes rain out as the mass moves inland, and from warmer to cooler conditions (Dansgaard 1964). The relative contributions of seasonal rainfall, combined with its place of origin, can also have a control on $\delta^{18}O$ values (Wang et al. 2001; Lachniet 2009), but the isotopic signature of Texas precipitation will not deviate much seasonally because the Gulf of Mexico is the primary source of moisture throughout the year.

On glacial-interglacial timescales, the $\delta^{18}O$ value of the ocean has changed due to variations in the amount of ice present on the earth. Seawater $\delta^{18}O$ increases as the amount of ice stored as continental ice sheets increases, because evaporation will preferentially remove the light isotopes (^{16}O) into the vapor and leave behind the heavier isotopes (^{18}O) in the ocean water (Lachniet 2009). Thus, in glacial periods, more ^{16}O is locked up in ice and the oceans become isotopically heavier (more positive) than during warmer periods with less continental ice. The glacial ocean $\delta^{18}O$ composition may have been ~1.1‰ higher than modern (Labeyrie et al. 1987; Shackleton 1987).

2.3 Methods

2.3.1 Austin precipitation collection

Beginning in April 2015, rainfall samples were collected from a residential area in North Austin, Texas. Rainfall was sampled at a daily resolution through an open top rain gauge. Date, sample precipitation amount (mm), and temperature (°C) on day of collection were recorded. To prevent and/or minimize evaporative loss, a thin film of mineral oil was placed inside the gauge. After each day with rain, water was transferred into a labeled bottle and stored in a freezer until isotopic analysis to minimize isotopic exchange between the water sample and the air after collection. Eighty-six Austin rainwater samples were collected and analyzed for δD and $\delta^{18}O$ makeup on a Picarro A0211 High-Precision Vaporizer attached to a Picarro Li2120 cavity ring down spectrometer based on the liquid evaporator autosampling method established by Gupta et al. (2009). The autosampler injected 2μL water samples from glass vials fitted with silicon septa. The evaporator and analyzer were cleaned with dry gas and evacuated several times, while the needle was rinsed, to remove any contamination from previous samples. With the evaporator set at 140°C and under continuous vacuum, the water sample was vaporized within several seconds of injection and then combined with the nitrogen dry carrier gas, resulting in a homogenous mixture of water vapor isotopologues. This mixture equilibrated for 2 minutes and then flowed at a constant rate in the three-way valve to the instrument for isotopic measurements. After dilution from the evaporator, the 2μL water injection resulted in a ~20,000 ± 220 ppm pulse of water vapor at ~35 Torr throughout the analyses. The measurements taken during the flat pulse of the water sample concentration profile were measured and used to calculate oxygen and hydrogen isotopic ratios in the sample. Precisions are ±0.10‰ for $\delta^{18}O$ values and ±0.50‰ for δD values, and sample results were calibrated relative to the international VSMOW standard (Craig 1961).

Recorded rainfall amounts and temperature were confirmed with historical data from Wunderground's local weather station at Quail Hollow, North Austin, Texas. Rainfall was sampled at a daily resolution, but some rain events occurred over more than one day. NOAA NCEI Radar Data Map was used to evaluate each recorded rain event. If a single rainfall event spanned more than one day based on historical radars from NCEI, isotope measurements from our data record were combined using amount-weighted averages such that each data point in our record represents a single rain event regardless of duration (n=61). The isotopic values of rainwater were then compared to other same-day variables including the amount of rainfall in a particular storm and temperature to investigate controls on oxygen isotopic composition of Texas rainwater.

2.3.2 Cobbs Cavern dripwater collection

During a February 2017 trip to Cobbs Cavern, three dripwater samples were taken from sites of active drips from the room of Cobbs Cavern where the stalagmite from this project, 16CobbB2, was collected. A fourth dripwater sample was collected from a small cave lake in a room of the cave adjacent to the collection site room. Drip rates were recorded. Samples were collected in glass bottles and a crimper was used to seal the tops immediately upon collection to prevent isotopic exchange between dripwater and water vapor in Cobbs Cavern. The samples were stored in a refrigerator until analysis. Cave dripwater samples were analyzed for δD and $\delta^{18}O$ makeup on a Picarro A0211 High-Precision Vaporizer attached to a Picarro Li2120 cavity ring down spectrometer. All water samples were measured relative to VSMOW standard and analyzed according to the Gupta et al. (2009) method described above.

18

2.3.3 Classification of Texas storms

Because MCSs deliver a majority of precipitation to Texas, storm events producing rainfall for our collected samples were filtered by MCS versus non-MCS to investigate isotopic differences based on storm type. The date of each storm was recorded on day of collection, and used to search reflectivity radar data to determine the type of storm. Radar imagery from the NCEI National Reflectivity Radar was used due to its widespread availability and high-resolution radar data (**Figure 2.5**).

Each storm that produced a rainfall sample was classified as MSC or non-MCS based on the method set forth by Houze (1989). First, the area of continuous rainfall had to exceed 100 km in length. Second, the reflectivity values had to exceed 40 dbZ and convective activity must be present during formation of the storm system. Finally, after convective activity had been detected, there must have been stratiform precipitation with reflectivity values of at least 30 dBz (Houze et al. 1989; Smull and Houze 1985; Steiner et al. 1995; Houze 2004). The presence of a leading-line trailing stratiform structure is the most common, clear indicator of a mature MCS (Houze et al. 1990), although leading stratiform and parallel stratiform arrangements are also indicative of MCS formation (Parker and Johnson 2000). NOAA time-stamped upper air maps were used to investigate the presence of lines of divergence that are required to form an MCS when the NCEI radar imagery was not sufficient in determining MCS status.

.

Figure 2.5. Mesoscale convective system (MCS) storm classification. MCS storm identified using NOAA NCEI National Reflectivity Mosaic map. This MCS, developed through a trailing stratiform structure, occurred on May 19, 2016 and delivered 63mm of precipitation to our Austin collection site.

2.4 Results

2.4.1 Isotope analysis

Austin precipitation collected from April 2015 to March 2017 had an average $\delta^{18}O$ of -4.0‰ ±2.7‰ with a range of 12.46‰ (**Table 2.1**). Rainfall δD values averaged -20.9‰ ±21.9‰ with a range of 106.8‰. During this two-year time interval, twenty-nine rain events from the dataset were classified as MCSs and delivered 1058mm of rainfall; the average MCS $\delta^{18}O$ value was -4.6‰ ±2.2‰. Non-MCS precipitation, sourced from thirty-two rain events delivering

985mm of rainfall, had an average $\delta^{18}O$ value of -3.5‰ ±2.9. Cave dripwaters from four distinct

sites inside Cobbs Cavern had an average $\delta^{18}O$ value of –4.8‰ ±0.1‰ and δD values –29.5‰

±0.7‰, with a $\delta^{18}O$ range less than 0.3‰ (**Table 2.2**). Over the nine month cave temperature

record, Cobbs Cavern maintained a steady 19.93°C (±0.03°C). D-excess values were also similar

between precipitation and cave dripwater, as Austin precipitation d-excess averaged -11.3‰

±5.5‰ and cave dripwater 8.7‰ ±1.6‰.

Table 2.1. Austin rainfall isotope value results. Rainfall collected from our residential site in North Austin, Texas from April 2015 to March 2017.

Date	$\delta^{18}O$ (‰)	δD (‰)	d-excess (‰)
4/18/15	-8.51	-57.0	11.1
4/24/15	-1.98	-7.5	8.3
4/27/15	-1.04	-4.2	4.1
5/5/15	-1.41	2.9	14.2
5/8/15	-0.67	5.4	10.8
5/11/15	-4.98	-28.9	10.9
5/15/15	-1.43	-3.7	7.7
5/17/15	-2.76	-15.2	6.9
5/24/15	-5.51	-34.4	9.7
5/25/15	-3.96	-20.2	11.5
5/29/15	-4.50	-22.9	13.1
6/14/15	-13.13	-94.7	10.3
6/20/15	-3.25	-18.2	7.8
6/27/15	-4.01	-22.6	9.5
9/9/15	-2.03	-2.4	13.8
10/23/15	-8.04	-50.8	13.5
10/30/15	-6.86	-41.6	13.3
11/17/15	-2.91	-10.5	12.8
11/27/15	-2.27	-0.5	17.7
12/13/15	-7.05	-45.3	11.1
12/27/15	-3.39	-13.2	13.9
1/2/16	-9.54	-83.0	-6.7
1/6/16	-4.39	-11.6	23.5
2/23/16	-8.14	-53.0	12.1
3/8/16	-8.65	-54.8	14.4
3/29/16	0.67	12.1	6.7
4/1/16	-4.06	-22.6	9.9
4/12/16	-2.90	-6.3	16.9
4/16/16	-1.76	-1.0	13.1

Table 2.1 continued

Date	$\delta^{18}O$ (‰)	δD (‰)	d-excess (‰)
4/20/16	-4.12	-17.6	15.4
4/21/16	-5.40	-30.5	12.7
4/28/16	-2.25	-7.5	10.5
4/30/16	-0.09	9.2	9.9
5/12/16	-2.60	-5.2	15.6
5/16/16	-2.49	-5.8	14.2
5/17/16	-5.10	-33.5	7.3
5/19/16	-6.45	-37.5	14.1
5/27/16	-4.50	-27.2	8.8
5/29/16	-2.20	-15.0	2.6
5/30/16	-2.69	-32.7	-11.2
6/1/16	-9.34	-62.2	12.5
6/28/16	-3.02	-14.58	9.6
7/25/16	-1.67	-2.40	11.0
8/13/16	-5.18	-32.20	9.2
8/20/16	-5.28	-31.40	10.8
8/28/16	-3.69	-17.17	12.3
9/10/16	0.05	1.23	0.9
9/23/16	-1.77	-1.43	12.7
9/24/16	-2.50	-13.90	6.1
11/3/16	-4.03	-17.78	14.5
11/6/16	-3.68	-14.01	15.5
11/7/16	-4.61	-16.60	20.3
11/22/16	-1.42	0.48	11.8
12/4/16	-8.57	-55.80	12.8
1/2/17	-5.33	-28.03	14.6
1/13/17	-1.55	4.29	16.7
1/15/17	-2.08	-2.09	14.5
1/17/17	-3.55	-12.60	15.8
2/19/17	-5.68	-31.42	14.0
3/3/17	-2.77	-2.32	19.8
3/10/17	-3.25	-13.22	12.7
Average	**-4.02**	**-20.9**	**11.3**
Stnd dev.	**2.7**	**-21.9**	**5.5**

Table 2.2. Cobbs Cavern dripwater isotope value results. Cave dripwater collected from Cobbs Cavern in Williamson County, TX in February 2017.

Sample	$\delta^{18}O$ (‰)	δD (‰)	d-excess (‰)
Drip 1	-4.92	-28.86	10.5
Drip 2	-4.66	-30.13	7.1
Drip 3	-4.75	-30.16	7.8
Pool	-4.81	-28.90	9.5
Average	**-4.78**	**-29.5**	**8.7**
Stnd. dev	**0.1**	**0.7**	**1.5**

2.4.2 Local Meteoric Water Line

To evaluate moisture source origins and evaporative conditions of our cave dripwater and its relationship to local rainfall, a LMWL for Williamson County, Texas was constructed (**Figure 2.6**). We found a significant linear correlation (R^2=0.94) between the deuterium and oxygen isotope values. The constructed LMWL has a slope (7.93) and y-intercept (10.85) very close to those of the GMWL (8 and 10, respectively), which represents the average isotopic compositions of global precipitation. Global rainfall is sourced primarily from precipitation and evaporation that occurs over the open ocean. Dripwaters collected from Cobbs Cavern fall in the middle of the constructed central Texas LMWL.
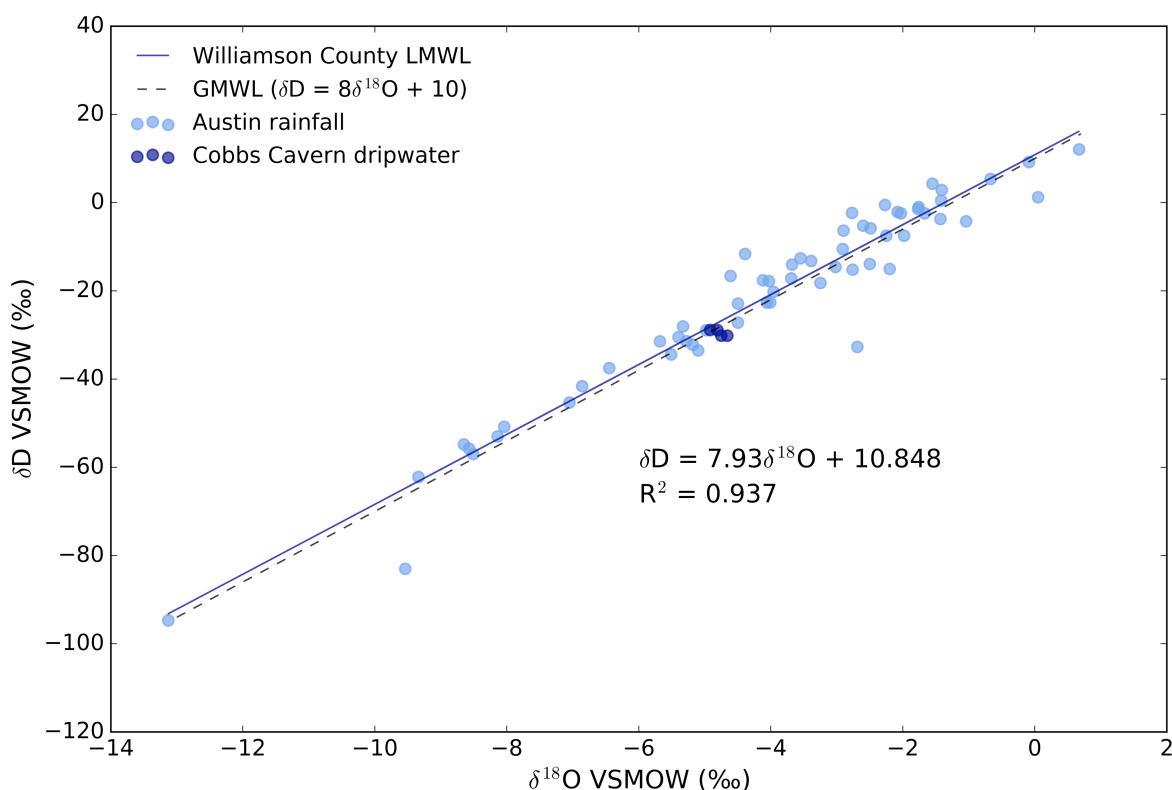
Figure 2.6. Central Texas local meteoric water line (solid blue line). Austin rainfall is plotted in light blue. Cobbs dripwater is plotted in dark blue. The global meteoric water line is plotted as the black dashed line.

2.4.3 Rainfall effects

By comparing the oxygen isotopic composition of Austin rainwater samples to temperature on the day of collection, we investigated temperature as a driver of oxygen isotope variability in Texas rainwater. We found a weak, insignificant relationship ($R^2= 0.076$) between temperature and rainwater $\delta^{18}O$ (**Figure 2.7**), suggesting that temperature is not a significant control on oxygen isotope variability. The other major potential driver of oxygen isotope variability in mid-latitude rainfall is the amount of precipitation. Here, we found a significant negative correlation (**Figure 2.8**, $R^2=0.273$, p<0.0001) between amount of precipitation in a particular rain event and

the $\delta^{18}O$ value of that rainfall, thus connecting more depleted rainfall $\delta^{18}O$ values with increased precipitation totals. After classification of each storm providing a rainfall sample as MCS or non-MCS, the negative correlation between the $\delta^{18}O$ value and the amount of rainfall was strengthened in the dataset from MCS storms (**Figure 2.9**, $R^2 = 0.305$, $p<0.0001$).

Another important factor in the signature of rainfall is the d-excess value. Physical conditions at the site of evaporation of source water vapor, including relative humidity, sea surface temperature (SST), and air temperature, are the main determinants of d-excess values (Merlivat and Jouzel 1979). Using the radar imagery method described above, storms were classified as MCS versus non-MCS. In our Austin rainwater record from April 2015 to March 2017, we found that MCSs were responsible for the majority (56%) of rainfall reaching the study site for the duration of the record.

To further investigate the connection between storm type and isotopic composition of rainfall, we compared d-excess values of MCSs versus non-MCSs storms. We did not find a significant difference between d-excess values of MCSs and non-MCSs. However, d-excess values can also be used to identify vapor origins, and in our data d-excess values are comparable between rainwater and dripwater samples, which indicates the same source of origin for both dripwater and rainwater. For Austin rainwater, d-excess values average 11.3‰ (n=61, $\sigma=5.5$). In cave dripwaters, d-excess values averaged 8.7 (n=4, $\sigma=1.5$).
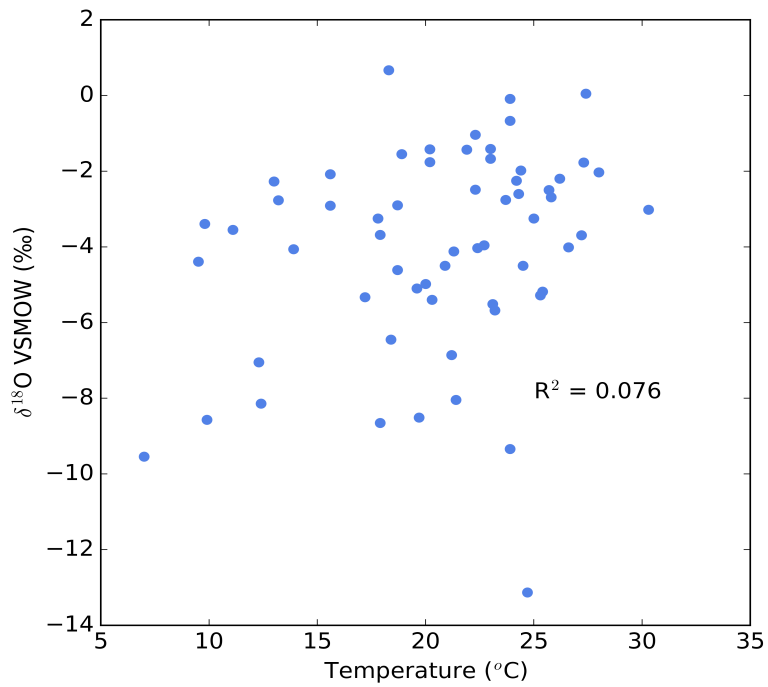
Figure 2.7. Austin rainfall oxygen isotopic composition versus temperature. Rainfall samples were collected from April 2015 to March 2017.
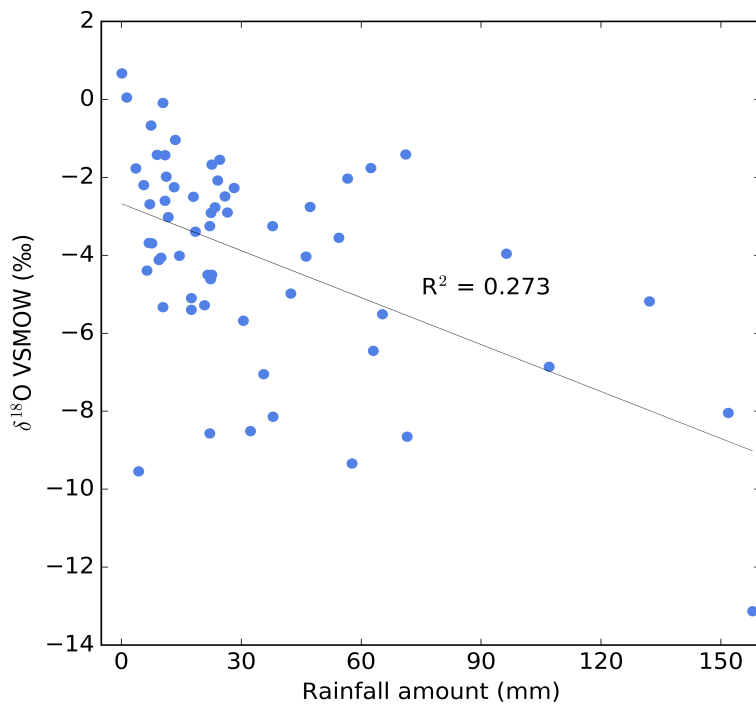
Figure 2.8. Austin rainfall isotopic composition versus amount of rainfall. Rainfall samples were collected from April 2015 to March 2017.

26
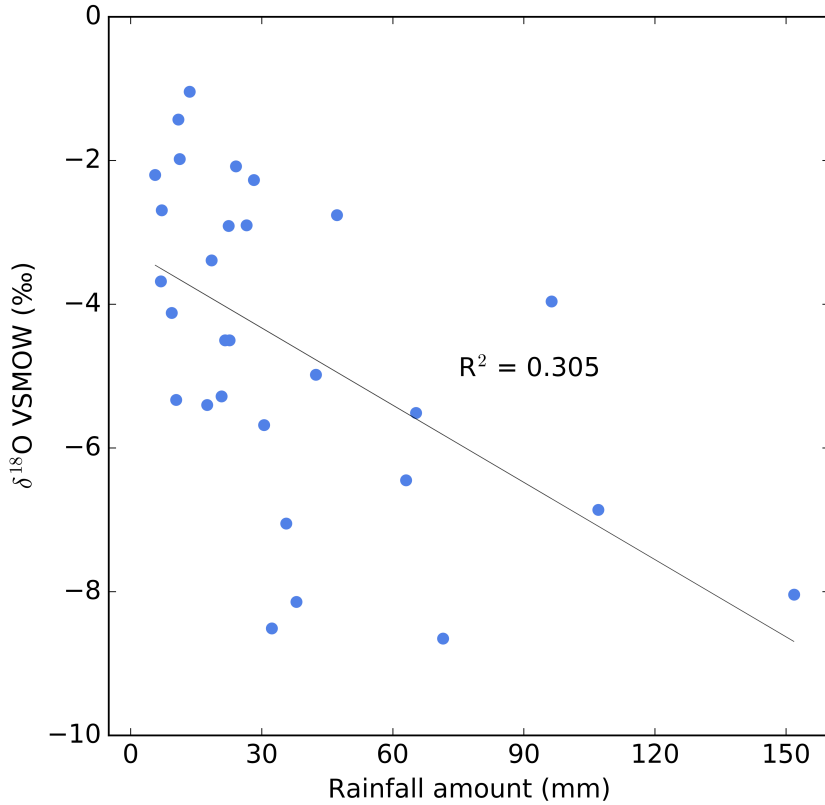
Figure 2.9. MCS-only Austin rainfall isotopic composition versus rainfall amount. Rainfall samples were collected from April 2015 to March 2017.

2.5 Discussion

2.5.1 Cobbs Cavern dripwaters on the Local Meteoric Water Line

The constructed LMWL for Williamson County, Texas, is within reasonable error of the GMWL with cave dripwaters falling in the center of the LMWL, thereby indicating an open ocean source of moisture for both our Austin rainwater and Cobbs Cavern dripwaters. For central Texas and the SGP, this source is the Gulf of Mexico. Because cave lake stable isotopic values are indistinguishable from dripwater values in Cobbs Cavern, both drip and stagnant cave waters originate from local meteoric water.

The LMWL further indicates that evaporative effects are not distorting the rain signal that is reaching Cobbs Cavern, and ultimately, the speleothem sample. If rainwater were undergoing evaporation prior to entering the cave, the isotope values would plot above the LMWL (Clark and Fritz 1997). Because the LMWL of Austin rainwater and cave dripwater has a slope approximating that of the GMWL, we have ruled out secondary evaporation effects that occur during rainfall, which is a phenomenon more common in regions of higher aridity (Clark and Fritz 1997).

Cobbs Cavern is a relatively shallow cave. The rainwater that feeds into the cave likely maintains a small residence time in the epikarst. This leaves little room for evaporation, which, in combination with our LMWL results, indicates that central Texas precipitation does not undergo significant recycling of moisture on land. Furthermore, the relatively small variance in d-excess values of rainwater (n=61, σ=5.5) suggests that the source origin of Austin precipitation is similar, and consistently the Gulf of Mexico throughout the duration of our record (Rozanski et al. 1993).

2.5.2 Lack of evidence for other isotope effects

Cobbs Cavern has an elevation of ~300m above sea level, and our Austin rainfall collection site has an elevation ~450m. No major orographic barriers exist in the SGP region, so the altitude effect does not affect $\delta^{18}O$ isotope variability in central Texas rainwater. Furthermore, because Austin is less than 200 miles from the Gulf of Mexico, water vapor does not travel far enough inland to the collection site such that the continental effect will only have a negligible impact on the $\delta^{18}O$ of rainfall at our study site. This leaves temperature and amount as the two main drivers of isotope variability. Our analysis of Austin rainfall indicates a weak

28

relationship between temperature and rainfall δ^{18}O, so temperature does not have a control on oxygen isotopic variability in Texas precipitation. Therefore, the major identifiable control on oxygen isotope variability in Texas rainwater, and ultimately, Cobbs Cavern dripwater, is the amount of rainfall reaching the cave.

2.5.3 Dominant amount effect in Austin precipitation

The amount effect is the observed phenomenon in which the isotopic values of tropical and sub-tropical rainfall become more negative with increased precipitation under modern climate conditions (Dansgaard 1964). This effect allows for paleorainfall reconstructions of speleothem isotope records from mid- and low-latitude regions (Wang et al. 2001; Cruz et al. 2005; Partin et al. 2007; Cross et al. 2015). Our Austin rainfall data demonstrates a statistically significant amount effect. Previous rainfall analyses in central Texas have also documented the presence of a so-called amount effect in Texas precipitation (Wong et al. 2015).

One of the mechanisms driving this amount effect is the type of storm system delivering the precipitation. During spring and fall in the SGP, multicell cluster storms, including MCSs, deliver large amounts of rainfall to the region. A substantial proportion of rainfall in tropical and warmer, mid-latitude regions are the result of MCSs (Houze 2004). MCSs are the largest of convective storms and are most typically defined as cumulonimbus cloud systems that generate an area of precipitation covering more than 100 km^2. In a system as organized as an MCS, surface vapor feeds the creation of a convective updraft; this vapor advects to the stratiform region of rainfall and precipitates out. If nearby air is unsaturated, evaporation of this rainfall may occur such that lighter isotopes preferentially undergo evaporation before the heavier isotopes. The vapor becomes depleted with respect to δ^{18}O composition, and is funneled into the

downdraft where it cycles through this pattern of rainout, downdraft incorporation, and further isotopic depletion, resulting in MCS cycling as a crucial mechanism of the amount effect in isotope geochemistry (Kurita 2013). Kurita et al. (2011) also found that the most negative isotopic extremes in surface water vapor are correlated with maximum amounts of precipitation in MCS stratiform precipitation regions, thus providing more evidence correlating more depleted oxygen isotope values in rainwater with increased amounts of MCS-sourced rainfall.

Our rainfall record demonstrates an enhanced amount effect in MCS precipitation. After classifying each storm from our dataset, we found a strong negative correlation between the amount of rainfall and that rainfall's δ^{18}O value. This indicates that storm structure, which is related to the amount of rain in a storm event, can influence the isotopic value of rainfall. Large, organized MCS storms likely contribute to the more depleted isotopic signal found in our Austin rainfall data. Therefore, in the speleothem record presented in Chapter 3, more negative δ^{18}O values reflect increased precipitation due to climate conditions in which the polar jet delivers frequent cold fronts to the SGP, which function as lifting mechanisms for humid Gulf air and result in more intense, organized convective systems in the region and thus large amounts of precipitation. In other words, the "amount effect" in the speleothem record is fueled by the persistence of a climate regime encouraging formation of MCSs and overall wetter conditions.

2.5.4 Proposed glacial vs. interglacial climate dynamics

During excursions of global warming, planetary jet streams shift poleward as energy is transferred to the polar zones from heat accumulation and the decline of sea ice (Archer and Caldeira 2008). This results in temperature extremes that send cooler air to the middle latitudes, which ultimately encourages storm generation in mid-latitude regions (Screen et al. 2012).

Francis and Vavrus (2016) hypothesized that the reduced temperature gradient between polar and mid-latitude atmospheres causes the polar jet to adopt a more oscillatory path. Because the amplitude of planetary waves increases, their speed decreases, the flow becomes weakened and elongated, and more extreme weather occurs in mid-latitude regions (Francis and Vavrus 2016). Therefore, during periods of higher global temperatures, the polar jet stream shifts north and adopts an oscillatory pattern with slower waves of greater amplitude.

Although there is little previous regional work on glacial-interglacial timescales investigating these climate dynamics, we propose a similar atmospheric mechanism for glacial versus interglacial periods. In warm interglacial periods in the SGP, such as MIS 5e, the amount effect is strengthened by the persistence of a climate pattern with conditions favorable for large, organized storm growth (**Figure 2.10**). As the temperature gradient between the high and middle latitudes is reduced, the polar jet stream moves northward and gains amplitude, thus delivering more frequent cold fronts to the SGP. These fronts then function as lifting mechanisms for humid Gulf of Mexico air, which is funneled onto the continent by the western branch of the Bermuda High. Increases in summer temperatures can intensify development of the Bermuda High (Betancourt et al. 1990), which further propels warm air from the Gulf of Mexico into the path of southerly cold fronts. This results in more frequent and intense convective storm system formations that release rainfall with more depleted oxygen isotopic compositions. During glacial times, we suggest that MCS activity is reduced because the polar jet is farther south and less oscillatory such that it does not flush as many frontal systems into the SGP (**Figure 2.11**). Furthermore, air coming from the Gulf of Mexico is less warm and holds less water vapor during glacial times. This lack of a penetrative polar jet combined with cooler Gulf air results in less

frequent MCS formation, and thus more sporadic, smaller rainfall events with less depleted oxygen isotopic compositions.

Figure 2.10. Interglacial SGP climate schematic. Conditions of global warming encourage a northward shift of the polar jet. The polar jet adopts an elongated, more oscillatory pattern as the Arctic warms faster than the equatorial region, which reduces the temperature gradient between the polar and mid-latitude atmospheres. The polar jet is then positioned to deliver frequent cold fronts to the SGP, thus fueling uplift of warm, humid air from the Gulf of Mexico and resulting in more frequent mesoscale convective system formation.

(B) Glacial SGP Climate Dynamics
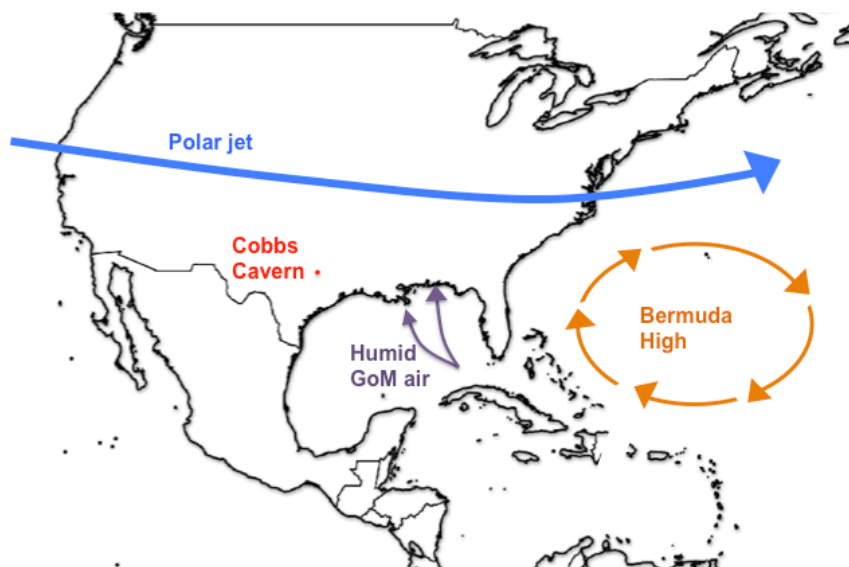
Figure 2.11. Glacial SGP climate schematic Under a glacial climate regime, the severe temperature gradient between the polar and mid-latitude atmospheres forces the polar jet to maintain a constrained, less oscillatory path that does not penetrate into the SGP region. Air from the Gulf of Mexico is less warm and holds less water vapor, resulting in less convective storm activity in the region.

2.6 Conclusions

This two-year dataset of central Texas precipitation and Cobbs Cavern dripwaters illustrates that cave dripwater reflects the isotopic composition of rainfall in central Texas, which corresponds with rainfall variability in the broader SGP region. While there is no significant evidence for air temperature as a control on oxygen isotope variability in our rainfall dataset, there is a statistically significant relationship between the oxygen isotopic composition of a particular rain event and the amount of rainfall associated with that event. The remaining isotope effects are negligible, and we conclude that the chief driver of oxygen isotope variability in our central Texas rainwater is the amount of precipitation in a particular rain event. Furthermore, after classifying storm type, we found that the amount effect is more pronounced in organized

storm systems such as MCSs. More frequent and extreme convective system formation is likely attributed to a stronger, more penetrative polar jet that is intensified during warmer conditions.

Our LMWL results suggest that central Texas rainfall does not undergo significant recycling of moisture on land, and that the Gulf of Mexico is our open ocean source of moisture throughout the year. The lack of significant variance in Austin rainwater d-excess values further suggests that the vapor source of precipitation and source vapor evaporative conditions are similar and consistent throughout the record (Rozanski et al. 1993). Barring any in-cave kinetic effects (discussed in Chapter Three), dripwater from Cobbs Cavern will be representative of meteoric water originating from the Gulf of Mexico. Based off our analysis of modern SGP rainfall, Austin precipitation data, and cave dripwater data, the speleothem record presented in Chapter Three will likely be a robust reconstruction of variability of rainfall amounts during rainy years and storm structure in the SGP.

2.7 References

Archer, C. L. and K. Caldeira. 2008. Historical trends in the jet streams. Geophys. Res. Lett. 35: L08803.Archer, C. L. and K. Caldeira. 2008. Historical trends in the jet streams. Geophys. Res. Lett. 35: L08803.

Bar-Mathews, M., Ayalon, A., Kaufman, A., Wasserburg, G.J., 1999. The eastern Mediterranean paleoclimate as a reflection of regional events: Soreq Cave, Israel, *Earth Planet. Sci. Lett.* 166: 85–95.

Betancourt, J.L., Van Devender, T.R., and P.S. Martin. 1990. Packrat Middens: The Last 40,000 Years of Biotic Change, University of Arizona Press.

Bradley, R.S. 2015. Paleoclimatology: Reconstructing Climates of the Quaternary, Third Ed., Academic Press, Oxford, UK.

Clark, I., and P. Fritz. 1997. Environmental Isotopes in Hydrology, Lewis Publishers, New York, NY.

Craig, H. 1961. Isotopic variations in meteoric waters, *Science* 133: 1702-03.

Cross, M., McGee, D., Broecker, W.S., Quade, J., Shakun, J.D., Cheng, H., Lu, Y., Edwards, R.L. 2015. Great Basin hydrology, paleoclimate, and connections with the North Atlantic: A speleothem stable isotope and trace element record from Lehman Caves, NV, *Quaternary Science Reviews* 127: 186-98.

Cruz, F.W., Burns, S.J., Karmann, I., Sharp, W.D., Vuille, M., Cardoso, A.O., Ferrari, J.A., Silva Dias, P.L., Viana, O. 2005. Insolation-driven changes in atmospheric circulation over the past 116,000 years in subtropical Brazil, *Nature* 434: 63–66.

Dansgaard, W. 1961. The isotopic composition of natural waters. Medd. Om Gronland, 166(2): 1-120.

Dansgaard, W. 1964. Stable isotopes in precipitation, *Tellus* 16(4): 436–468.

Elliott, R.D. 1949. Forecasting the weather – The weather types of North America, *Weatherwise* 2: 15-18.

Francis, J.A. and S.J. Vavrus. 2012. Evidence linking Arctic amplification to extreme weather in mid-latitudes, *Geophys. Res. Lett.* 39: L06801.

Fricke, H.C. and J. R. O'Neil. 1999. The correlation between 18O=16O ratios of meteoric water and surface temperature: its use in investigating terrestrial climate change over geologic time, *Earth and Planetary Science Letters* 170: 181-196.

Fritsch, J.M., Kane, R.J., and C.R. Chelius. 1986. The Contribution of Mesoscale Convective Weather Systems to the Warm-Season Precipitation in the United States, *Journal of Applied Meteorology and Climatology* 25: 1333-1345.

Froehlich, K., Gibson, J.J., and P. Aggarwal. 2002. Deuterium excess in precipitation and its climatological significance, Proc. Int. Conf. on Study of Environmental Change Using Isotope Techniques: C&S Papers Series 13/P, Vienna, Austria, International Atomic Energy Agency: 54-66.

Gedzelman, S.D., and J.R. Lawrence. 1982. The isotopic composition of cyclonic precipitation, *Journal of Applied Meteorology* 21: 1385-1404.

Gedzelman, S.D. 1988. Deuterium in water vapor above the atmospheric boundary layer, *Tellus*, 40b: 134-147.

Gupta, P., Noone, D., Galewsky, J., Sweeney, C., and B.H. Vaughn. 2009. Demonstration of high-precision continuous measurements of water vapor isotopologues in laboratory and remote field deployments using wavelength-scanned cavity ring-down spectroscopy (WS-CRDS) technology, *Rapid Commun. Mass Spectrom*. 23: 2534–2542.

Houze, R.A., Rutledge, S.A., Biggerstaff, M.I., and Smull, B.F. 1989. Interpretation of Doppler Weather Displays of Midlatitude Mesoscale Convective Systems, *American Meteorological Society* 70(6): 608-619.

Houze, R.A., Smull, B.F., and P. Dodge. 1990. Mesoscale Organization of Springtime Rainstorms in Oklahoma, *Monthly Weather Review* 118: 613-654.

Houze, R. A. 2004. Mesoscale convective systems, *Reviews of Geophysics* 42(4): RG4003.

Jouzel, J., Merlivat, L., and C. Lorius. 1982. Deuterium excess in an East Antarctic ice core suggests higher relative humidity at the oceanic surface during the last glacial maximum, *Nature* 299: 688–691.

Kim, S.-T. and J. R. O'Neil. 1997. Equilibrium and nonequilibrium oxygen isotope effects in synthetic carbonates, *Geochimica et Cosmochimica Acta* 61: 3461–3475.

Kumjian, M., Evans, J.S., and J.L. Guyer. 2006. The relationship of the Great Plains low level jet to nocturnal MCS development. Preprints, 23rd Conf. on Severe Local Storms, St. Louis, MO, Amer. Meteor. Soc. P. Vol. 1.

Kunkel, K. E. et al. 2013. Regional Climate Trends and Scenarios for the U.S. National Climate Assessment Part 4. NOAA Technical Report NESDIS 142-4: 1–91.

Kurita, N., Noone, D., Risi, C., Schmidt, G.A., Yamada, H., and K. Yoneyama. 2011. Intraseasonal isotopic variation associated with the Madden-Julian Oscillation, *Journal of Geophysical Research* 116: D24101.

Kurita, N. 2013. Water isotopic variability in response to mesoscale convective system over the tropical ocean, *Journal of Geophysical Research-Atmos* 118(18), 10,376–10,390.

Labeyrie, L., Duplessy, J.C., and P.L. Blanc. 1987. Variations in mode of formation and temperature of oceanic deep waters over the past 125,000 years, *Nature* 327: 477-482.

Lachniet, M. S. 2009. Climatic and environmental controls on speleothem oxygen isotope values, *Quaternary Science Reviews* 28(5-6): 412–432.

Merlivat, L. and Jouzel, J. 1979. Global climatic interpretation of the deuterium-oxygen 18 relationship for precipitation, *Journal of Geophysical Research* 84: 5029-33.

Nativ, R. and Riggio, R. 1990. Precipitation in the Southern High Plains: Meteorologic and isotopic features, *Journal of Geophysical Research* 95(0148-0227).

Nielsen-Gammon, J. W. 2011. The changing climate of Texas, The impact of global warming on Texas 39-68.

Parker, M.D., and R.H. Johnson. 2000. Organizational Modes of Midlatitude Mesoscale Convective Systems, *Monthly Weather Review* 128: 3413-3436.

Partin, J. W., K. M. Cobb, and J. L. Banner. 2008. Climate variability recorded in tropical and s ub-tropical speleothems, *PAGES* 16(3): 2.

Rozanski, K., Araguás-Araguás, L., Gonfiantini, R. 1993. Isotopic patterns in modern global precipitation. In: Swart, P.K., Lohmann, K.L., McKenzie, J., Savin, S. (Eds.), Climate Change in Continental Isotopic Records. American Geophysical Union, Washington, DC, 1–37.

Screen, J.A., Deser, C., and I. Simmonds. 2012. Local and remote controls on observed Arctic warming. *Geophys. Res. Lett.* 39: L10709.

Shackleton, N.J. 1987. Oxygen isotopes, ice volume and sea level, *Quaternary Science Reviews* 6(3-4): 183-190.

Steiner, M., Houze, R.A. Jr., and S.E. Yuter. 1995. Climatological Characterization of Three-Dimensional Storm Structure from Operational Radar and Rain Gauge Data, *Journal of Applied Meteorology* 34: 1978-2007.

Wang, Y. J., H. Cheng, R. L. Edwards, Z. S. An, J. Y. Wu, C. C. Shen, and J. A. Dorale. 2001. A high-resolution absolute-dated late Pleistocene monsoon record from Hulu Cave, China, *Science* 294(5550): 2345-2348.

Wong, C. I., J. L. Banner, and M. Musgrove. 2015. Holocene climate variability in Texas, USA: An integration of existing paleoclimate data and modeling with a new, high-resolution speleothem record, *Quaternary Science Reviews* 127(c): 155–173.

CHAPTER III

LATE PLEISTOCENE AND HOLOCENE CLIMATE INFERRED FROM STABLE

ISOTOPES IN A TEXAS STALAGMITE

3.1 Introduction

In the US Southern Great Plains (SGP), the efficacy of water management strategies and, ultimately, the economic health of this agriculturally significant region, depends on a better understanding of how SGP hydroclimate may vary with future climate change. Atmospheric concentrations of major greenhouse gases, including carbon dioxide, methane, and nitrous oxide, are higher now than they have been for the last 800,000 years (IPCC 2014). While global surface temperatures are expected to rise by 1.5 to 2°C by 2100, precipitation forecasts are less straightforward since rainfall variability will not be uniform across the globe (IPCC 2014). The IPCC RCP8.5 scenario forecasts increased precipitation amounts in high and low latitudes, but there is greater uncertainty surrounding the rainfall forecasts in mid-latitude and subtropical regions (IPCC 2014). According to RCP8.5, continental mid-latitude regions are expected to experience more intense and frequent extreme rainfall events (IPCC 2014). A better understanding of the mechanisms driving past rainfall variability and the influence of future climate scenarios on these mechanisms is needed to ensure water security into the future, especially in regions already experiencing water resource stress.

One such region is the Great Plains region, which comprises roughly 70% farmland and/or rangeland, and depends heavily on precipitation alone for crop irrigation (Kunkel et al. 2013). While croplands in the western half of the SGP are mostly irrigated, their water resources–such as the Ogallala Aquifer–are being rapidly depleted (Rosenberg et al. 1999). This region's

38

viability and success in crop production is highly sensitive to a range of climatic conditions including rainfall, temperature and heat stress, ozone levels, and severe weather events (Kunkel et al. 2013). Understanding the hydroclimate variability of this economically significant region will help policymakers devise more effective water management strategies and climate change mitigation plans.

Although the instrumental climate record is useful in studying modern climate dynamics, it does little to contribute to understanding climatological variability beyond the last century and necessitates the use of paleoclimate records. Long-term records of regional hydrological variability allow for investigations into patterns of wet or dry periods that can be placed in the context of distinct global climate regimes such as glacial vs. interglacial periods. Marine and terrestrial paleoclimate archives are able to record these glacial-interglacial cycles. For example, ice cores recovered from Antarctica have trapped air bubbles for the past ~800 kyr; analysis of this air has revealed variations in CO_2 that align with the past four ~100 kyr glacial-interglacial cycles (Petit et al. 1999). During glacials, the planet is colder, drier, and dustier, with more extensive ice sheets, than interglacial periods such as the most recent glacial period that occurred from 120 kyr to 11.5 kyr BP. The Holocene interglacial began thereafter and has lasted until present day.

A time period of particular interest is the penultimate interglacial period, known as the Eemian interglacial, or Marine Isotope Stage (MIS) 5e. MIS 5e peaked around 125 kyr BP and had temperatures as much as 2°C warmer, (Shackleton 2002), sea level 4-6m higher (Bard et al. 1990), and ice sheets smaller (Cuffey and Marshall 2000) than present day. MIS 5e thus has the potential to serve as an analogue for future planetary warming scenarios, but robust paleoclimate archives are needed to investigate climate conditions during this period.

39

Speleothems are a useful archive that allow for long term paleoclimate reconstructions based on their isotopic composition. These cave deposits record the isotopic footprint of rainfall as mineral-rich, meteoric water seeps into the karst system and drips to form stalactites and stalagmites. Recently, speleothems have been used for a variety of reconstructions ranging from temperature to rainfall amount in part because speleothem growth typically arises from closed system karst formations and speleothem samples are suitable for high-precision uranium-thorium (U/Th) disequilibrium dating (Shen et al. 2012). Therefore, generating a high-resolution time series in tandem with an oxygen isotope depth series sampled from a U/Th dated speleothem can allow for robust reconstructions of hydroclimate variability well beyond the Holocene.

Studying past variability in the climate dynamics of glacial and interglacial periods will help elucidate what controls orbital configuration may have on the climate system. Stalagmite oxygen isotopic records from tropical and sub-tropical regions across the planet have demonstrated significant orbital signals that roughly align with variability in summer insolation (Wang et al. 2001; Wang et al. 2008; Cruz et al. 2005; Fleitmann et al. 2007). In some monsoon climates, Milankovitch forcing—primarily precessional cycles of ~23kyr—have a role in the intensity of rainfall. Records have indicated a robust correlation between summer insolation and summer monsoon intensity, as increased solar radiation builds stronger monsoons and may shift inland the position of the ITCZ during the summer season (Wang et al. 2001; Asmerom et al. 2007; Cruz et al. 2005). However, this relationship remains ambiguous for much of the globe. More well-dated, long-term paleoclimate data, such as speleothem records, are needed to establish a clearer understanding of how variability in orbital geometry and insolation may influence the variability of rainfall throughout the planet.

Wang et al. (2001) generated a record correlating $\delta^{18}O$ variability in Chinese stalagmite samples to the relative intensity of the summer East Asian Monsoon (EAM) over the last 75,000 years. They found a link between EAM intensity and stadial-interstadial Dansgaard-Oeschger (D/O) cycles recorded in Greenland ice records (Dansgaard et al. 1993) to conclude that abrupt climate events caused by rapid changes in ocean and atmosphere patterns are hemispheric in scope and shift from more latitudinal patterns in stadials to longitudinal patterns in interstadials (Wang et al. 2001). Cheng et al. (2016) continued this work to more precisely constrain the timing of ice age boundaries using stalagmite samples from China. In the U.S., Asmerom et al. (2010) generated a $\delta^{18}O$ record from a New Mexico speleothem dated from 56 kyr to 11 kyr BP and found evidence of the Younger Dryas event and Heinrich Events. Wagner et al. (2010) used a speleothem record to demonstrate the prevalence of drier conditions in the U.S. Southwest during interstadial periods, and wetter conditions during stadials as established in the Greenland ice record.

In Texas, the most prolific proxy data include tree rings, speleothems, and sediment records. Tree rings are an important climate archive to investigate drought history, but despite their potential for high-resolution reconstructions, tree ring records are limited to the past ~500 years. Cleaveland et al. (2011) used bald cypress rings from central Texas to demonstrate the consistency of extended droughts in recent SGP climate. Other tree ring work has been conducted in Texas, but have chronologies extending back fewer than 400 years (e.g. Stahle et al. 2016). Thus, while these climate archives help elucidate recent climate patterns, they do not contribute to a robust understanding of regional changes in mean state and forcing.

Although speleothem work has been conducted in Texas and the SGP, previous Texas speleothem oxygen isotope records only cover discontinuous intervals–about 9 to 19,000 years

BP–in the Holocene (Wong et al. 2015; Feng et al. 2014). Feng et al. (2014) generated a record

of the Last Glacial Maximum (LGM) and Bolling-Allerod warm period from a central Texas

speleothem that demonstrated a 2‰ depletion in $\delta^{18}O$ in Termination I. Comparison of U.S.

Southwest speleothem records with a Texas record revealed variability in the source of moisture

during deglacial times (Feng et al. 2014; Asmerom et al. 2010; Wagner et al. 2010). Wong et al.

(2015) also generated a central Texas speleothem $\delta^{18}O$ record for the Holocene but found no

trend other than a roughly 1500-year 0.5‰ oscillatory pattern. Nevertheless, these records

validate the potential for past rainfall reconstructions from dripwater $\delta^{18}O$ recorded in carefully

chosen Texas speleothem samples that have been screened for kinetic fractionation effects.

3.1.2 Stable isotopes in speleothems

The relevant stable isotopes of oxygen are ^{16}O and ^{18}O, and a mass spectrometer is used

to measure the ratios of both isotopes relative to a standard. The result is reported in "delta"

notation ($\delta^{18}O$) and the equation is as follows (**Equation 1**):

$$\delta^{18}O = \left(\frac{^{18}O/^{16}O_{sample} - {}^{18}O/^{16}O_{standard}}{^{18}O/^{16}O_{standard}} \right) \times 1000$$

For carbonate materials, such as speleothems, the reference standard is Pee Dee Belemnite (PDB,

now "Vienna" PDB or VPDB) (Craig 1957). For water, the reference is Standard Mean Ocean

Water (SMOW, now VSMOW) (Gonfiantini 1978). The δ measurement is reported in "per mil"

(‰) notation, where the standards are given a value of 0.0‰. Changes in the ratio of ^{18}O to ^{16}O

as therefore conveyed as differences compared to the standard reference materials; so, relatively

lower $\delta^{18}O$ values signify that the sample is depleted in ^{18}O and thus isotopically "lighter",

whereas more positive $\delta^{18}O$ values indicate that the sample is enriched in ^{18}O and isotopically

"heavier" (Lachniet 2009). If speleothem carbonate is deposited under equilibrium conditions, its $\delta^{18}O$ value can be correlated to the $\delta^{18}O$ value of cave dripwater and the temperature of the cave because of its relationship to fractionation rates (Hendy 1971; Kim and O'Neil 1997).

Although less studied than oxygen isotopes, speleothem $\delta^{13}C$ values provide insight into vegetation cover in the region from which the speleothem grew (Dorale et al. 1998). Dripwater filters through the soil such that $\delta^{13}C$ values in the soil reflect the relative concentration of C_3 and C_4 plants (Dorale et al. 1998). Trees and cool-season grasses comprise the C_3 plant category; C_4 plants include warm-season grasses from tropical and temperature grasslands (Dorale et al. 1998). The $\delta^{13}C$ values of C_3 plants, which are found in regions with low CO_2 production or during the non-growing season, are less negative than the $\delta^{13}C$ values of C_4 plants (Dorale et al. 1998; Sundqvist et al. 2007). Thus, carbon isotope signals recorded in speleothems can aid in reconstructions of the type of ecosystem and plant life at the time the speleothem formed.

3.1.3 Speleothem formation and suitability for paleoclimate study

As rain and groundwater absorbs CO_2, it forms a weak carbonic acid (H_2CO_3). This acid eventually disassociates into a free hydrogen ion (H^+) and bicarbonate (HCO_3^-). This solution will dissolve $CaCO_3$ as it encounters limestone (**Equation 2**). When the partial pressure of CO_2 in the solution exceeds the partial pressure of CO_2 in a cave, some CO_2 will escape from the solution and the resultant solution will be supersaturated in calcite (Hendy 1971). As the solution drips onto the cave ceiling or floor, it creates speleothems through calcite deposition (**Equation 3**).

$$H_2CO_3 + CaCO_3 \rightarrow Ca^{2+} + 2\ HCO_3^- \qquad \textbf{(2)}$$

$$Ca^{2+} + 2\ HCO_3^- \rightarrow CaCO_3 + H_2O + CO_2 \qquad \textbf{(3)}$$
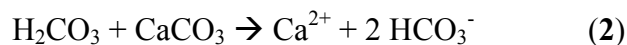
Speleothem formations record isotopic signals in C and O in the precipitated $CaCO_3$. A slow loss of CO_2 from the precipitating calcite solution–hence, a slow precipitation of calcite–results in preservation of isotopic equilibrium of aqueous CO_2 and bicarbonate ions during deposition so that variations in $\delta^{18}O$ will be representative of past climate conditions (Hendy 1971). More specifically, hydrological variability as recorded by the $\delta^{18}O$ of speleothems can be interpreted as a reconstruction of dripwater and, consequently, rainfall $\delta^{18}O$ (Partin et al. 2008; Lachniet 2009).

Although covariance between $\delta^{13}C$ and $\delta^{18}O$ in a sample was originally thought to illustrate the presence of kinetic effects (Hendy 1971), that covariance between oxygen and carbon can be attributable to climate fluctuations since $\delta^{13}C$ values may reflect vegetation changes via soil CO_2, atmospheric CO_2, and carbonate bedrock (Dorale and Liu 2009). However, rapid degassing of CO_2 prohibits the system from equilibrating isotopically during calcite deposition, which can result in fractionation of oxygen and carbon isotopes (Hendy 1971). A Replication Test can rule out kinetic effects in speleothems because if more than two speleothems from the same cave reveal similar isotopic profiles, fractionation effects must be absent or have disturbed distinct samples in the exact same manner, which is improbable (Dorale and Liu 2009). Understanding local and regional controls on rainfall $\delta^{18}O$ values is crucial in generating a robust speleothem $\delta^{18}O$ variation record (Lachniet 2009). Growth of speleothems generally results from closed system karst formations, so these cave deposits are able to be dated precisely using U/Th disequilibrium dating (Shen et al. 2012). By pairing a $\delta^{18}O$ depth series with a high-resolution time series, speleothems permit long-term reconstructions of hydroclimate variability beyond the Holocene.

44

3.1.4 Uranium-thorium dating of speleothems

Speleothems are accumulations of calcium carbonate that have precipitated from cave dripwaters. Uranium (U) is fairly soluble in natural waters, meaning that as a material such as calcite precipitates from these natural waters, it will contain small amounts of uranium. Conversely, thorium (Th) is not soluble in natural waters, so it is not included in the calcite lattice during speleothem formation. Because the ^{230}Th activity upon $CaCO_3$ formation approximates zero, the ^{230}Th concentration increases with time as a decay of ^{234}U. ^{234}U maintains secular equilibrium with ^{238}U, and the decay chain of U to Th can be used to date various calcareous materials based on the activity ratio of ^{230}Th to ^{238}U (Faure 1986). Uranium-series dating is distinct from other radiometric dating methods because it does not involve final measurement of a stable end-member decay product from the chain. Rather, U-series dating measures the degree to which secular equilibrium has been reached between the parent radioactive isotope, ^{234}U, and the daughter radioactive isotope, ^{230}Th, to calculate an age.

To use this radiometric ^{230}Th-^{238}U method of dating, the initial ^{230}Th/^{238}U ratio must be very near zero, the sample must exist in a closed uranium system so that intermediate nuclides between ^{238}U and ^{230}Th do not disrupt the activity measurements for dating, and the initial activity ratio of ^{234}U/^{238}U should be known (Faure 1986). Calcite material up to 600,000 years old can be dated using this U/Th disequilibrium method (Dorale et al. 2004). This limitation results from a number of factors, including how well constrained the ^{230}Th-^{234}U ratio in a sample is, the half life of ^{230}Th, and the accuracy of knowledge of ^{230}Th and ^{234}U half-lives (Dorale et al. 2004).

3.1.5 Present Study

Determining how rainfall variability has affected this region in past interstadial (warm, non-glacial) periods is crucial to understanding how to predict future changes in the region's rainfall. In the Great Plains region, there is significant model uncertainty in the sign and intensity of hydroclimate response to different scenarios of climate change (Cook et al. 2008; Kunkel et al. 2013). The IPCC AR4 General Circulation Models (GCMs) generally forecast increased precipitation in the mid Great Plains region but reduced precipitation in the SGP by 2100 (IPCC 2014; Cook et al. 2008). Although the Coupled Model Intercomparison Project phase 3 (CMIP3) models overall forecast a reduction in SGP rainfall, they disagree on the magnitude of rainfall changes depending on the emission scenario selected (Kunkel et al. 2013). In contrast, the North American Regional Climate Change Assessment Program (NARCCAP) produced rainfall analyses forecasting an increase in future SGP precipitation relative to the reference period selected (Kunkel et al. 2013). Model disagreement obstructs a clear forecast of rainfall and extreme weather projections in the SGP.

Because few paleorainfall records exist from past interglacials on the North American continent, this project seeks to fill this paleoclimate data gap and add to the body of knowledge of SGP rainfall history. Ultimately, this may aid modelers in creating more accurate models of future precipitation variability to ensure the SGP's sustainability as both an agriculturally productive and water-secure urban region. In this chapter we present three U-series dated speleothem oxygen and carbon records from an undisturbed cave in central Texas. We use the conclusions reached from our study on oxygen isotope variability in Texas precipitation in Chapter Two to ensure a robust reconstruction of the isotope geochemistry of our speleothem calcite. The U/Th dates indicate speleothem growth from 350 to 3800 years BP, from 98,000 to

130,000 years BP, and from 179,000 to 209,000 years BP. Therefore, we have isotope data from both the Late Holocene and the Late Pleistocene, including the penultimate interglacial period of MIS5e. We use the oxygen isotope record we generated to investigate what drives $\delta^{18}O$ variability in our speleothem, and compare modern conditions (~350 yr BP) to past interglacial (MIS 5e) conditions in order to investigate how rainfall variability may shift in the SGP in response to calculated rises in Northern Hemisphere (NH) insolation and predicted anthropogenic warming scenarios. Our Texas speleothem records contribute to a clearer understanding of SGP hydroclimate variability on orbital timescales.

3.2 Setting

3.2.1 Southern Great Plains climatology

The Great Plains region comprises a diversity of agricultural products including soybeans, cotton, corn, cattle, and hogs; these products are highly sensitive to climate extremes and water stress, and irrigation is already depleting regional aquifers (Kunkel et al. 2013). On average, the eastern half of the SGP receives more than 1800 mm (70in) each year, whereas the western half receives less than 300 mm (12 in) of annual rainfall (Basara et al. 2013). This variance in rainfall amount in a ~1000km wide region results in a diversity of temperature and precipitation patterns. Furthermore, this region frequently experiences extreme weather events, including tornadoes, flooding, and drought, with intensities and storm types that vary widely depending on location (Kunkel et al. 2013).

Geographical and physical features of the region also contribute to the diversity of climates found in the Great Plains. The Rocky Mountain Range, the western border of the Great

47

Plains, prevents Pacific Ocean moisture from reaching this region; thus, the main source of moisture to the region, especially the southern half or the SGP region, is the Gulf of Mexico (Kunkel et al. 2013). A standing high-pressure system persists in the subtropical Atlantic Ocean and pulls warm air from the ocean into the SGP such that warm and humid conditions prevail for much of the year (Kunkel et al. 2013). When positioned sufficiently southward, the polar jet stream can bring cold fronts into the region; these fronts then act as lifting mechanisms for humid Gulf of Mexico air and often results in formation of convective systems.

The low-level flow over the SGP region during spring and summer months often generates a nocturnal low-level jet (LLJ) with the Gulf of Mexico (GoM) serving as chief source of moisture to the SGP (Higgins et al. 1997). In the spring months, the Bermuda High leads to the formation of southerly winds that transport unstable, warm air from the GoM to the SGP (Mo et al. 2005; Tuttle and Davis 2006). Thus, distinct LLJ events, sometimes referred to as the Great Plains low-level jet (GPLLJ), form an atmospheric flow bringing summer precipitation to the SGP region (Cook et al. 2008). Mo et al. (2005) conducted a 23-year National Centers for Environmental Protection (NCEP) reanalysis (RR) that found that the zonal easterly Caribbean low-level jet (CALLJ) carries moisture from the Caribbean to the GoM and the meridional southerly GPLLJ moves moisture onward from the GoM to the Great Plains region.

During years with an El Niño Southern Oscillation (ENSO), the LLJ teams up with an ENSO-induced standing trough over the SGP, resulting in an increased rainfall rate in the SGP (Wang et al. 2015). When the trough is directly west of the region, southwesterly flow and divergence above the SGP may result, leading to the creation of mesoscale convective systems (MCS) and heightened amounts of precipitation from GoM-sourced SGP moisture (Johns 1993; Houze 2004; Tuttle and Davis 2006; Barandiaran et al. 2013). When ENSO develops, it is

expected to increase the amount of precipitation in SGP during later spring months due to the presence of the regional LLJ. Anthropogenic warming in the form of increased SST from rising global temperatures has strengthened this connection (Wang et al. 2015).

Furthermore, past extreme hydrologic events in the central U.S. have been linked to an increase in the number of GPLLJ developments as well as a strengthening of the southerly low-level flow over the region (Cook et al. 2008). It is predicted that under current warming scenarios in the SGP, the GPLLJ will continue to strengthen as a result of intensified zonal geopotential height gradients throughout the region (Cook et al. 2008). Therefore, it is crucial to establish a better understanding of the connection between SGP atmospheric dynamics and extreme hydroclimate events.
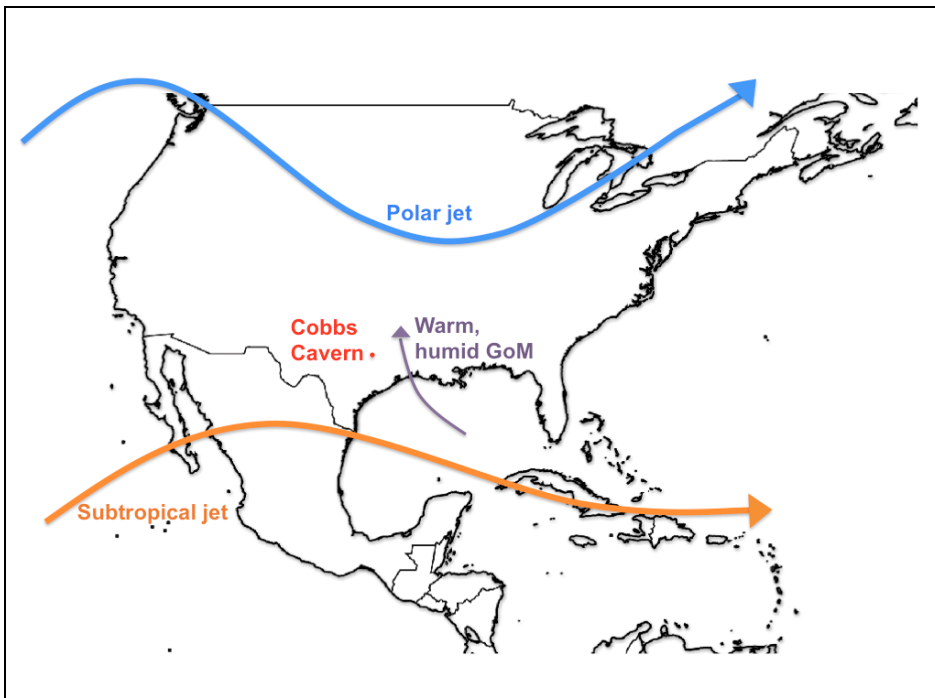
Figure 3.1. Southern Great Plains atmospheric diagram. General movement patterns of the subtropical jet (orange) and polar jet (blue).

3.2.2 Cobbs Cavern

We collected the stalagmite sample (16CobbB2) from Cobbs Cavern in central Texas. Cobbs Cavern is located on a private conservation easement in Williamson County, Texas (**Figure 3.2**, 30.5° N, 97.75° W) about 30 miles north of Austin, Texas. Williamson County is nestled in the Edwards Plateau at the foot of the Great Plains with Cobbs Cavern sitting at the northernmost part of the Balcones Fault Zone. The Edwards Plateau of central Texas forms the southernmost part of the Great Plains. The Edwards Plateau is bordered by the Rolling Plains to the north and connects with the New Mexico and Texas High Plains in the west. The watershed of the Edwards Plateau drains into the Colorado, Guadalupe, San Antonio, and Nueces Rivers and their tributaries (Blum et al. 1994). Situated in the Edwards Plateau, the Balcones escarpment region is an example of a mature karst aquifer in the SGP. Over 3,000 caves and sinkholes have been identified in the Edwards Plateau, many of which, including Cobbs Cavern, have existed since the Pliocene (White et al. 2009).

Cobbs Cavern lies on the private property of the Lyda family trust's 4-T Ranch and is one of the longest caves in Texas. This cave has limited surface expression. Access to the cave has been restricted with only the outermost half of the cave open to visitors from 1962 to 1970. With permission from the Lyda family trust and logistical assistance from the Williamson County Conservation Fund, Cambrian Environmental Consultants, and SWCA Environmental Consultants, we have amassed speleothem samples, collected cave dripwater samples to test for evaporative effects, recorded pCO_2 values in the cave, and placed temperature loggers in Cobbs Cavern to monitor temperature fluctuations.
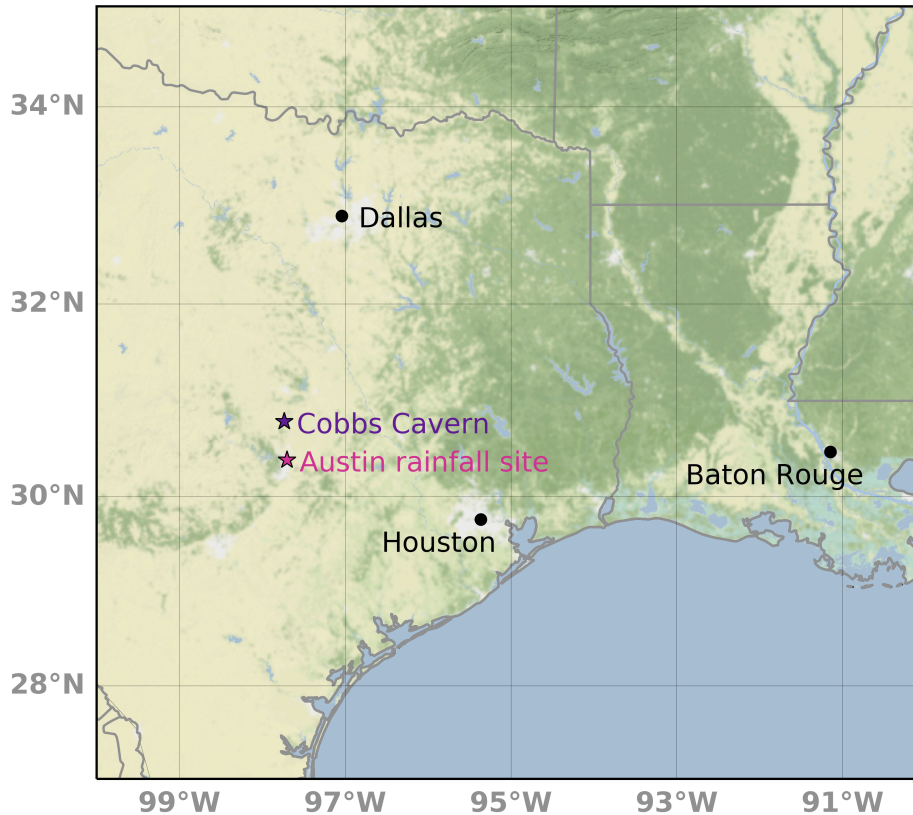
Figure 3.2. Map of Cobbs Cavern and Austin rainfall collection site.

3.3 Methods

3.3.1 Stalagmite collection and analysis

For this speleothem project, a dormant calcite stalagmite (16CobbB2) was collected in June 2016 from Cobbs Cavern in the Texas Hill country. This columnar stalagmite sample measured 146.5 cm in total length (**Figure 3.3**). We recovered the sample in a room full of other dormant and actively dripping speleothems, where the sample had been growing deep in the undisturbed side of the cave.

After collection, 16CobbB2 was sliced lengthwise with a rock saw. Each longitudinal slice of the stalagmite measured between 0.5 and 1 cm in thickness. Splitting the sample revealed

that 16CobbB2 had no visible detrital material along the growth axis in the calcite. The sample was then divided into six pieces, A through F, with A as the youngest and F the oldest.

Eighteen subsamples of 16CobbB2 Pieces A, D, and E were drilled for U/Th chemistry and ^{230}Th dating (**Figure 3.4**). Chemical separation and purification of uranium and thorium procedures were done according to methods described in Shen et al. (2002; 2003). U/Th isotopic measurements of calcite powder, ~60 mg each, were performed on a multicollection inductively coupled plasma mass spectrometer (MC-ICP-MS), Thermo-Fisher NEPTUNE, at the High-Precision Mass Spectrometry and Environment Change Laboratory (HISPEC) in the Department of Geosciences, National Taiwan University (Shen et al. 2012). To correct for mass bias and determine U and Th contents and isotope makeup, a gravimetrically calibrated triple-spike, ^{229}Th-^{233}U-^{236}U, isotope dilution method was used (Shen et al. 2012). U/Th nuclide half-lives used for ^{230}Th calculations of age are denoted in Cheng et al. (2013). U/Th isotopic errors and ^{230}Th uncertainties, relative to 1950 CE, are two standard deviation of the mean.

A computer-controlled mill was used to drill and collect calcite powder along the growth axis of each piece. Milled calcite powder was labeled and stored in a plastic vial until analysis. Oxygen and carbon stable isotope analyses in calcium carbonate were performed by a Thermo Electron Kiel IV Carbonate Device connected to a dual inlet Thermo MAT 253 stable isotope ratio monitoring mass spectrometer at the Stable Isotope Geoscience Facility (SIGF) at Texas A&M University. Calcium carbonate samples, weighing between 40 and 80 μg, were reacted with nominally 103% phosphoric acid at 75°C for 7 minutes. The resultant isotope values were reported in delta notation relative to Vienna Peedee Belemnite (VPDB) standard for carbonates. Analytical precision was determined using an internal standard calibrated to NBS-19 and IAEA-603, the isotopic reference material that measured in sample runs at a ratio of 3 standards to 20

unknown samples to track instrumental precision and accuracy. For the SIGF Kiel IV and MAT 253, the long-term average precision of this standard is 0.06‰ (±1σ) for δ^{18}O and 0.04‰ (±1σ) for δ^{13}C.
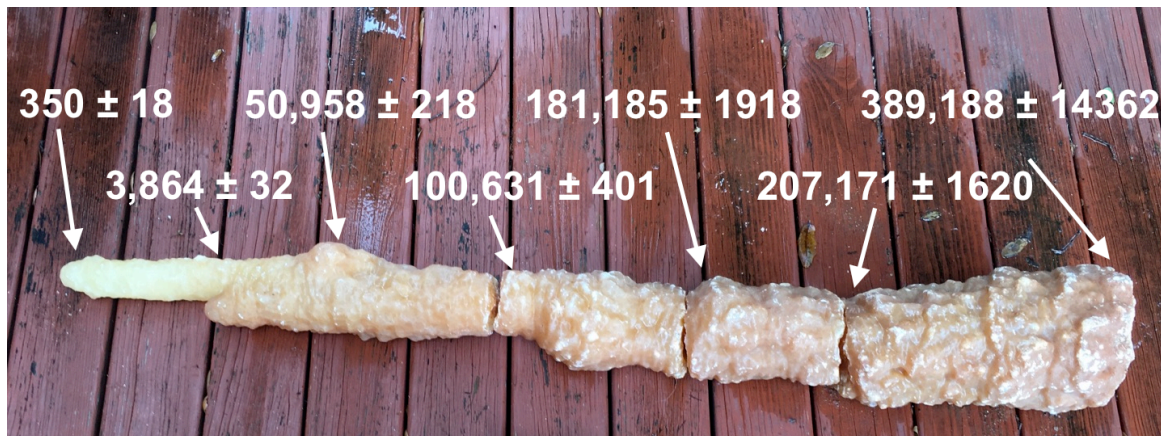
Figure 3.3. Entire stalagmite (16CobbB2). Top U/Th ages (years before 1950 AD) shown for each piece.
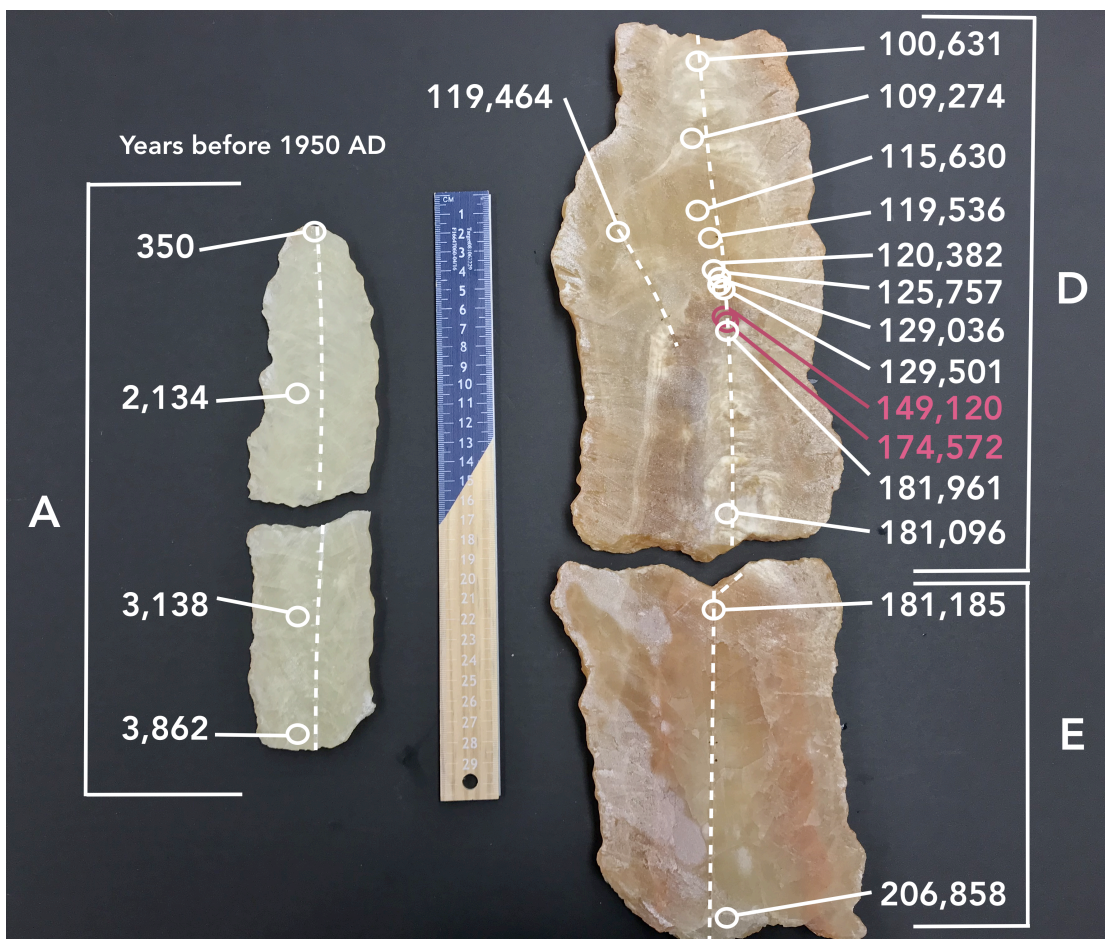
Figure 3.4. Stalagmite (16CobbB2) with dates and drill paths (dashed white lines). Pieces A, D, and E are shown, and identified hiatus dates are indicated in pink.

Table 3.1. U/Th isotopic ratios and ^{230}Th ages of 16CobbB2 pieces D and E (Pleistocene).

Piece	Distance to base (mm)[a]	^{238}U (ppb)[b]	^{232}Th (ppt)	δ^{234}U measured[b]	[^{230}Th/^{238}U] activity[c]	^{230}Th/^{232}Th atomic (x 10^{-4})	Age (yr BP) relative to 1950 AD
D	9.75	261.71 ± 0.30	17.4 ± 7.2	75.2 ± 1.4	0.6542 ± 0.0013	162008 ± 66486	100631 ± 401
D	72.25	205.9 ± 0.38	983.5 ± 7.9	46.5 ± 2.6	0.6672 ± 0.0025	2303 ± 20	109274 ± 865
D	95.75	178.48 ± 0.41	7.6 ± 7.7	50.1 ± 3.2	0.6915 ± 0.0030	267424 ± 270028	115630 ± 1118
D	103.75	336.23 ± 0.50	202.1 ± 6.8	63.2 ± 1.8	0.7144 ± 0.0021	19598 ± 662	119464 ± 746
D	113.75	314.49 ± 0.45	304.2 ± 7.5	61.1 ± 2.1	0.7131 ± 0.0027	12157 ± 302	119536 ± 950
D	125.75	275.72 ± 0.51	1044.1 ±7.7	66.9 ± 2.5	0.7206 ± 0.0027	3138 ± 25	120382 ± 987
D	146.3	202.67 ± 0.45	198.0 ± 7.0	50.1 ± 3.2	0.7345 ± 0.0027	12397 ± 437	129036 ± 1244
D	153.8	195.54 ± 0.35	146.4 ± 7.6	52.9 ± 1.9	0.7381 ± 0.0027	16257 ± 848	129501 ± 1027
D	161.3	206.38 ± 0.39	1055.6 ± 7.5	63.7 ± 2.6	0.8021 ± 0.0031	2586 ± 20	149120 ± 1501
D	166.4	321.37 ± 0.47	7.5 ± 7.5	69.5 ± 1.6	0.8656 ± 0.0028	613464 ± 613448	174572 ± 1573
D	169.7	231.66 ± 0.49	29.2 ± 7.5	69.4 ± 2.7	0.8803 ± 0.0037	115213 ± 29603	181961 ± 2365
D	268.2	160.64 ± 0.16	116.8 ± 6.4	67.3 ± 1.3	0.8766 ± 0.0019	19882 ± 1087	181091 ± 1198
E	303.95	168.88 ± 0.29	1973.5 ± 8.6	69.2 ± 2.1	0.8792 ± 0.0031	1240.5 ± 6.6	181185 ± 1918
E	450.95	153.16 ± 0.20	1.1 ± 6.9	59.4 ± 1.7	0.9128 ± 0.0025	2050847 ± 12675399	206858 ± 1998

Analytical errors are 2σ of the mean.

[a] Base given as the youngest edge of piece D

[b] [^{238}U] = [^{235}U] x 137.818 (±0.65‰) (Hiess et al., 2012); δ^{234}U = ([^{234}U/^{238}U]$_{activity}$ - 1) x 1000.

[c] [^{230}Th/^{238}U]$_{activity}$ = 1 - e^{-l230T} + (δ^{234}U$_{measured}$/1000)[l$_{230}$/(l$_{230}$ - l$_{234}$)](1 - e$^{-(l230 - l234) T}$), where T is the age.

Table 3.2. U/Th isotopic ratios and ^{230}Th ages of 16CobbB2 piece A (Holocene).

Piece	Distance to base (mm)[a]	^{238}U (ppb)[b]	^{232}Th (ppt)	δ^{234}U measured[b]	[^{230}Th/^{238}U] activity[c]	^{230}Th/^{232}Th atomic (x 10^{-4})	Age (yr BP) relative to 1950 AD
A	0.5	153.61 ± 0.27	16.8 ± 7.6	70.2 ± 2.0	0.00411 ± 0.00018	619 ± 279	350 ± 18
A	99.5	167.17 ± 0.41	89.3 ± 7.2	83.1 ± 3.4	0.02178 ± 0.00032	672 ± 55	2,134 ± 34
A	184.5	200.37 ± 0.41	281.3 ± 7.6	89.9 ± 2.6	0.03191± 0.00031	375 ± 11	3,138 ± 37
A	246.5	218.56 ± 0.39	268.6 ± 7.6	86.8 ± 2.2	0.03878 ± 0.00026	520 ± 15	3,864 ± 32

Analytical errors are 2σ of the mean.

[a] Base given as the youngest edge of piece D

[b] [^{238}U] = [^{235}U] x 137.818 (±0.65‰) (Hiess et al., 2012); δ^{234}U = ([^{234}U/^{238}U]$_{activity}$ - 1) x 1000.

[c] [^{230}Th/^{238}U]$_{activity}$ = 1 - e^{-l230T} + (δ^{234}U$_{measured}$/1000)[l$_{230}$/(l$_{230}$ - l$_{234}$)](1 - e$^{-(l230 - l234) T}$), where T is the age.

3.3.2 Cave monitoring

To gain a better understanding of the stability of the cave site, we placed HOBO temperature loggers in Cobb Cavern from April 2016 to November 2017. The first deployment starting in April 2016 included two loggers in different rooms of the ventilated side ("skylight cave") of Cobbs Cavern. The loggers were recovered and new loggers placed in different positions in the unventilated side ("deep cave") of Cobbs Cavern for the third deployment beginning in February 2017. This second set of loggers were placed in the room of the cave from which our sample, 16CobbB2, was collected. Each logger was attached to a stalagmite sample using zipties to keep it in place. At each trip to our cave site, we also recorded pCO_2 values and collected dripwater samples with the results discussed in Chapter Two.

3.4 Results

3.4.1 Cave results

Data from temperature loggers spanning April 2016 to February 2017 demonstrate a steady temperature in Cobbs Cavern (**Figure 3.5**). The Williamson County ambient air temperature fluctuates throughout the year with a range of roughly 34°C. August is generally Williamson County's hottest month with an average temperature of 28.8°C; January is typically the coldest month with an average temperature of 8.8°C (NOAA NCEI). The cave temperature as recorded by the two temperature loggers is a steady 19°C throughout the year with a minimum temperature of 18.5°C and maximum of 21.1°C. This small temperature range is derived from data from the deep cave logger as well as the more ventilated skylight logger. The skylight

logger exhibits a greater degree of variance throughout the year but still approximates 19°C
temperature year round.

The mean temperature of our record for Cobbs Cavern is 19.9°C which approximates the mean annual temperature (MAT) of Williamson County of 19.3°C. Furthermore, pCO2 values in the poorly ventilated side of the cave range from 0.9% in January, to 1.5% in June, to 1.3% in November. High pCO_2 values are generally found in caves with little to no ventilation (Gillieson 1996). This reduces the pCO_2 gradient between the cave atmosphere and the drip, which limits the likelihood of rapid degassing and favors calcite that is precipitated in isotopic equilibrium (Hendy 1971; Lachniet 2009). Together, these cave monitoring records indicate that Cobbs Cavern is providing a temperature-stable environment for the preservation of speleothems, with little outside influence. This is likely a result of the cave having little to no surface expression, and thus minimal interaction with the outside environment.
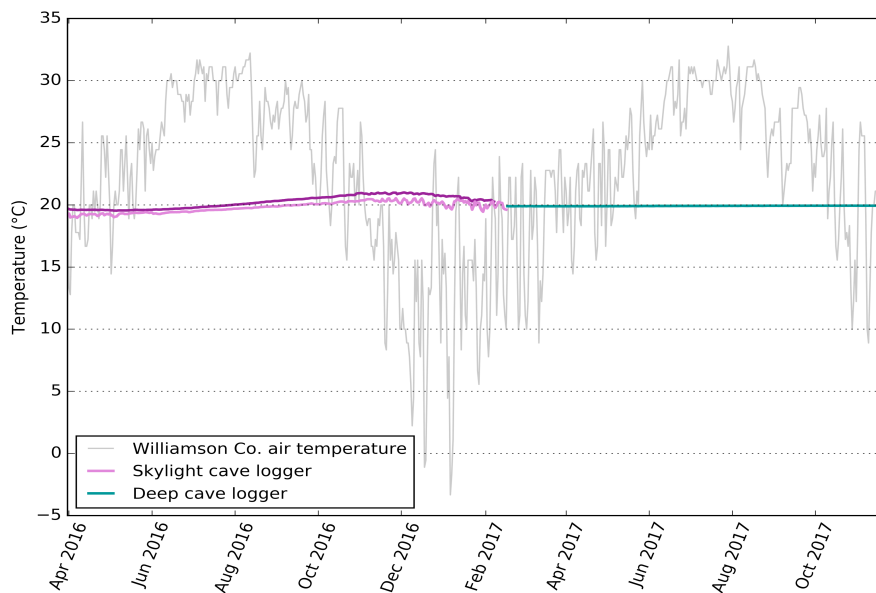
Figure 3.5. Cobbs Cavern temperature record (pink and green lines). Data from April 2016 to November 2017 with outside air temperature of Williamson County, Texas (grey). Texas temperature data from Wunderground's Georgetown Municipal Airport station.

3.4.2 Age models

We obtained 18 high-precision U/Th dates (**Table A-1**) using a multicollector inductively

coupled plasma mass spectrometry with age uncertainties of ±2%. These dates show that

16CobbB2 grew continuously from 350 to 3800 yr BP, from 98 to 130 kyr BP, and from 179 to

208 kyr BP. An age model for our speleothem sample (16CobbB2) was created by linear

interpolating between U/Th dates. Each U/Th age was used as the age model anchor point with

the exception of the older Pleistocene record, which had overlapping U/Th ages. To ensure that

our age model for this record demonstrated logical, linear growth, we used the outer boundaries

of three U/Th ages (age uncertainty subtracted from the 181,961 age, and added to the 181,091

and 181,185 ages) to approximate the most reasonable intervals of growth. We then calculated

age models and growth rates for each record using all minimum, and all maximum growth rates

to demonstrate that our average age models fall within reasonable error given the most extreme

parameters.

Based on the U/Th dates a growth hiatus was found at the ~150mm mark (piece D) along

the primary growth axis. There was a clear visible change from translucent calcite to a darker,

denser material. In our original age model (**Figure 3.6**), what is identified as a growth hiatus

included three U/Th ages ranging from 130 to 179 kyr BP over ~11 mm of growth resulting in a

growth rate below 1μm/year. In contrast the growth rates pre and post hiatus were 5 and 8

μm/year. The 2 U/Th dates, 149,311 and 174,572 yr BP, associated with this hiatus or period of

extremely slow growth were excluded from any age model development because we believe

these 2 dates to have included calcite dust from before or after the hiatus; as a consequence, pre

and post hiatus age models were developed.

The first Pleistocene age model, (**Figure 3.7A**), has dates ranging from 98 to 130 kyr BP. Eight U/Th ages were used to constrain this age model, with an average growth rate of 5 μm/yr. An age model with maximum age (U/Th age plus uncertainty) paramaters indicate a growth rate of 4.9 μm/yr, and minimum age paramaters indicate a rate of 5.3 μm/yr, supporting our calculated average growth rate of 5 μm/yr.

The second Pleistocene age model, (**Figure 3.7B**), has dates ranging from 179 to 208 kyr BP. Four U/Th ages were used to constrain this age model, with an average growth rate of 8 μm/yr. An age model with maximum age paramaters indicates a growth rate of 7.7 μm/yr, and minimum 10.9 μm/yr, thus supporting the calculated average growth rate of 8 μm/yr.

The Late Holocene age model, (**Figure 3.8**), has dates ranging from 350 to 3800 yr BP. Four U/Th ages were used to constrain the age model, with an average growth rate of 70 μm/yr. Maximum U/Th ages indicate a growth rate of 72 μm/yr, and minimum age paramaters indicate a rate of 68 μm/yr, supporting our calculated average growth rate of 70 μm/yr.
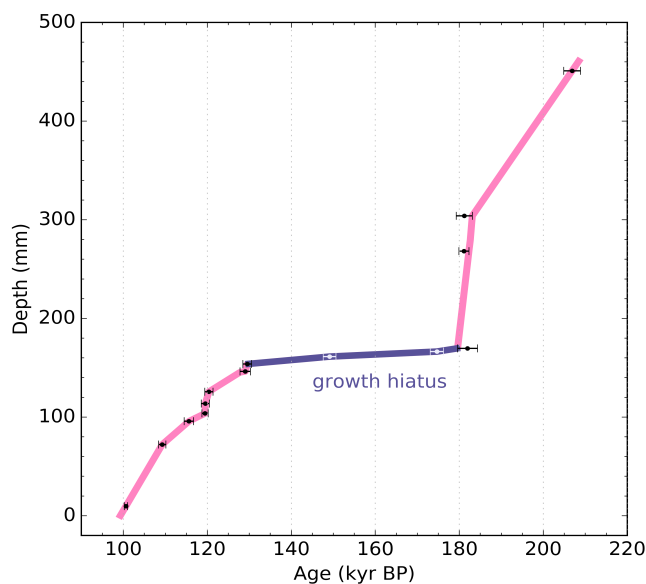
Figure 3.6. Pleistocene U/Th age model (16CobbB2) with hiatus (purple).
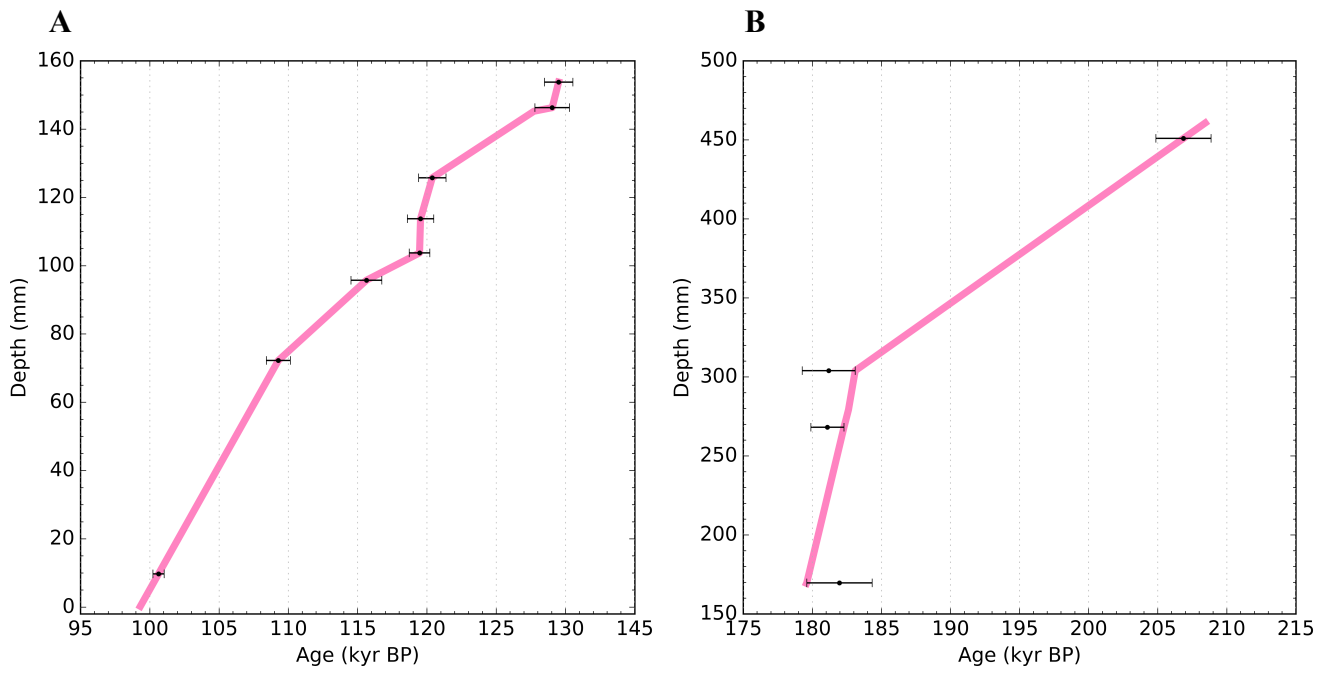
Figure 3.7. Two-part Pleistocene U/Th age model. Pre-hiatus age model from 98 to 130 kyr BP shown in A, and post-hiatus age model from 179 to 209 shown in B. An assumption of linear growth underlies the models.
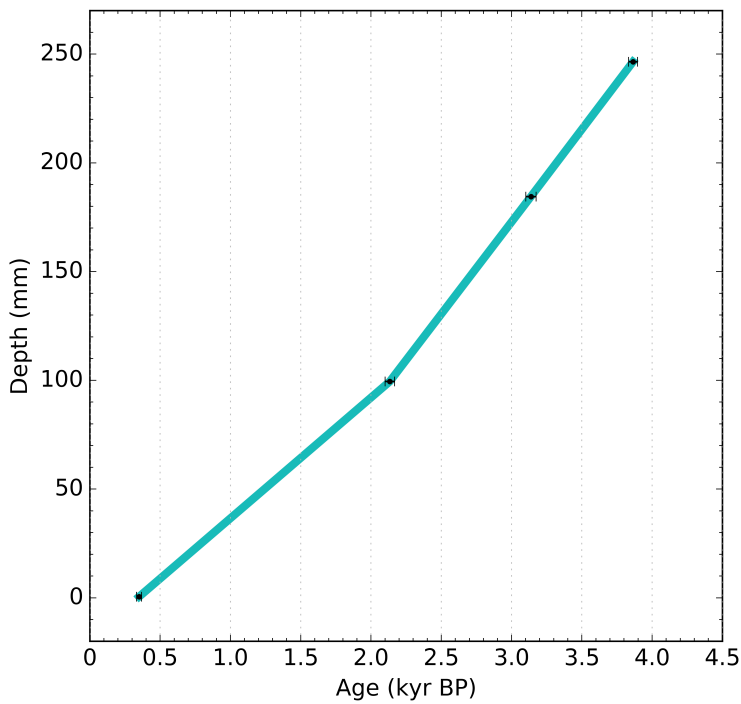
Figure 3.8. Late Holocene U/Th age model. There is assumption of linear growth.

3.4.3 Oxygen isotopes

No evidence for solution drilling and dissolution due to undersaturated caves waters was detected in 16CobbB2; these effects would have been observable as small holes borne into the top of the stalagmite due to dripwater with low pH (Lachniet 2009). The calcite is largely transparent, and appeared to have low abundances of visible detrital material. These preliminary conditions make the sample ideal for paleoclimate reconstruction work, though further investigations into fractionation concerns were conducted and are discussed later.

We measured 1059 $\delta^{18}O$ values along 70 cm of the 16CobbB2 growth axis, and excluded inclusion of data from the growth hiatus at the 150 mm mark on Piece D (**Figures 3.9, 3.10, 3.11**). The average resolution of isotope measurements for 16CobbB2 is 100 yr/sample. The $\delta^{18}O$ record has a range of 3‰, from -6.19‰ to -3.13‰ (**Tables A-2, A-3**). Combined with the U/Th chronology, our three records span continuous growth periods from 350 to 3800 yr BP, from 98 to 130 kyr BP, and from 179 to 208 kyr BP.

The Pleistocene $\delta^{18}O$ values in 16CobbB2, with dates indicating growth from ~98 to 209 kyr BP, range from -6.19‰ to -3.13‰ with an average of -4.85 ± 0.5‰ (1σ, n=790). The most pronounced fluctuations in the Pleistocene oxygen record from 16CobbB2 (**Figure 3.12**) include relative $\delta^{18}O$ minima at 108, 128, 179, and 198 kyr BP, with the most negative absolute $\delta^{18}O$ values at 108 and 128 kyr BP (-6.19‰ and -6.18‰, respectively). Observable $\delta^{18}O$ relative maxima occur at 104, 129, 186, and 201 kyr BP, with the most positive absolute $\delta^{18}O$ value at 186 kyr BP (-3.13‰). The Holocene record has dates indicating growth from ~350 to 3800 yrs BP. The Late Holocene $\delta^{18}O$ values in 16CobbB2 (**Figure 3.13**) range from -5.39‰ to -4.49‰, with an average of -4.92‰ $\pm$ 0.2‰ (1σ, n=232).
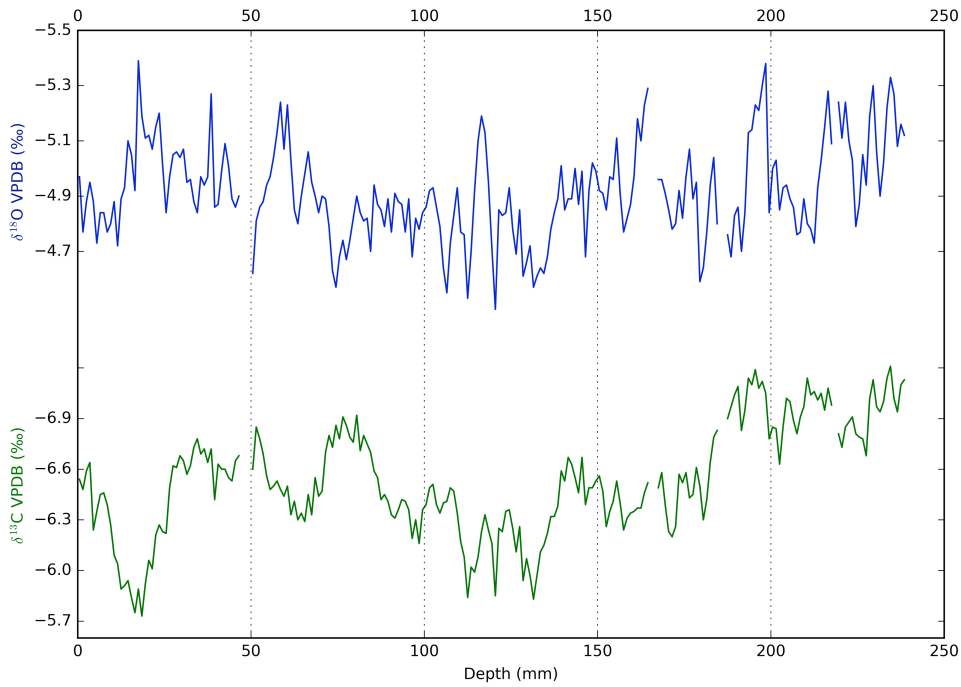
Figure 3.9. Piece A δ^{18}O (blue) and δ^{13}C (green) records versus depth (distance in mm). 0 is the top (youngest) of the piece.
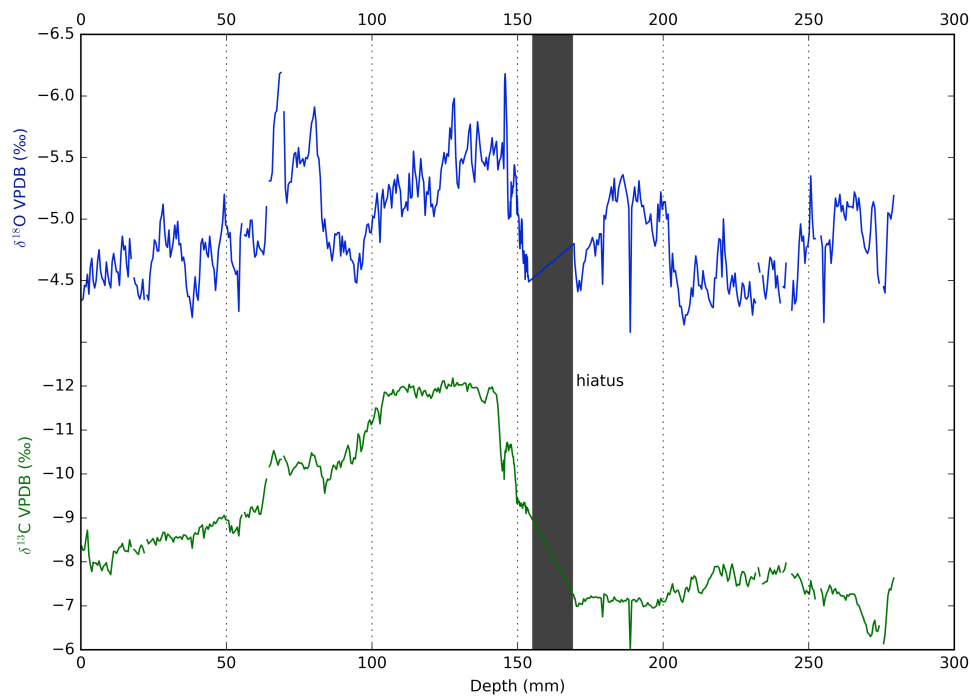
Figure 3.10. Piece D δ^{18}O (blue) and δ^{13}C (green) records versus depth (distance in mm). 0 is the top (youngest) of the piece, and the hiatus is highlighted in black.
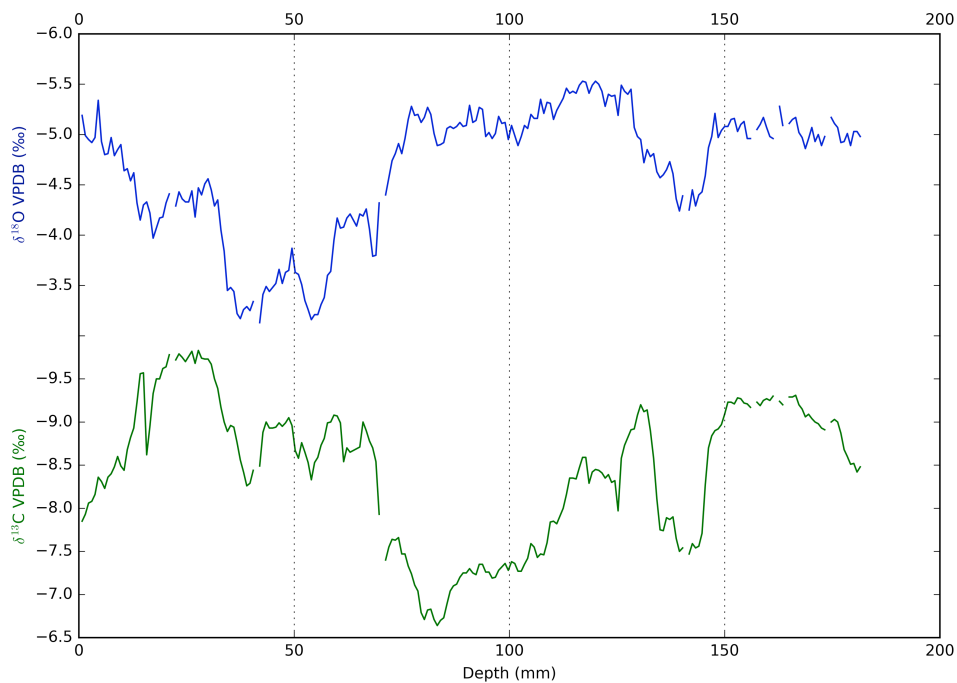
Figure 3.11. Piece E δ¹⁸O (blue) and δ¹³C (green) records versus depth (distance in mm). 0 is the top (youngest) of the piece.
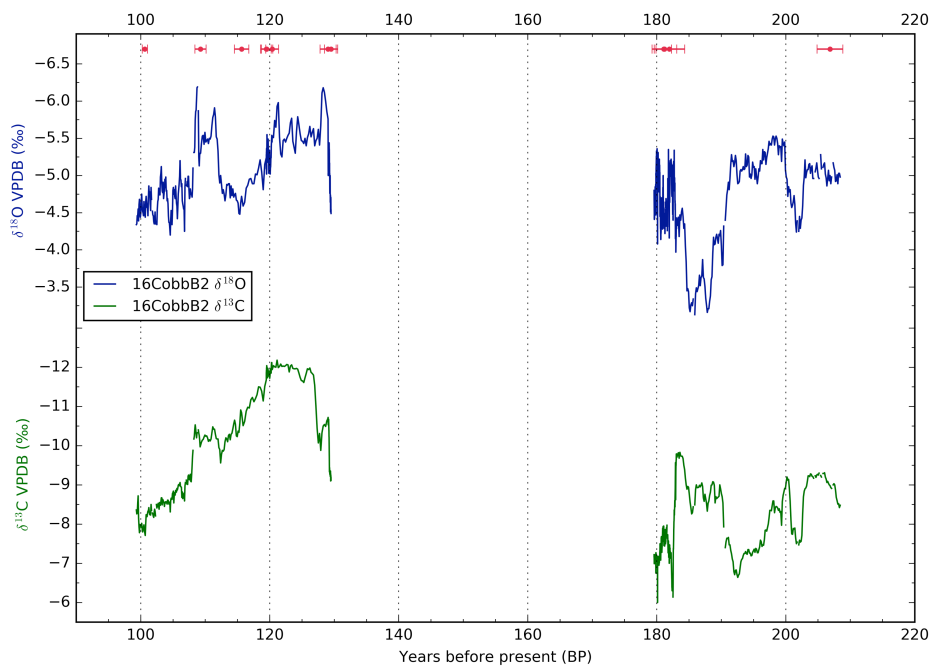
Figure 3.12. Texas Pleistocene δ¹⁸O (blue) and δ¹³C (green) records with U/Th dates. Error bars shown in pink.

63
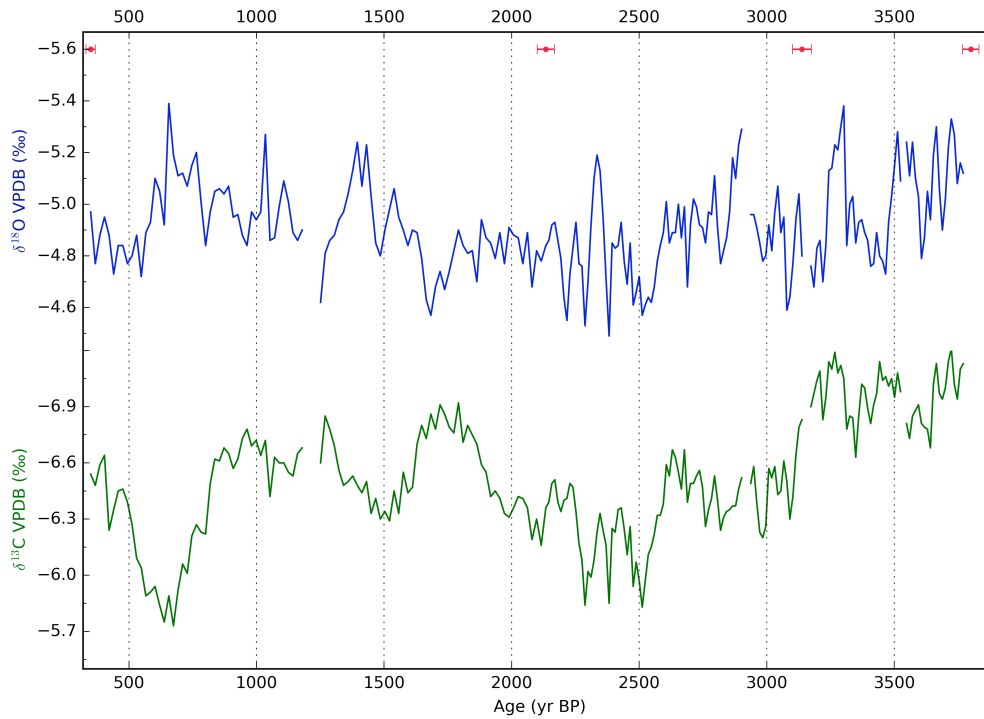
Figure 3.13. Texas Holocene δ^{18}O (blue) and δ^{13}C (green) records with U/Th dates. Error bars shown in pink.

3.4.4 Carbon isotopes

Following the same process as the oxygen record, we then measured 1059 δ^{13}C values

along 70 cm of the 16CobbB2 growth axis with an average resolution of 100 yr/sample (see

Figures 3.9, 3.10, 3.11 above). Hiatus-related isotope measurements are excluded from

discussion, and the average resolution of δ^{13}C data is 100 yr/sample. The δ^{13}C record has a larger

range of 6‰, from -12.18‰ to -5.73‰.

The Pleistocene δ^{13}C values in 16CobbB2, with dates indicating growth from ~98 to 208

kyr BP, range from −6.19‰ to −3.13‰ with an average of −4.85‰ ± 0.5‰ (1σ, n=790). The

most pronounced fluctuations (see **Figure 3.12** above) in the Pleistocene carbon record from

16CobbB2 include relative δ^{13}C minima at ~110, 120-127, 185, and 200 kyr BP, with the most

negative absolute $\delta^{18}O$ values at 108 and 128 kyr BP (-6.19‰ and -6.18‰, respectively). Observable $\delta^{13}C$ peaks in the Pleistocene record occur at ~100, 180, and 192 kyr BP. The Late Holocene $\delta^{13}C$ values in 16CobbB2 (see **Figure 3.13** above) range from −7.21‰ to −5.73‰ with an average of −6.53‰ ± 0.33‰ (1σ, n=232). The carbon isotope values in the Cobbs record generally do not align with fluctuations in the oxygen record.

3.5 Discussion

3.5.1 Fractionation

Before interpreting $\delta^{18}O$ values from 16CobbB2, it must first be established that the speleothem is reliably recording changes in the $\delta^{18}O$ of cave dripwater. To do this, we must rule out kinetic effects that could be distorting the isotopic signal. To test for kinetic effects, we have plotted two different drill paths from piece D, with one path as a Hendy path, to assess intrasample reproducibility in the speleothem. In both paths, we find a reproducible, large per mil change in both the carbon and oxygen records (**Figure 3.14**). This indicates that isotope values are not changing with distance from the locus of deposition.

We then analyzed carbon and oxygen covariation along the growth axis. Significant covariation between carbon and oxygen could be an indication of nonequilibrium deposition (Dorale and Liu 2009; Mickler et al. 2006). In our Pleistocene record, we find no significant covariation (R^2=0.13, n=790, p=0.0001) between oxygen and carbon in our sample (**Figure 3.15**). In our Holocene record, we also find no significant covariation (R^2=0.08, n=232, p=0.0001) between oxygen and carbon in our sample (**Figure 3.16**).

Covariation between carbon and oxygen values is not necessarily indicative of fractionation. Factors driving variability in speleothem $\delta^{18}O$, in this case amount of rain, can also affect bioproductivity, which ultimately alters organic matter composition and $\delta^{13}C$ values in the speleothem (Dorale and Liu 2009). However, this is not the case in 16CobbB2, as demonstrated by a clear lack of covariation between oxygen and carbon in both time periods.

This evidence, combined with monitoring results from Cobbs Cavern indicating a stable cave environment, suggests that stalagmite 16CobbB2 formed under isotopic equilibrium conditions and that kinetic effect are not affecting our samples. Thus, stalagmite $\delta^{18}O$ is reliably recording changes in rainfall $\delta^{18}O$. Based on our analysis of Austin rainfall, we interpret this as variability in the amount of precipitation reaching the SGP.
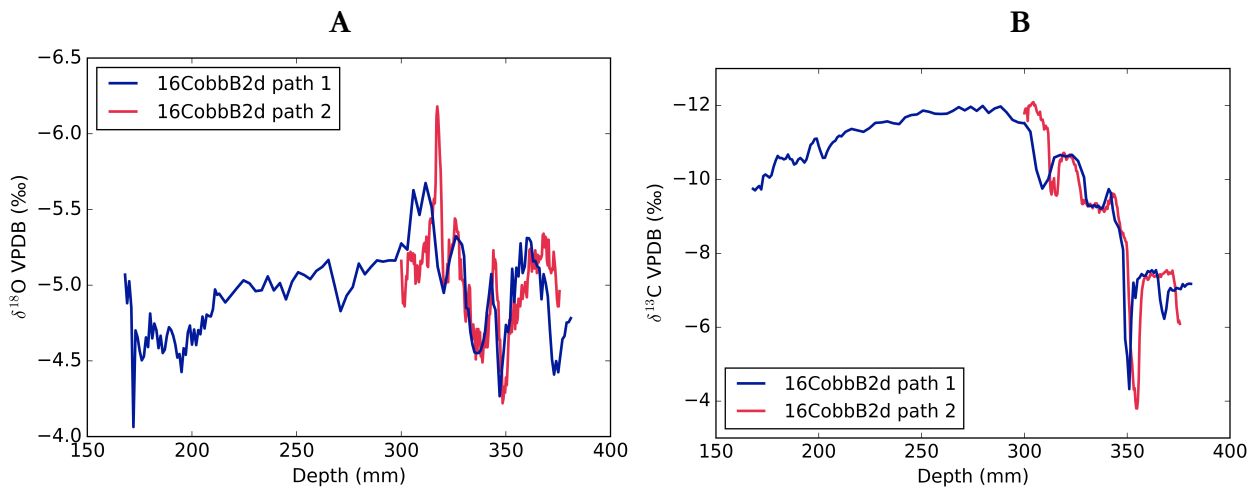
Figure 3.14. Hendy paths. Reproducibility between paths in both the oxygen (A) and carbon (B) records as indication of equilibrium deposition.
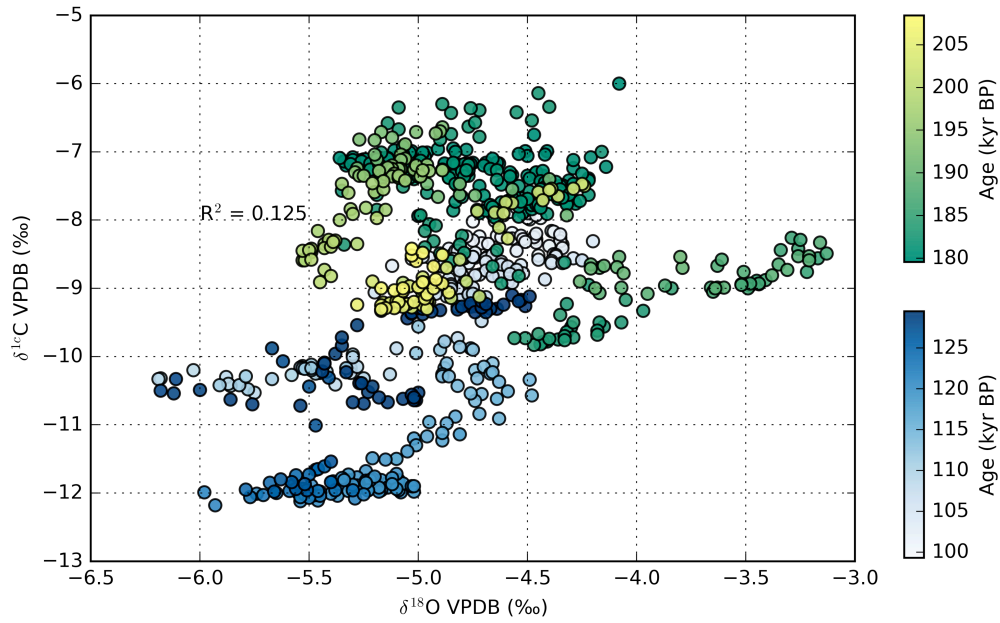
Figure 3.15. Pleistocene oxygen and carbon covariation. Comparison of Texas stalagmite isotope values along the drill path to test for covariation. The younger half of the Pleistocene record is shown in shades of blue, and the older half in green.
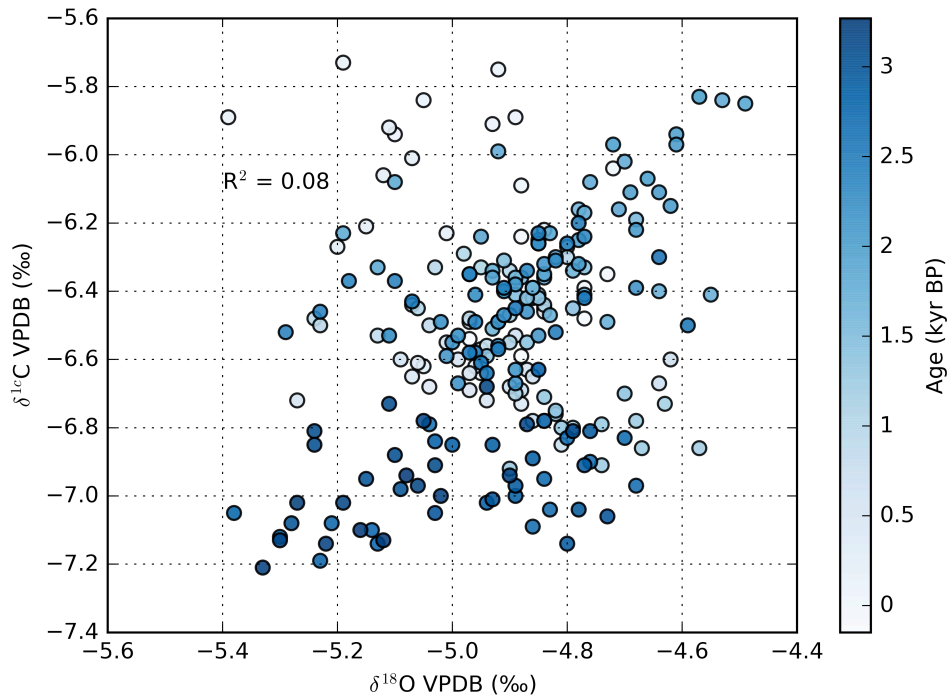
Figure 3.16. Holocene oxygen and carbon covariation. Comparison of Texas stalagmite isotope values along the drill path to test for covariation.

.

3.5.2 Oxygen isotope interpretation

During speleothem formation, temperature dependent fractionation of calcite and water, with a ratio of ~–0.20‰/°C (Kim and O'Neil 1997), and the isotopic signature of dripwater, drive $\delta^{18}O$ variability in calcite (Fleitmann et al. 2003; Asmerom et al. 2007; Baker and Bradley 2010). If temperature were the sole driver of $\delta^{18}O$ variability in 16CobbB2, cave temperature would have to change by ~15°C based on the range of oxygen isotope variability of 3.06‰ over the course of the entire record encompassing the time periods 350 to 3800 yr BP, 99 kyr to 130 kyr BP, and 179 kyr to 208 kyr BP. A 15°C shift in air temperature, even from glacial to interglacial periods, is not a plausible range of temperature change in the SGP, as estimates from coupled ocean-atmosphere simulations from the Paleoclimate Modeling Intercomparison Project (PMIP2) suggest the Last Glacial Maximum (LGM) was 2-5°C cooler than present (Braconnot et al. 2007). Tropical SST-based reconstructions of temperature variability during the LGM have shown a range of glacial cooling ranging from 1 to 5°C (Porter 2001; Waelbroeck et al. 2009). An oxygen isotope record from Atlantic corals off the coast of Barbados indicated LGM SSTs just shy of 5 °C cooler than present (Guilderson et al. 2001). Across the globe, a long-term paleotemperature speleothem record from Soreq Cave in Israel indicated LGM temperatures ~6 to 7°C cooler than present (Affek et al. 2008). A continental paleotemperature record derived from atmospheric noble gas concentrations dissolved in radiocarbon-dated groundwater in northeastern Brazil suggested LGM temperatures ~5°C cooler than modern day temperatures (Stute et al. 1995), which is in agreement with temperature reconstructions reached by other South American pollen records and snow line reconstructions (Rind and Peteet 1985). Although these temperature reconstructions exhibit a high degree of variability, none come close to the

15°C difference needed to explain isotope variability in our speleothem record if it were interpreted entirely in terms of temperature.

Monitoring efforts for Cobbs Cavern have demonstrated its stable temperature environment for growing calcite in isotopic equilibrium. Caves such as Cobbs Cavern, with no major surface expressions, generally maintain relative humidity levels near 100% (Poulson and White 1969). Therefore, the requisite ~15°C range is not reasonable given the year-round, steady temperature approximation of Williamson County MAT in Cobbs Cavern.

A lack of isotopic covariation combined with reproducible Hendy paths led us to conclude that fractionation or kinetic effects are not interfering with equilibrium deposition of speleothem calcite. We also conclude that cave temperature is not the primary driver of stalagmite δ^{18}O variability. Thus, we argue the primary control on Cobb speleothem δ^{18}O variability is the δ^{18}O value of dripwater, which we demonstrated in Chapter 2 as rainwater influenced by the "amount effect".

The temperature effect, or a direct correlation between MAT at the cave site and the average δ^{18}O value of precipitation, is statistically insignificant at Cobb based on our rainfall data (**Figure 2.7**). This means that temperature is not a major control on isotope variability in central Texas rainwater. The altitude effect, in which a decrease in δ^{18}O values occurs with an increase in altitude, is also negligible at our site because there are no orographic barriers near Cobbs Cavern. Furthermore, Cobbs is not far enough inland for the continental effect to be a major factor because the water does not travel far from the Gulf of Mexico to reach the cave site. The amount effect is the observable decrease in precipitation δ^{18}O values as the amount of rainfall increases (Lachniet 2009). As demonstrated by our rainfall data, and previous central

Texas rainfall analyses (e.g. Wong et al. 2015), the so-called "amount effect" is a significant control on the rainwater $\delta^{18}O$, and ultimately, cave dripwater $\delta^{18}O$.

Therefore, based on our complementary Austin rainfall data, we interpret more negative $\delta^{18}O$ values in the speleothem as indicative of wetter conditions, likely resulting from the presence and persistence of multiple years of climate patterns conducive to the formation of large, organized convective systems. We interpret more positive $\delta^{18}O$ values in the speleothem as indicative of drier conditions. In our Texas stalagmite oxygen record (**Figure 3.17**), we find oxygen minimums coincident with the timing of MIS 5e, the Eemian interglacial. We find oxygen maximums coincident with MIS 5d, and MIS 6a, which marks the deglacial transition from MIS 6a to MIS 5e (**Figure 3.17**).
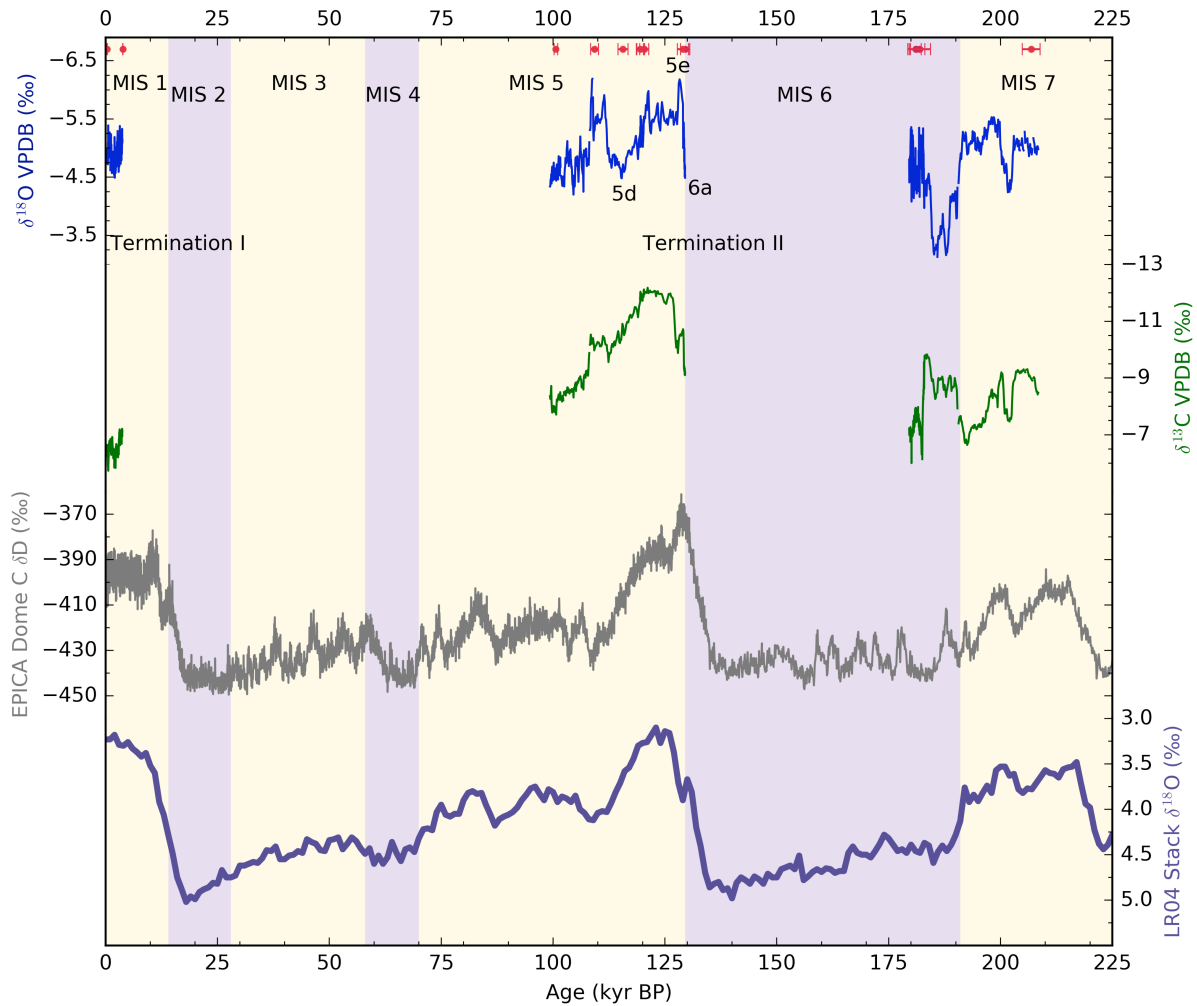
Figure 3.17. Texas speleothem record. Stalagmite oxygen (blue) and carbon (green) records with U/Th ages and associated error bars (pink). Marine Isotope Stages are labeled MIS and differentiated by the purple and gold shading. Deuterium values from EPICA Dome C (gray) and the oxygen record of the Lisiecki-Raymo benthic stack (purple) are shown to put our Texas record in global context.

3.5.3 Carbon isotope interpretation

Drivers of carbon isotope variability are less straightforward as speleothem carbon is sourced from either carbonate bedrock or CO_2 derived from the soil and atmosphere. The proportion of carbon derived from soil versus atmosphere depends on vegetation density (Hellstrom et al. 1998) and soil respiration rates (Genty et al. 2003), whereby shallow and poorly

vegetated soils get more of their CO_2 from the atmosphere (Cerling 1984, Frumkin et al. 2000).

Thus, the proportion of host rock carbon can influence speleothem $\delta^{13}C$ values (Hendy 1971;

Fairchild et al. 2006).

One of the main drivers of speleothem $\delta^{13}C$ variability is the relative abundance of C3

and C4 plants that exist above the karst area, which helps control the $\delta^{13}C$ value of soil (Dorale et

al. 1992; Fairchild et al. 2006). Differences in the chemical and physical composition of plants

allow for plants to discriminate against carbon-13 during photosynthesis. This plant-specific

preference for a particular carbon isotope is then used to differentiate among photosynthetic

groups. C3 and C4 refer to the distinct photosynthetic pathway of a plant, such that C3 plants are

not equipped with photosynthetic adaptations to reduce photorespiration, but C4 plants are.

Because C4 plants are able to more efficiently capture CO_2 at elevated leaf temperatures, these

plants are typically more heat and drought tolerant. Their $\delta^{13}C$ value is more positive than that of

their C3 counterparts due to differing isotope preferences and processes of carboxylation

(O'Leary 1988). Enrichment of ^{13}C in calcite generally reflects a higher contribution of C4 plants

to soil CO_2 and thus the $\delta^{13}C$ of speleothem calcite can reveal the relative distributions of plants

with different photosynthetic pathways directly above the cave (Cerling et al. 1984; Dorale et al.

1998). Warm season grasses such as crabgrass, as well as corn and sugarcane, fall under the C4

photosynthetic pathway and are found in desert and subtropical regions (Ehleringer 1978;

Hattersley 1983). In contrast, wetter conditions or increased moisture availability in a region

generally result in a shift toward C3 vegetation, which consists of most temperate plants and all

woody trees; this trend toward C3 vegetation leads to more negative speleothem $\delta^{13}C$ values

(Lloyd and Farquhar 1994). Consequently, C3 vegetation $\delta^{13}C$ values are more negative than C4

values (Smith and Epstein 1971; Cerling 1984).

Another major control on $\delta^{13}C$ values in speleothems is vegetation biomass, which may be affected by temperature and precipitation (Genty et al. 2006). As previously discussed, the type of vegetation overlying the karst area can influence $\delta^{13}C$ values, but so can the amount of biomass and thus biologic activity in the vicinity of the cave (Cruz et al. 2006). A pronounced decrease in speleothem $\delta^{13}C$ values may reflect enhanced biologic CO_2 production in the overlying soil due to warmer temperature and/or increased precipitation (Hellstrom et al. 1998). A speleothem record from western Australia exhibited more positive $\delta^{13}C$ values during the LGM and early deglaciation, but a steep decline in $\delta^{13}C$ values was coincident with the onset of interglacial conditions, which the authors interpreted to reflect increased plant density due to heavier rainfall periods during the early to mid Holocene (Denniston et al. 2013).

Despite this seemingly straightforward $\delta^{13}C$ signal of vegetation type and bioproductivity, complications may arise with secondary effects that can influence speleothem $\delta^{13}C$ values. First, rapid degassing of CO_2, whereby $^{12}CO_2$ preferentially escapes from oversaturated waters, may result in elevated $\delta^{13}C$ values of residual dissolved inorganic carbon (Hendy 1971, Mickler et al. 2004). Secondly, fractionation during precipitation, in which carbonate ions are incorporated into rapidly precipitating $CaCO_3$ without equilibrium isotope exchange between solid $CaCO_3$ and the solution, could also influence speleothem $\delta^{13}C$ values. Finally, as the speleothem-building calcite solution makes its way through the flowpath in the unsaturated zone, it may equilibrate with lower $_pCO_2$ conditions, which results in a process known as prior calcite precipitation (PCP) (Fairchild et al. 2000). PCP is this process by which calcite precipitates from solution before deposition on the stalagmite and may increase $\delta^{13}C$ values (Fairchild et al. 2000) Thus, elevated $\delta^{13}C$ values could be caused by enhanced PCP in the karst flow path from slower flow rates in dry conditions, whereas wetter climates may reduce the

occurrence of PCP due to more constant recharge rates (Johnson et al. 2006; Denniston et al. 2013). Temperate caves like Cobbs Cavern without a steep seasonal $_pCO_2$ gradient are less likely to form speleothems that have been influenced by the effects of PCP (Fairchild et al. 2000).

In addition, cave ventilation rates may also distort speleothem $\delta^{13}C$ values (Tremaine et al. 2011; Spötl et al. 2005). In caves where ventilation rates may fluctuate on a seasonal basis, interpretation of speleothem $\delta^{13}C$ values must take into account this variability in ventilation. However, monitoring efforts at Cobbs Cavern have demonstrated that the cave maintains an even temperature and stable, high $_pCO_2$ environment throughout the year. We have documented no evidence for these in-cave kinetic effects at Cobbs Cavern, although their potential influences should be noted.

Cobbs Cavern is located beneath a well-vegetated grassland, in which case speleothem $\delta^{13}C$ most likely reflects carbon values from the soil. We interpret more negative $\delta^{13}C$ values as indicative of wetter conditions, either through a trend toward a higher relative abundance of C3 plants over C4 plants, or increased biologic CO_2 productivity in the soil zone above the cave that result from warmer temperatures and/or increased precipitation (Hellstrom et al. 1998; Genty et al. 2006). A demonstrated lack of correlation between $\delta^{13}C$ and the $\delta^{18}O$ values (see **Figures 3.15 and 3.16**), suggests that carbon isotope variability in the speleothem does not reflect the same precipitation variability recorded in the oxygen record. There is a lack of evidence for in-cave kinetic effects in 16CobbB2 that would contaminate the isotopic signal of the speleothem calcite. The roles of kinetic fractionation and PCP on speleothem $\delta^{13}C$ values cannot be entirely eliminated, but are likely negligible in our stalagmite sample. Therefore, $\delta^{13}C$ values in 16CobbB2 are largely reflective of regional moisture availability via the amount or type of vegetative biomass that was present during speleothem formation, such that more negative

values reflect wetter conditions and more positive reflect drier conditions. A negative peak in our speleothem record coincides with MIS 5e, suggesting increased regional moisture availability, or a trend toward C3 vegetation, during this interglacial time.

Although there is no conclusive interpretation of global speleothem $\delta^{13}C$ values, previous speleothem work from similar humid continental regions has largely interpreted more negative $\delta^{13}C$ values as an indicator of wetter conditions. A U/Th dated speleothem from West Virginia recorded a precipitous decline in calcite $\delta^{13}C$ at ~122.7 kyr BP, which was interpreted as an abrupt increase in regional moisture availability coincident with the timing of MIS 5e (Springer et al. 2014). In Israel, a speleothem collected from Soreq Cave spanning 178 to 152 kyr BP, a largely glacial interval with a cold but humid Mediterranean climate where negative peaks in $\delta^{13}C$ were also interpreted as indicative of increased moisture availability and CO_2 sourced from C3 vegetation (Ayalon et al. 2002). A pollen core from central Texas indicated the presence of deciduous forest and thus wetter conditions from 3000 to 2000 yr BP, whereas after 2000 yr BP drier conditions ensued along with a shift toward C4 and savanna plants (Holloway et al. 1987). This work illustrates that vegetation shifts can occur relatively rapidly in central Texas as a result of changing climatic conditions and supports our interpretation of Cobbs $\delta^{13}C$ values as reflective of changing moisture conditions in the SGP region.

3.5.4 Ice volume correction

Because variations in global ice volume affect the oxygen isotopic composition of ocean water and ultimately global water vapor, an ice volume correction was done for the Cobbs Cavern speleothem record by subtracting estimates of seawater $\delta^{18}O$ values from speleothem $\delta^{18}O$ values. In cold periods, such as the second half of the Pleistocene record, more seawater is

locked up in large continental ice sheets. Since the isotopically lighter ^{16}O is preferentially incorporated into ice, the oceans become isotopically heavier (more positive) in oxygen during cold periods than they do during warmer periods with less global ice volume. To compensate for this, oxygen isotope values are shifted more negative according to the quantitative δ^{18}O seawater dataset generated by Waelbroeck (2010) that established a robust regression between a relative sea level (RSL) curve and long-term benthic isotope records from the North Atlantic and Equatorial Pacific to generate a dataset of ocean δ^{18}O history through the past 430 kyr.

An ice volume correction was then applied to the Pleistocene record of 16CobbB2 (**Figure 3.18**) by calculating a 95% confidence interval for the distribution of the means, using the runs test (Draper and Smith 1998) to calculate the actual degrees of freedom in the Cobbs isotope record. We found that the δ^{18}O means of the raw versus the ice-corrected dataset are indistinguishable for the first half of the Pleistocene record (98 to 130 kyr BP), which encompasses the Eemian interglacial, a time of maximum insolation to the northern hemisphere. The ice volume correction does significantly change the δ^{18}O means of the older half of the Pleistocene record (179 to 208 kyr BP), which encompasses major cold periods with substantial global ice volume such that the ice volume effect is expected to have a greater influence on δ^{18}O values.

Furthermore, the difference of means between the raw records of both Pleistocene records, 0.32‰, is equivalent to 1-2°C temperature change (Lachniet 2009) from glacial to interglacial periods. This temperature change is reasonable given other North American reconstructions and model simulations such as those from PMIP2 that find the LGM 2-5°C cooler than the modern (Rind and Peteet 1985; Stute et al. 1995; Braconnot et al. 2007). Consequently, an ice volume correction could result in canceling out a temperature effect that

may be real. We also note that the shifts toward more negative $\delta^{18}O$ values in our speleothem record during interglacial times are not affected by the ice volume correction. Although the magnitude of the range of $\delta^{18}O$ values changes with an ice volume correction, the frequency of peaks and troughs in $\delta^{18}O$ values in our speleothem record does not change, and the timing and frequency of the peaks and troughs in $\delta^{18}O$ values is the chief focus of our project.
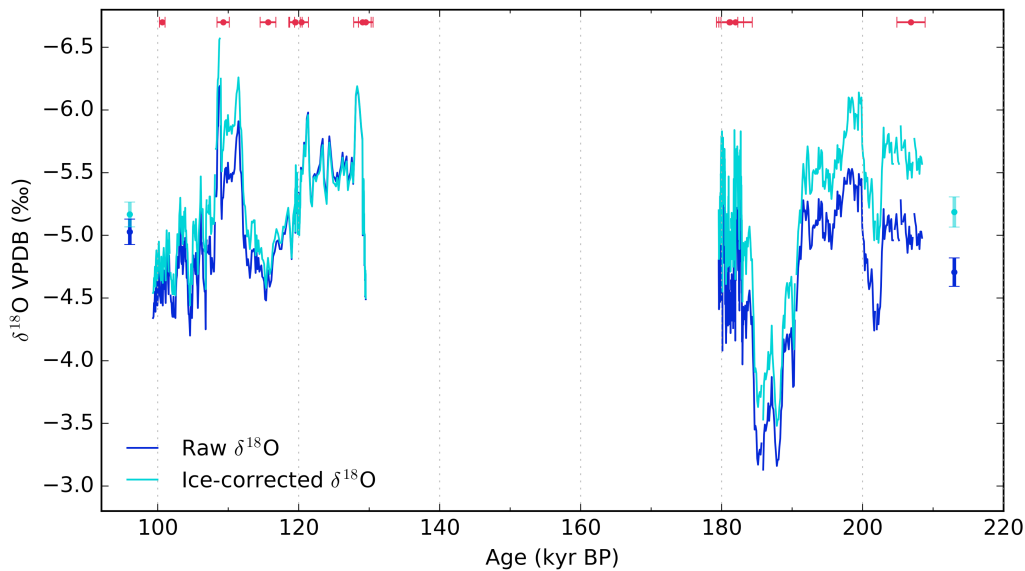
Figure 3.18. Ice volume correction of the speleothem record. Texas stalagmite raw oxygen record (dark blue) and ice-corrected record (turquoise) with distributions of each mean shown with error bars. Ice corrected values based on Waelbroeck et al. (2010) seawater $\delta^{18}O$ reconstruction.

3.5.5 Orbitally driven variability

Landmark paleoclimate work has identified variations in the earth's orbital configuration as the main mechanisms driving Quaternary ice age succession (Hays et al. 1976; Imbrie and Imbrie 1980). To investigate this, we examined our record for orbital spectral powers. We found

peaks (more negative values) in the $\delta^{18}O$ at ~108 kyr and ~128 kyr BP in the younger half of the

Pleistocene record, and peaks at approximately ~180 kyr and ~203 kyr in the older half of the

Pleistocene record. These ~20 kyr and ~23 kyr frequencies roughly align with the frequency of

an axial precession cycle. Therefore, to investigate the observed ~20-23 kyr cycle that appears in

the Cobbs oxygen record, we compared the record with NH summer insolation at 30°N (**Figure 3.19**).

Precession, one of three Milankovitch orbital parameters governing the amount of the

sun's energy reaching the earth's surface, is the result of a gyroscopic wobble of the earth on its

axis primarily due to the gravitational pull of the sun and the moon on the earth. A complete

precessional cycle generally takes 26,000 years. While undergoing this wobble, the orientation of

the earth's tilt changes relative to its plane of orbit around the sun, but the tilt itself is maintained

at a relatively constant 23.4°. Precession is an especially significant orbital component in the

low- and mid-latitudes, where it has been found to dominate climate responses to warming

(Short et al. 1991; Kim and Crowley 1994).

In monsoon climates globally, variations in solar intensity have been connected with

rainfall intensity. Speleothem $\delta^{18}O$ records from Hulu and Dongge Caves in China over the last

160 kyr have demonstrated that variations in East Asian Monsoon (EAM) strength are connected

to orbitally induced changes in insolation as EAM intensity concurrently changed with

Greenland temperature reconstructions from GISP2 (Wang et al. 2001; Wang et al. 2005).

Similarly, a Holocene speleothem $\delta^{18}O$ record from Qunf Cave in Oman also suggested a direct

relationship between monsoon precipitation variability and changes in NH summer insolation

(Fleitmann et al. 2003). In northern Africa, coupled atmosphere-ocean climate model simulations

showed increased tropical Atlantic SST in the summer as the amplitude of seasonal insolation

was increased in the mid Holocene (Kutzbach and Liu 1997). In the arid American Southwest, a Holocene speleothem $\delta^{18}O$ record from New Mexico correlates periods of increased solar activity with reduced moisture to the region, which is the opposite trend to the Asian cave records, likely due to solar activity playing a role in moderating the El Niño–Southern Oscillation (ENSO) or Pacific Decadal Oscillation (PDO) (Asmerom et al. 2007). Nevertheless, this New Mexican speleothem record further strengthens the link between solar variability and moisture availability.

Although Texas does not qualify as a monsoon climate, it nevertheless exhibits monsoon-like qualities during rainy years, with peak precipitation amounts in late spring and fall (**Figure 2.1**). Yet even in areas without a monsoon climate, solar variability has been hypothesized to be a driver speleothem isotopic variability due to its connection to increased rates of biologic activity in the soil (Frisia et al. 2003). Although the details governing orbital influences on earth processes remain unclear, solar variability undoubtedly maintains an important control on climate.

When comparing the Cobbs oxygen record with summer insolation, we find that our oxygen record aligns with peak to trough timing of changes in NH insolation on glacial-interglacial timescales. Minima in the $\delta^{18}O$ record match maxima of precession-paced annual summer insolation at 30°N. This alignment suggests that one of the drivers of large changes in our oxygen record, and thus wetter versus drier periods in the SGP, is NH insolation. Therefore, our Pleistocene Texas speleothem record agrees with conclusions reached by other major speleothem records in that variability in NH insolation exerts some degree of control on large changes in rainfall intensity.
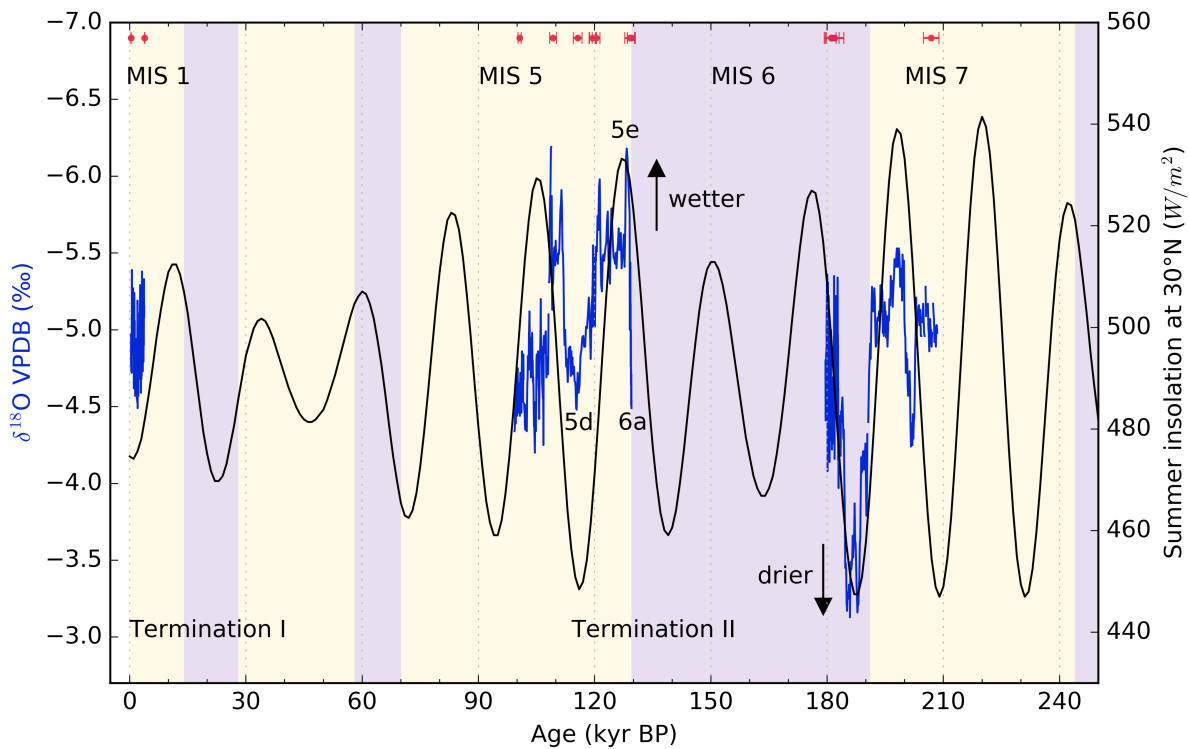
Figure 3.19. Orbitally driven rainfall variability. Texas stalagmite oxygen record (blue) with U/Th ages (pink) and northern hemisphere summer insolation at 30°N (black). Glacial terminations are noted. More negative $\delta^{18}O$ are interpreted as indicative of wetter conditions, and more positive values drier.

3.5.6 MIS 5e – The Eemian

MIS 5e, also known as The Eemian Interglacial, was the penultimate interglacial period. During this time, temperatures were as much as 2°C warmer, (Shackleton 2002), sea level 4-6m higher (Bard et al. 1990), and ice sheets less extensive (Cuffey and Marshall 2000) than modern day. The orbital position of the earth was such that NH summer heating was greater than present (Berger and Loutre 1991). This indicates that MIS 5e may serve as a potential analogue for future warming scenarios.

To examine the moisture conditions of the modern versus those of MIS 5e, we compared the 3500 years of MIS 5e with the most negative $\delta^{18}O$ values in our oxygen record to our 3500 years of data from the late Holocene (**Figure 3.20**). Here it is important to note that the ice volume correction, mentioned above, did not significantly alter Cobbs $\delta^{18}O$ during MIS 5e and that is why we use the raw $\delta^{18}O$ record here. A 2x standard error distribution of the mean was calculated, using the runs test (Draper and Smith 1998) to estimate degrees of freedom. The calculated distributions of the means from our 3500 years of data in the late Holocene and 3500 years from the height of MIS 5e do not overlap, indicating a significant difference between the mean $\delta^{18}O$ values of MIS 5e versus our late Holocene data. Furthermore, because the average $\delta^{18}O$ value of MIS 5e (-5.66‰) is significantly more negative than the average value of the late Holocene data (-4.91‰), we suggest that MIS 5e was a wetter time period with more frequent, more intense, and/or more organized convective storm systems in the SGP than the late Holocene.

Although little hydroclimate work extending as far back as MIS 5e has been done in the SGP, modern model scenarios and reanalyses of historical weather data (e.g. Lorenz and DeWeaver 2007; Archer and Caldeira 2008) provide evidence for a northward shift of the polar jet stream in response to global warming, such as during peak interglacial conditions similar to those in MIS 5e. Previous paleoclimate work in North America further supports this conclusion, such as the work of Asmerom et al. (2010) in which the authors use a New Mexican speleothem $\delta^{18}O$ record to conclude that temperature changes in the northern hemisphere result in latitudinal displacement of the polar jet stream and the ITCZ, which indicates a more arid North American Southwest in response to warming. However, moisture conditions in the US Southwest are generally out of phase with those in the SGP region due to the path of the jet stream and the

difference in moisture origin, which is the Pacific Ocean for the southwestern US but the Gulf of Mexico for the SGP. Nevertheless, a potential mechanism driving increased SGP rainfall during MIS 5e, and a probable explanation for more negative MIS 5e $\delta^{18}O$ values relative to the modern, is a shift of the polar jet stream such that it was situated more directly over the SGP region during MIS 5e than its Holocene position.

Shifts in this upper level jet, which delivers synoptic support for thunderstorm formation, could also affect the extent of the GPLLJ, which is responsible for sustaining synoptic lift in the SGP, and therefore deliver greater amounts of precipitation through the formation of MSCs in the SGP region (Wang et al. 2013; Barandarian et al. 2013). Increased regional low-level moisture advection by the GPLLJ has been suggested as a driving force for simulated modern rainfall increases in the central US (Cook et al. 2008). The intensification of jet formation, sustained at length, is hypothesized as the mechanism responsible for the 1993 Midwest floods (Arritt et al. 1997). An unusually strong jet in the SGP region, associated with increased rates of precipitation and flood events (Cook et al. 2008), could be related to the northward shift of the polar jet stream and thus responsible in part for greater amounts of rainfall during the warm MIS 5e period in the SGP.

Another potential mechanism to explain increased rainfall during warm events is enhanced zonal gradients over the SGP that could be due increased regional temperatures. In central North America, horizontal geopotential height gradients shift from predominantly meridional to largely zonal as the Bermuda high shifts farther west during the warmer months (Cook et al. 2008). This further strengthens the jet, resulting in increased rates of precipitation, likely through more organized storm system formation, in the central US. During warm MIS 5e,

enhanced zonal gradients over the SGP may have strengthened the jet and resulted in an anomalously wet period in the region.

Although the lack of concurrent paleoclimate reconstructions precludes us from deriving a robust conclusion to explain a wetter MIS 5e than present, previous evidence of shifts in the polar jet and changes in geopotential height gradients during warm periods suggest these factors could be at play in delivering greater amounts of precipitation to the SGP region. MIS 5e interglacial conditions likely led to intensification of the GPLLJ and/or a latitudinal shift of the polar jet stream, which resulted in less moisture delivery to the US Southwest (Asmerom et al. 2010) but greater moisture delivery to the SGP.
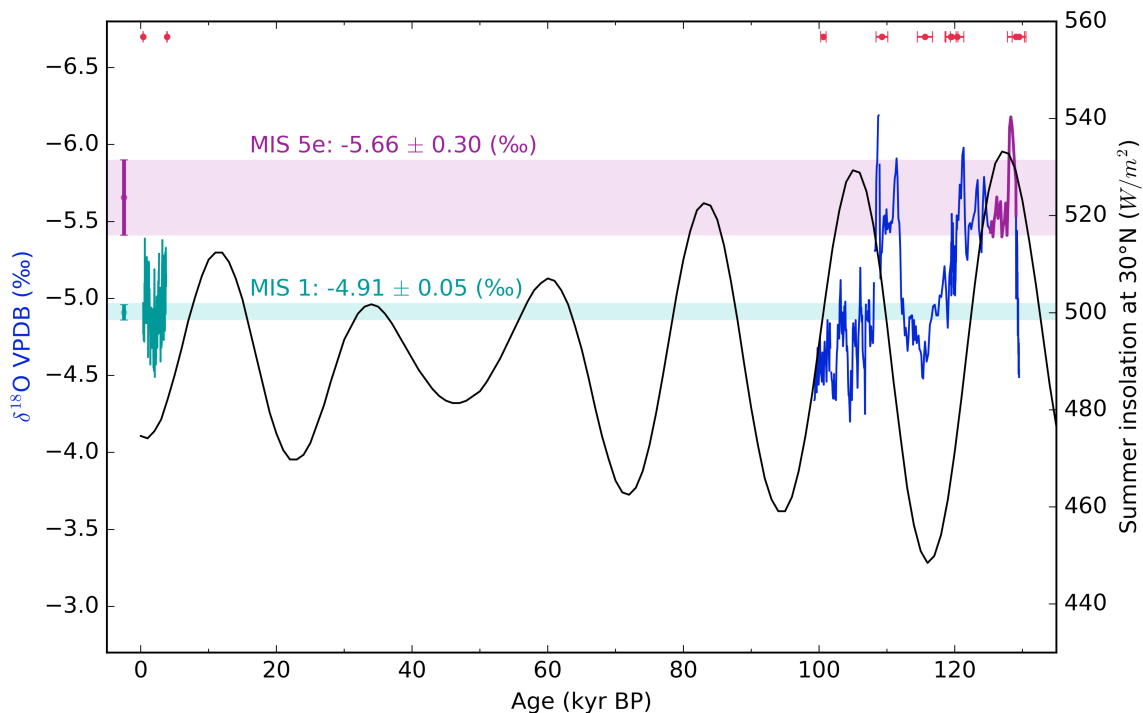
Figure 3.20. Moisture conditions in MIS 5e versus the modern. The 3500 wettest years of the Texas stalagmite record for MIS 5e (purple) compared with the 3500 years of data for the late Holocene (green). Distributions of the means are shaded in the appropriate color and each denoted with an error bar.

3.6 Conclusions

This speleothem record contributes to a clearer understanding of large-scale rainfall patterns in the SGP region. There is little to no evidence for kinetic effects or fractionation in our speleothem, leading us to conclude that the stalagmite likely formed under conditions of isotopic equilibrium. Dripwater $\delta^{18}O$ thus serves as a true reconstruction of rainwater $\delta^{18}O$. Variability in amount of rainfall is the primary control on $\delta^{18}O$ variability in Cobbs Cavern calcite.

Controls on the carbon record are less straightforward than oxygen. We cannot totally rule out PCP or kinetic effects. However, we suggest that a combination of biologic factors such as vegetation type overlying the karst area and soil bioproductivity are important drivers of $\delta^{13}C$ variability in the speleothem.

Our central Texas stalagmite $\delta^{18}O$ records SGP hydrologic response to a changing climate. We suggest that interglacials correspond to wetter conditions in the SGP, likely due to increased water vapor penetrating into the SGP as well as polar jet movement such that it delivers more cold fronts to the region, which act as lifting mechanisms for warm Gulf of Mexico air and result in more persistent, frequent, and intense convective storm activity. Furthermore, the $\delta^{18}O$ variability roughly follows maximum insolation at 30°N from 98-130 kyr BP and 179-208 kyr BP. This suggests NH insolation as a potential driver of large changes in our oxygen record, and thus, regional large-scale rainfall variability. After comparison of past interglacial with modern (late Holocene) data, we find our record provides evidence for increased precipitation under past warming conditions. If we assume that rainfall variability will continue to follow NH insolation, then with the calculated future rise in insolation, combined with predicted anthropogenic warming, we suggest a wetter SGP into the future.

3.7 References

Affek, H.P., Bar-Matthews, M., Ayalon, A., Matthews, A., and J.M. Eiler. 2008. Glacial/interglacial temperature variations in Soreq cave speleothems as recorded by 'clumped isotope' thermometry, *Geochimica et Cosmochimica Acta* 72 (22):5351-5360.

Archer, C. L. and K. Caldeira. 2008. Historical trends in the jet streams. *Geophys. Res. Lett*. 35: L08803.

Arritt, R.W., Rink, T.D., Segal, M., Todey, D.P., Clark, C.A., Mitchell, M.J., and K.M. Labas.1997. The Great Plains low-level jet during the warm season of 1993, *Monthly Weather Review* 125: 2176-2192.

Asmerom, Y., Polyak, V., Burns, S, and J. Rasmussen. 2007. Solar forcing of Holocene climate: New insights from a speleothem record, southwestern United States, *Geological Society of America* 35(1): 1-4.

Asmerom, Y., V. J. Polyak, and S. J. Burns. 2010. Variable winter moisture in the southwestern United States linked to rapid glacial climate shifts, *Nature Geoscience* 3(2): 114-117.

Ayalon, A., Bar-Matthews, M., and A. Kaufman. 2002. Climatic conditions during marine oxygen isotope stage 6 in the eastern Mediterranean region from the isotopic composition of speleothems of Soreq Cave, Israel, *Geology* 30(4): 303-306.

Barandiaran, D., S.-Y. Wang, and K. Hilburn. 2013. Observed trends in the Great Plains low-level jet and associated precipitation changes in relation to recent droughts, *Geophysical Research Letters* 40(23): 6247–6251.

Bard, E., Hamelin, E., and R.G. Fairbanks. 1990. U-Th ages obtained by mass spectrometry in corals from Barbados: sea level during the past 130,000 years, *Nature* 346: 456-58.

Basara, J. B., J. N. Maybourn, C. M. Peirano, J. E. Tate, P. J. Brown, J. D. Hoey, and B. R. Smith. 2013. Drought and associated impacts in the Great Plains of the United States—A review. *International Journal of Geosciences* 4: 72–81.

Berger, A. and M.F. Loutre. 1991. Insolation values for the climate of the last 10 million of years, *Quaternary Science Reviews* 10: 297-317.

Blum, M. D., R. S. Toomey III, and S. Valastro Jr. 1994. Fluvial response to Late Quaternary climatic and environmental change, Edwards Plateau, Texas, *Palaeogeography, Palaeoclimatology, Palaeoecology* 108: 1–21.

Braconnot, P., Otto-Bliesner, B., Harrison, S., Joussaume, S., Peterchmitt, J.-Y., Abe-Ouchi, A., Crucifix, M., Driesschaert, E., Fichefet, T., Hewitt, C.D., Kageyama, M., Kitoh, A., Laîné, A., Loutre, M.-F., Marti, O., Merkel, U., Ramstein, G., Valdes, P., Weber, L., Yu, Y., Zhao, Y., 2007. Results of PMIP2 coupled simulations of the Mid-Holocene and Last

Glacial Maximum - Part 1: experiments and large-scale features, *Climate of the Past* 3: 261-277.

Cheng, H., R. L. Edwards, A. Sinha, C. Spötl, L. Yi, S. Chen, M. Kelly, G. Kathayat, X. Wang, X. Li, X. Kong, Y. Wang, Y. Ning, and H. Zhang. 2016. The Asian monsoon over the past 640,000 years and ice age terminations, *Nature* 534(7609): 640-646.

Cerling, C. E. 1984. The stable isotopic composition of modern soil carbonate and its relationship to climate, *Earth and Planetary Science Letters* 71: 229-40.

Cleaveland, M.K., Votteler, T.H., Stahle, D.K., Casteel, R.C. and J.L. Banner. 2011. Extended Chronology of Drought in South Central, Southeastern and West Texas, *Texas Water Journal* 2(1): 54-96.

Cook, K. H., E. K. Vizy, Z. S. Launer, and C. M. Patricola. 2008. Springtime intensification of the Great Plains Low-Level Jet and midwest precipitation in GCM simulations of the twenty-first century, *Journal of Climate*, 21(23): 6321–6340.

Craig, H. 1957. Isotopic standards for carbon and oxygen and correction factors for mass-spectrometric analysis of carbon dioxide, *Geochimica et Cosmochimica Acta* 12: 133–149.

Cruz, F.W., Burns, S.J., Karmann, I., Sharp, W.D., Vuille, M., Cardoso, A.O., Ferrari, J.A., Silva Dias, P.L., Viana, O. 2005. Insolation-driven changes in atmospheric circulation over the past 116,000 years in subtropical Brazil, *Nature* 434: 63–66.

Cruz, F. W., S. J. Burns, I. Karmann, W. D. Sharp, M. Vuille, and J. A. Ferrari. 2006. A stalagmite record of changes in atmospheric circulation and soil processes in the Brazilian subtropics during the Late Pleistocene, *Quaternary Science Reviews* 25(21-22), 2749-61.

Cuffey, K.M. and S.J. Marshall. 2000. Substantial contribution to sea-level rise during the last interglacial from the Greenland ice sheet, *Nature* 404: 591-94.

Dansgaard, W., S. J. Johnsen, H. B. Clausen, D. Dahl-Jensen, N. S. Gundestrup, C. U. Hammer, C. S. Hvidberg, J. P. Steffensen, A. E. Sveinbjornsdottir, J. Jouzel, and G. Bond. 1993. Evidence for general instability of past climate from a 250-kyr ice-core record, *Nature* 364: 218-220.

Denniston, R.F., Asmerom, Y., Lachniet, M., Polyak, V.J., Hope, P., An, N., Rodzinyak, K., Humphreys, W.F. 2013. A last glacial maximum through middle Holocene stalagmite record of coastal Western Australia climate, *Quat. Sci. Rev.* 77, 101-112.

Dorale, J.A., Gonzalez, L., Reagan, M.K., Pickett, D., Murrell, M.T., Baker, R.G. 1992. A high-resolution record of Holocene climate change in speleothem calcite from Cold Water Cave, northeast Iowa, *Science* 258: 1626-30.

Dorale, J.A., R. Edwards, E. Ito, and L. Gonzalez. 1998. Climate and vegetation history of the midcontinent from 75 to 25 ka: A speleothem record from Crevice Cave, Missouri, USA, *Science* 282(5395): 1871–1874.

Dorale, J.A., Edwards, R.L., Alexander, E.C. Jr., Shen, C.-C., Richards, D.A., and H. Cheng. 2004. Uranium-series dating of speleothems: current techniques, limits, & applications. In: Sasowsky, I.D., Mylroie, J. (eds) <u>Studies of Cave Sediments</u>. Springer, Boston, MA.

Dorale, J. A. and Z. Liu. 2009. Limitations of Hendy Test criteria in judging the paleoclimatic suitability of speleothems and the need for replication, *Journal of Cave and Karst Studies* 71: 73-80.

Draper, N.R. and H. Smith. 1998. Applied Regression Analysis, Third Ed. Wiley-Interscience Publication, New York.

Ehleringer, J. 1978. Implications of quantum yield differences on the distributions of C3 and C4 grasses, *Oecologia* 31: 255-267.

Fairchild, I.J., Borsato, A., Tooth, A.F., Frisia, S., Hawkesworth, C.J., Huang, Y.M., McDermott, F., Spiro, B. 2000. Controls on trace element (Sr-Mg) compositions of carbonate cave waters: implications for speleothem climatic records, *Chemical Geology* 166: 255-269.

Fairchild, I.J., Smith, C.L., Baker, A., Fuller, L., Spötl, C., Mattey, D., McDermott, F. 2006. Modification and preservation of environmental signals in speleothems, *Earth-Science Reviews* 75: 105–153.

Faure, G. 1986. Principles of Isotope Geology, John Wiley and Sons: New York, NY.

Feng, W., B. F. Hardt, J. L. Banner, K. J. Meyer, E. W. James, M. Musgrove, R. L. Edwards, H. Cheng, and A. Min. 2014. Changing amounts and sources of moisture in the U.S. southwest since the Last Glacial Maximum in response to global climate change, *Earth and Planetary Science Letters* 401(C): 47–56.

Fleitmann D., Burns, S.J., Mudelsee, M., Neff, U., Kramers, J., Mangini, A., and A. Matter. 2003. Holocene forcing of the Indian monsoon recorded on a stalagmite from southern Oman, *Science* 300: 1737–1739.

Fleitmann, D., S. J. Burns, A. Mangini, M. Mudelsee, J. Jramers, I. Villa, U. Neff, A. A. Al-Subbary, A. Buettner, D. Hippler, A. Matter. 2007. Holocene ITCZ and Indian monsoon dynamics recorded in stalagmites from Oman and Yemen (Socotra), *Quaternary Science Reviews* 26(1): 170-188.

Frisia, S., Borsato, A., Preto, N., and F. McDermott. 2003. Late Holocene annual growth in three Alpine stalagmites records the influence of solar activity an the North Atlantic Oscillation on winter climate, *Earth Planet. Sc. Lett*., 216: 411–424.

Genty, D., Blamart, D., Ouahdi, R., Gilmour, M., Baker, A., Jouzel, J., Van-Exter, S. 2003. Precise dating of Dansgaard-Oeschger climate oscillations in western Europe from stalagmite data, *Nature* 421: 833-837.

Genty, D., D. Blamart, B. Ghaleb, V. Plagnes, C. Causse, M. Bakalowicz, K. Zouari, N. Chkir, J. Hellstrom, K. Wainer, and F. Bourges. 2006. Timing and dynamics of the last deglaciation from European and North African delta C-13 stalagmite profiles— Comparison with Chinese and South Hemisphere stalagmites, *Quaternary Science Reviews* 25(17-18), 2118-42.

Gillieson, D. 1996. Caves: Processes, Development, Management. Blackwell, Malden, MA.

Gonfiantini, R. 1978. Standards for stable isotope measurements in natural compounds, *Nature* 271: 534–536.

Guilderson, T., Fairbanks, R. & J. Rubenstone. 2001. Tropical Atlantic coral oxygen isotopes; glacial-interglacial sea surface temperatures and climate change, *Mar. Geol.* 172: 75–89.

Hattersley, P.W. 1983. The distribution of C3 and C4 grasses in Australia in relation to climate, *Oecologia* 57(1/2): 113-128.

Hendy, C. H. 1971. The isotopic geochemistry of speleothems: 1. Calculation of effects of different modes of formation on the isotopic composition of speleothems and their applicability as palaeoclimatic indicators, *Geochimica et Cosmochimica Acta* 35: 801-824.

Higgins, R.W., et al. 1997. Influence of the Great Plains low-level jet on summertime precipitation and moisture transport over the central United States, *Journal of Climate* 10: 481-507.

Houze, R. A. 2004. Mesoscale convective systems, *Reviews of Geophysics* 42(4): RG4003.

Imbrie, J., and J.Z. Imbrie. 1980. Modeling the Climatic Response to Orbital Variations, *Science* 207: 943-53.

IPCC, 2014: Climate Change 2014: Synthesis Report. Contribution of Working Groups I, II and III to the Fifth Assessment Report of the Intergovernmental Panel on Climate Change [Core Writing Team, R.K. Pachauri and L.A. Meyer (eds.)]. IPCC, Geneva, Switzerland, 151 pp.

Johns, R.H. 1993. Meteorological conditions associated with bow echo development in convective storms, *Weather and Forecasting* 294(8): 294-299.

Johnson, K.R., Hu, C.Y., Belshaw, N.S., and Henderson, G.M. 2006. Seasonal trace element and stable-isotope variations in a Chinese speleothem: the potential for high-resolution paleomonsoon reconstruction, Earth Planet. Sci. Lett. 244: 394-407.

Hays, J.D., Imbrie, J., and N.J. Shackleton. 1976. Variations in the Earth's Orbit: Pacemaker of the Ice Ages, *Science* 194(4270): 1121-32.

Hellstrom, J., Mcculloch, M., Stone, J. 1998. A detailed 31,000-year record of climate and vegetation change, from the isotope geochemistry of two New Zealand speleothems, *Quaternary Research* 50(2): 167-78.

Holloway, R.G., Raab, L.M., and R. Stuckenrath. 1987. Pollen analysis of late Holocene sediments from a Central Texas bog, *Tex. J. Sci*. 39: 71-80.

Kim, K.Y., and T.J. Crowley. 1994. Modeling the climate effect of unrestricted greenhouse emissions over the next 10,000 years, *Geophysical Research Letters*, 21(8): 681-84.

Kim, S.-T. and J. R. O'Neil. 1997. Equilibrium and nonequilibrium oxygen isotope effects in synthetic carbonates, *Geochimica et Cosmochimica Acta* 61: 3461–3475.

Kunkel, K. E. et al. 2013. Regional Climate Trends and Scenarios for the U.S. National Climate Assessment Part 4. Climate of the U.S. Great Plains, NOAA Technical Report NESDIS 142-4: 1–91.

Kutzbach, J.E., and Z. Liu. 1997. Response of the African Monsoon to Orbital Forcing and Ocean Feedbacks in the Middle Holocene, *Science* 278(5337): 440-43.

Lachniet, M. S. 2009. Climatic and environmental controls on speleothem oxygen isotope values, *Quaternary Science Reviews* 28(5-6): 412–432.

Lorenz, D. J., and E.T. DeWeaver. Tropopause height and zonal wind response to global warming in the IPCC scenario integrations, *J. Geophys. Res*. 112: D10119.
Lloyd, J. and G. D. Farquhar. 1994. ^{13}C discrimination during CO_2 assimilation by the terrestrial biosphere, *Oecologia* 99(3/4): 201-215.

Mickler, P.J., Stern, L.A. and J.L. Banner. 2006. Large kinetic isotope effects in modern speleothems, *GSA Bulletin* 118: 65-81.

Mo, K., M. Chelliah, M. Carrera, R. Higgins, and W. Ebisuzaki. 2005. Atmospheric moisture transport over the United States and Mexico as evaluated in the NCEP regional reanalysis, *Journal of Hydrometeorology* 6(5): 710–728.

O'Leary, M. 1988. Carbon Isotopes in Photosynthesis, *BioScience* 38(5): 328-336.

Partin, J. W., K. M. Cobb, and J. L. Banner. 2008. Climate variability recorded in tropical and sub-tropical speleothems, *PAGES* 16(3): 2.

Petit, J. R., J. Jouzel, D. Raynaud, N. I. Barkov, J.-M. Barnola, I. Basile, M. Bender, J. Chappellaz, M. Davis, G. Delaygue, M. Delmotte, V. M. Kotlyakov, M. Legrand, V. Y. Lipenkov, C. Lorius, L. Pépin, C. Ritz, E. Saltzman, and M. Stievenard. 1999. Climate and atmospheric history of the past 420,000 years from the Vostok ice core, Antarctica, *Nature* 399: 429-436.

Porter, S.C. 2001. Snowline depression in the tropics during the Last Glaciation. *Quat. Sci. Rev.* 20: 1067-1091.

Poulson, T.L., and W.B. White, 1969. The cave environment, *Science* 165: 971–981.

Rind, D. and D. Peteet. 1985. Terrestrial Conditions at the Last Glacial Maximum and CLIMAP Sea-Surface Temperature Estimates: Are They Consistent?, *Quaternary Research* 24: 1-22.

Rosenberg, N. J., D. J. Epstein, D. Wange, L. Vail, R. Srinivasan, J. G. Arnold. 1999. Possible Impacts of Global Warming on the Hydrology of the Ogallala Aquifer Region, *Climatic Change* 42(4): 677-692.

Shackleton, N. J., F. Sánchez-Goñi, D. Pailler, and Y. Lancelot. 2002. Marine Isotope Substage 5e and the Eemian Interglacial, *Global and Planetary Change* 36:151-155.

Shen, C.-C., Cheng, H., Edwards, R.L., Moran, S.B., Edmonds, H.N., Hoff, J.A., and R.B. Thomas. 2003. Measurement of attogram quantities of ^{231}Pa in dissolved and particulate fractions of seawater by isotope dilution thermal ionization mass spectroscopy, *Analytical Chemistry* 75: 1075–1079.

Shen, C.-C., Edwards, R.L., Cheng, H., Dorale, J.A., Thomas, R.B., Bradley Moran, S., Weinstein, S.E., and H.N. Edmonds. 2002. Uranium and thorium isotopic and concentration measurements by magnetic sector inductively coupled plasma mass spectrometry, *Chemical Geology* 185: 165–178.

Shen, C.-C. et al. 2012. High-precision and high-resolution carbonate 230Th dating by MC-ICP-MS with SEM protocols, *Geochimica et. Cosmochima Acta*, 99(C): 71–86.

Short, D.A., Mengel, J.G., Crowley, T.J., Hyde, W.T., and G.R. North. 1991. Filtering of Milankovitch cycles by earth's geography, *Quaternary Research* 35(2): 157-73.

Smith, B.N. and S. Epstein. 1971. Two categories of 13C/12C ratios for higher plants, *Plant Physiology* 47: 380-84.

Spotl, C., Fairchild, I., Tooth, A. 2005. Cave air control on dripwater geochemistry, Obir Caves (Austria): implications for speleothem deposition in dynamically ventilated caves, *Geochim. Cosmochim. Acta* 69, 2451-68.

Springer, G.S., Rowe, H.D., Hardt, B., Cheng, H., Edwards, R.L. 2014. East central North America climates during marine isotope stages 3–5, *Geophysical Research Letters* 41(9): 3233-37.

Stahle, D.W., Cook, E.R., Burnette, D.J., Villanueva, J., Cerano, J., Burns, J.N., Griffin, D., Cook, B.I., Acuna, R., Torbenson, M.C.A., Sjezner, P., and I.M. Howard. 2016. The Mexican Drought Atlas: Tree-ring reconstructions of the soil moisture balance during the late pre-Hispanic, colonial, and modern eras, *Quaternary Science Reviews* 149: 34-60.

Stute, M., Forster, M., Frischkorn, H., Serejo, A., Clark, J.F., Schlosser, P., Broecker, W.S., and G. Bonani. 1995. Cooling of Tropical Brazil (5°) During the Last Glacial Maximum, *Science* 269: 379-383.

Sundqvist, H. S., K. Holmgren, and S.-E. Lauritzen. 2007. Stable isotope variations in stalagmites from northwestern Sweden document climate and environmental changes during the early Holocene, *The Holocene* 17(2): 259–267.

Tremaine, D.M., Froelich, P.N., Wang, Y. 2011. Speleothem calcite farmed in situ: modern calibration of d18O and d13C paleoclimate proxies in a continuously monitored natural cave system, *Geochim. Cosmochim. Acta* 75: 4929-50.

Tuttle, J. D., and C. A. Davis. 2006. Corridors of warm season precipitation in the central United States, *Mon. Weather Rev*. 134(9): 2297–2317.

Waelbroeck, C., Paul, A., Kucera, M., Rosell-Melee, A., Weinelt, M., Schneider, R., Mix, A.C., Abelmann, A., Armand, L., Bard, E., Barker, S., Barrows, T.T., Benway, H., Cacho, I., Chen, M.T., Cortijo, E., Crosta, X., de Vernal, A., Dokken, T., Duprat, J., Elderfield, H., Eynaud, F., Gersonde, R., Hayes, A., Henry, M., Hillaire-Marcel, C., Huang, C.C., Jansen, E., Juggins, S., Kallel, N., Kiefer, T., Kienast, M., Labeyrie, L., Leclaire, H., Londeix, L., Mangin, S., Matthiessen, J., Marret, F., Meland, M., Morey, A.E., Mulitza, S., Pflaumann, U., Pisias, N.G., Radi, T., Rochon, A., Rohling, E.J., Sbaffi, L., Schafer-Neth, C., Solignac, S., Spero, H., Tachikawa, K., Turon, J.L. 2009. Constraints on the magnitude and patterns of ocean cooling at the Last Glacial Maximum. *Nat. Geosci*. 2: 127-132.

Waelbroeck, C., et al. 2010. Sea-level and Deep Water Temperature 430KYr Reconstructions. IGBP PAGES/World Data Center for Paleoclimatology Data Contribution Series # 2010-126. NOAA/NCDC Paleoclimatology Program, Boulder CO, USA.

Wagner, J. D. M., J. E. Cole, J. W. Beck, P. J. Patchett, G.M. Henderson, and H. R. Barnett. 2010. Moisture variability in the southwestern United States linked to abrupt glacial climate change. *Nature: Letters* 3:110-113.

Wang, Y. J., H. Cheng, R. L. Edwards, Z. S. An, J. Y. Wu, C. C. Shen, and J. A. Dorale. 2001. A high-resolution absolute-dated late Pleistocene monsoon record from Hulu Cave, China, *Science* 294(5550): 2345-2348.

Wang Y., Cheng, H., Edwards, R.L., He, Y., Kong, X., An, Z., Wu, J., Kelly, M.J., Dykoski, C.A., and X. Li. 2005. The Holocene Asian monsoon: links to solar changes and North Atlantic climate. *Science* 308(5723): 854-857.

Wang, S., J. Huang, Y. He, and Y. Guan. 2014. Combined effects of the Pacific Decadal Oscillation and El Niño-Southern Oscillation on Global Land Dry–Wet Changes, *Sci. Rep*. 4: 6651.

Wang, S. S., W. R. Huang, and H. H. Hsu (2015), Role of the strengthened El Niño teleconnection in the May 2015 floods over the southern Great Plains, *Geophysical Research Letters* 1944-8007.

White, K., G. R. Davidson, and P. Paquin. 2009. Hydrologic evolution of the Edwards Aquifer recharge zone (Balcones fault zone) as recorded in the DNA of eyeless Cicurina cave spiders, south-central Texas, *Geology* 37(4): 339-342.

Wong, C. I., J. L. Banner, and M. Musgrove. 2015. Holocene climate variability in Texas, USA: An integration of existing paleoclimate data and modeling with a new, high-resolution speleothem record, *Quaternary Science Reviews* 127(c): 155–173.

CHAPTER IV

CONCLUSIONS

4.1 Rainfall research conclusions

In Chapter 2, we demonstrated that the isotopic composition of dripwater from Cobbs Cavern is reflective of the isotopic composition of central Texas rainwater, sourced from the Gulf of Mexico, influenced by isotope effects. By comparing our Austin rainwater $\delta^{18}O$ data to other same-day variables, we found a statistically significant relationship connecting the amount of precipitation to the $\delta^{18}O$ of that precipitation. More negative rainwater $\delta^{18}O$ values were indicative of increased precipitation totals, forming a relationship that was strengthened when storms were identified as mesoscale convective systems (MCSs).

Comparing our rainwater $\delta^{18}O$ dataset to air temperature on the day of collection revealed no significant relationship between the two, thus providing no support for central Texas temperature as a major driver of oxygen isotope variability in regional rainwater. The remaining isotope effects, including continentality, altitude, and ice volume, are negligible, and we conclude that the chief driver of oxygen isotope variability in our central Texas rainwater is the amount of precipitation in a particular rain event. After classifying storm type from our collected Austin rainfall, we found that the amount effect is more pronounced in organized storm systems such as MCSs.

Our local meteoric water line (LMWL) results indicate that the Gulf of Mexico is the year-round open ocean source of moisture and that central Texas precipitation does not experience significant recycling of moisture on land. We found a lack of variance in Austin rainwater d-excess values, which further suggests that the vapor source of our rainfall, and

93

evaporative conditions at that source, are similar and consistent throughout the record. We conclude that dripwater from Cobbs Cavern will be representative of meteoric rainwater originating from the Gulf of Mexico.

4.2 Speleothem research conclusions

Our long-term, paleorainfall speleothem record presented in Chapter 3 contributes to a better understanding of the mechanisms driving large-scale rainfall variability in the SGP. We found no evidence of isotope fractionation during calcite formation, which, combined with stable cave temperature and pCO_2 records, led us to conclude that the stalagmite 16CobbB2 likely formed under conditions of isotopic equilibrium. Our conclusions from Chapter 2, with these in-cave results, indicated that $\delta^{18}O$ in cave dripwater thus serves as a direct reflection of rainwater $\delta^{18}O$, which we interpreted as variability in the amount of rainfall reaching the SGP region. This relationship is made stronger when the storm delivering the rainfall is an organized MCS.

Because we cannot fully exclude the potential for prior calcite precipitation or kinetic effects in our speleothem, nor can we use rainwater records as a carbon proxy, controls on the carbon record are less straightforward than they are for the oxygen record. Given limited carbon data resources, we suggest that a combination of biologic factors including vegetation type overlying the karst area (e.g., C3 versus C4 photosynthetic pathways), and soil bioproductivity, are important drivers of $\delta^{13}C$ variability in the speleothem such that more negative $\delta^{13}C$ values are indicative of generally wetter conditions. A negative peak in our speleothem record coincides with MIS 5e, suggesting increased regional moisture availability, or a trend toward C3 vegetation, during this interglacial time.

Our central Texas stalagmite δ^{18}O records regional hydroclimate response to a changing climate. Based on our speleothem-based oxygen isotope record, we conclude that interglacials correspond to wetter conditions in the SGP, and glacials to drier conditions. Our speleothem δ^{18}O variability follows maximum insolation at 30°N from 98-130 kyr BP and 179-209 kyr BP, which indicates Northern Hemisphere (NH) insolation as a probable driver of large changes in our oxygen record, and ultimately, regional large-scale rainfall variability. By comparing MIS 5e (penultimate interglacial) with modern (late Holocene) data, we found that our record provides evidence for increased precipitation regimes, perhaps through more frequent and/or organized MCS storms, under past warming conditions. With the calculated future rise in insolation and predicted anthropogenic warming, our results indicate a wetter SGP into the future if rainfall variability continues to follow the NH insolation curve.

APPENDIX

Table A-1. Uranium and Thorium isotopic compositions and 230Th ages for 16CobbB2 by MC-ICPMS, Thermo Electron Neptune, at NTU.

Sample ID	Weight g	^{238}U ppb[a]	^{232}Th ppt	d^{234}U measured[a]	[^{230}Th/^{238}U] activity[c]	^{230}Th/^{232}Th atomic (x 10^{-6})	Age (yr ago) uncorrected	Age (yr ago) corrected[c,d]	Age (yr BP) relative to 1950 AD	d^{234}U$_{initial}$ corrected[b]
16CobbB-2a-to	0.0614	153.61 ±0.27	16.8 ±7.6	70.2 ±2.0	0.00411 ±0.00018	619 ±279	420 ±18	417 ±18	350 ±18	70.3 ±2.0
16CobbB-2a-1	0.0643	167.17 ±0.41	89.3 ±7.2	83.1 ±3.4	0.02178 ±0.00032	672 ±55	2,215 ±33	2,202 ±34	2,134 ±34	83.6 ±3.4
16CobbB-2a-2	0.0615	200.37 ±0.41	281.3 ±7.6	89.9 ±2.6	0.03191 ±0.00031	375 ±11	3,240 ±33	3,206 ±37	3,138 ±37	90.7 ±2.6
16CobbB-2a-b(	0.0610	218.56 ±0.39	268.6 ±7.6	86.8 ±2.2	0.03878 ±0.00026	520 ±15	3,961 ±28	3,931 ±32	3,864 ±32	87.8 ±2.2
16CobbB-2d-to	0.0649	261.71 ±0.30	17.4 ±7.2	75.2 ±1.3	0.6542 ±0.0013	162008 ±66486	100,699 ±401	100,698 ±401	100,631 ±401	100.0 ±1.8
16CobbB-2d-3	0.0607	205.90 ±0.38	983.5 ±7.9	46.5 ±2.6	0.6672 ±0.0025	2303 ±20	109,460 ±864	109,341 ±865	109,274 ±865	63.4 ±3.5
16CobbB-2d-6	0.0604	178.48 ±0.41	7.6 ±7.7	50.1 ±3.2	0.6915 ±0.0030	267424 ±270028	115,699 ±1118	115,698 ±1118	115,630 ±1118	69.4 ±4.4
16CobbB-2d-5	0.0683	336.23 ±0.50	202.1 ±6.8	63.2 ±1.8	0.7144 ±0.0021	19598 ±662	119,546 ±746	119,531 ±746	119,464 ±746	88.5 ±2.5
16CobbB-2d-7	0.0626	314.49 ±0.45	304.2 ±7.5	61.1 ±2.1	0.7131 ±0.0027	12157 ±302	119,627 ±950	119,603 ±950	119,536 ±950	85.6 ±3.0
16CobbB-2d-1	0.0640	275.72 ±0.51	1044.1 ±7.7	66.9 ±2.5	0.7206 ±0.0027	3138 ±25	120,541 ±987	120,449 ±987	120,382 ±987	94.0 ±3.5
16CobbB-2d-2	0.0670	202.67 ±0.45	198.0 ±7.0	50.1 ±3.2	0.7345 ±0.0027	12397 ±437	129,127 ±1244	129,103 ±1244	129,036 ±1244	72.2 ±4.6
6CobbB-2d-plus	0.0610	195.54 ±0.35	146.4 ±7.6	52.9 ±1.9	0.7381 ±0.0027	16257 ±848	129,586 ±1027	129,568 ±1027	129,501 ±1027	76.3 ±2.7
16CobbB-2d-4	0.0655	206.38 ±0.39	1055.6 ±7.5	63.7 ±2.6	0.8021 ±0.0031	2586 ±20	149,311 ±1502	149,187 ±1501	149,120 ±1501	97.1 ±4.0
6CobbB-2d-plus	0.0621	321.37 ±0.47	7.5 ±7.5	69.5 ±1.6	0.8656 ±0.0028	613464 ±613448	174,640 ±1573	174,639 ±1573	174,572 ±1573	113.7 ±2.7
16CobbB-2d-8	0.0619	231.66 ±0.49	29.2 ±7.5	69.4 ±2.7	0.8803 ±0.0037	115213 ±29603	182,031 ±2365	182,028 ±2365	181,961 ±2365	116.0 ±4.6
16CobbB-2d-b(	0.0728	160.64 ±0.16	116.8 ±6.4	67.3 ±1.3	0.8766 ±0.0019	19882 ±1087	181,175 ±1198	181,157 ±1198	181,091 ±1198	112.3 ±2.3
16CobbB-2e-to|	0.0593	168.88 ±0.29	1973.5 ±8.6	69.2 ±2.1	0.8792 ±0.0031	1240.5 ±6.6	181,529 ±1918	181,252 ±1918	181,185 ±1918	115.5 ±3.6
16CobbB-2e-b(	0.0668	153.16 ±0.20	1.1 ±6.9	59.4 ±1.7	0.9128 ±0.0025	2050847 ±12675399	206,925 ±1998	206,925 ±1998	206,858 ±1998	106.6 ±3.1

Analytical errors are 2s of the mean.

[a] [^{234}U] = [^{235}U] x 137.818 (±0.65‰) (Hiess et al., 2012); d^{234}U = ([^{234}U/^{238}U]$_{activity}$ - 1) x 1000.

[b] d^{234}U$_{initial}$ corrected was calculated based on ^{230}Th age (T), i.e., d^{234}U$_{initial}$ = d^{234}U$_{measured}$ X e^{l234*T}, and T is corrected age.

[c] [^{230}Th/^{238}U]$_{activity}$ = 1 - e^{-l230T} + (d^{234}U$_{measured}$/1000)[l$_{230}$/(l$_{230}$ - l$_{234}$)](1 - e$^{-(l230 - l234)T}$), where T is the age.

Decay constants are 9.1705 x 10^{-6} yr^{-1} for ^{230}Th, 2.8221 x 10^{-6} yr^{-1} for ^{234}U (Cheng et al., 2013), and 1.55125 x 10^{-10} yr^{-1} for ^{238}U (Jaffey et al., 1971).

[d] Age corrections, **relative to chemistry date on October 27th, 2016,** were calculated using an estimated atomic ^{230}Th/^{232}Th ratio of 4 (± 2) x 10^{-6}.

Those are the values for a material at secular equilibrium, with the crustal ^{232}Th/^{238}U value of 3.8. The errors are arbitrarily assumed to be 50%.

Table A-2. Holocene oxygen and carbon isotopic ratios of 16CobbB2, measured on Kiel IV, MAT 253 carbonate device.

Depth	Age Interpolation	Total CO$_2$ (µbar)	Measurement Sample Intensity m44 (mV)	δ^{13}C (‰ VPDB)[a]	δ^{18}O (‰ VPDB)[b]
0.5	350	1153	7102	-6.54	-4.97
1.5	368.02	1092	5439	-6.48	-4.77
2.5	386.04	1231	4288	-6.59	-4.88
3.5	404.06	1173	4268	-6.64	-4.95
4.5	422.08	911	4081	-6.24	-4.88
5.5	440.1	943	4658	-6.35	-4.73
6.5	458.12	924	4388	-6.45	-4.84
7.5	476.14	938	4656	-6.46	-4.84
8.5	494.16	1014	5530	-6.39	-4.77
9.5	512.18	955	4974	-6.27	-4.80
10.5	530.2	1002	5982	-6.09	-4.88
11.5	548.22	1053	7359	-6.04	-4.72
12.5	566.24	936	4480	-5.89	-4.89
13.5	584.26	1021	6540	-5.91	-4.93
14.5	602.28	1024	6552	-5.94	-5.10
15.5	620.3	987	5503	-5.84	-5.05
16.5	638.32	816	2872	-5.75	-4.92
17.5	656.34	973	5230	-5.89	-5.39
18.5	674.36	1043	6421	-5.73	-5.19
19.5	692.38	997	5846	-5.92	-5.11
20.5	710.4	985	5497	-6.06	-5.12
21.5	728.42	1038	6863	-6.01	-5.07
22.5	746.44	1007	6122	-6.21	-5.15
23.5	764.46	1053	7406	-6.27	-5.20
24.5	782.48	982	5371	-6.23	-5.01
25.5	800.5	899	3835	-6.22	-4.84
26.5	818.52	1104	6720	-6.49	-4.97
27.5	836.54	1048	6149	-6.62	-5.05
28.5	854.56	987	4331	-6.61	-5.06
29.5	872.58	1048	7019	-6.68	-5.04
30.5	890.6	1016	6118	-6.65	-5.07
31.5	908.62	999	5707	-6.57	-4.95
32.5	926.64	1043	7343	-6.62	-4.96
33.5	944.66	1009	6821	-6.73	-4.88
34.5	962.68	943	5167	-6.78	-4.84
35.5	980.7	970	5773	-6.69	-4.97

Table A-2 continued.

Depth	Age Interpolation	Total CO$_2$ (μbar)	Measurement Sample Intensity m44 (mV)	δ^{13}C (‰ VPDB)[a]	δ^{18}O (‰ VPDB)[b]
36.5	998.72	1012	5724	-6.72	-4.94
37.5	1016.74	1002	6715	-6.64	-4.97
38.5	1034.76	997	6306	-6.72	-5.27
39.5	1052.78	997	6489	-6.42	-4.86
40.5	1070.8	990	3787	-6.63	-4.87
41.5	1088.82	1058	4836	-6.60	-4.99
42.5	1106.84	1134	6360	-6.60	-5.09
43.5	1124.86	1187	7330	-6.55	-5.01
44.5	1142.88	1058	4797	-6.53	-4.89
45.5	1160.9	1104	4680	-6.65	-4.86
46.5	1178.92	1041	4467	-6.68	-4.90
47.5	1196.94	1136	5545	-5.88	-2.46
48.5	1214.96	1090	5138	-6.67	-4.64
49.5	1232.98	977	3556	-6.35	-4.36
50.5	1251	1175	7415	-6.60	-4.62
51.5	1269.02	1082	5251	-6.85	-4.81
52.5	1287.04	1104	5754	-6.78	-4.86
53.5	1305.06	970	3565	-6.69	-4.88
54.5	1323.08	1026	4291	-6.56	-4.94
55.5	1341.1	1212	6868	-6.48	-4.97
56.5	1359.12	1151	6369	-6.50	-5.04
57.5	1377.14	1202	5824	-6.53	-5.13
58.5	1395.16	1190	5797	-6.48	-5.24
59.5	1413.18	1109	5860	-6.44	-5.07
60.5	1431.2	1212	5869	-6.50	-5.23
61.5	1449.22	1107	5795	-6.33	-5.03
62.5	1467.24	1195	5870	-6.41	-4.85
63.5	1485.26	1134	5815	-6.30	-4.80
64.5	1503.28	1175	4805	-6.34	-4.90
65.5	1521.3	1151	4858	-6.29	-4.98
66.5	1539.32	1209	5753	-6.45	-5.06
67.5	1557.34	1029	4250	-6.33	-4.95
68.5	1575.36	1148	5268	-6.55	-4.90
69.5	1593.38	1092	5761	-6.44	-4.84
70.5	1611.4	1007	5849	-6.47	-4.90
71.5	1629.42	1034	5791	-6.70	-4.89
72.5	1647.44	1051	6620	-6.80	-4.79
73.5	1665.46	929	4542	-6.73	-4.63
74.5	1683.48	1073	5540	-6.86	-4.57
75.5	1701.5	995	6183	-6.78	-4.68
76.5	1719.52	1056	6595	-6.91	-4.74

Table A-2 continued.

Depth	Age Interpolation	Total CO$_2$ (ubar)	Measurement Sample Intensity m44 (mV)	δ^{13}C (‰ VPDB)[a]	δ^{18}O (‰ VPDB)[b]
77.5	1737.54	960	5192	-6.86	-4.67
78.5	1755.56	1014	5443	-6.79	-4.74
79.5	1773.58	1158	7245	-6.76	-4.82
80.5	1791.6	1170	7410	-6.92	-4.90
81.5	1809.62	1175	7460	-6.71	-4.84
82.5	1827.64	1178	7473	-6.80	-4.81
83.5	1845.66	1161	7425	-6.75	-4.82
84.5	1863.68	1178	7302	-6.70	-4.70
85.5	1881.7	1112	6138	-6.59	-4.94
86.5	1899.72	1163	4336	-6.55	-4.87
87.5	1917.74	1168	7387	-6.42	-4.85
88.5	1935.76	1078	5441	-6.45	-4.79
89.5	1953.78	1009	4288	-6.41	-4.89
90.5	1971.8	1131	6657	-6.33	-4.77
91.5	1989.82	1139	6871	-6.31	-4.91
92.5	2007.84	1056	4989	-6.36	-4.88
93.5	2025.86	1048	4822	-6.42	-4.87
94.5	2043.88	1097	5894	-6.41	-4.77
95.5	2061.9	1187	7384	-6.36	-4.89
96.5	2079.92	1183	5944	-6.19	-4.68
97.5	2097.94	1197	7457	-6.30	-4.82
98.5	2115.96	1183	7457	-6.16	-4.78
99.5	2134	1168	7398	-6.36	-4.84
100.5	2145.81	1226	7483	-6.39	-4.86
101.5	2157.62	1187	7419	-6.49	-4.92
102.5	2169.43	1229	7419	-6.51	-4.93
103.5	2181.24	1175	7419	-6.39	-4.86
104.5	2193.05	1075	5419	-6.34	-4.79
105.5	2204.86	1195	4299	-6.40	-4.64
106.5	2216.67	1060	5152	-6.41	-4.55
107.5	2228.48	1151	6716	-6.49	-4.73
108.5	2240.29	1178	7069	-6.47	-4.83
109.5	2252.1	1085	5600	-6.34	-4.93
110.5	2263.91	1134	6907	-6.17	-4.77
111.5	2275.72	1207	7070	-6.08	-4.76
112.5	2287.53	1046	4947	-5.84	-4.53
113.5	2299.34	1095	5927	-6.02	-4.70
114.5	2311.15	1095	5796	-5.99	-4.92
115.5	2322.96	1034	4747	-6.08	-5.10
116.5	2334.77	1161	7066	-6.23	-5.19
117.5	2346.58	1217	7022	-6.33	-5.13

TableA-2 continued.

Depth	Age Interpolation	Total CO_2 (μbar)	Measurement Sample Intensity m44 (mV)	$\delta^{13}C$ (‰ VPDB)[a]	$\delta^{18}O$ (‰ VPDB)[b]
118.5	2358.39	1180	7047	-6.24	-4.95
119.5	2370.2	1021	6018	-6.16	-4.71
120.5	2382.01	995	5470	-5.85	-4.49
121.5	2393.82	1148	7110	-6.25	-4.85
122.5	2405.63	1143	7126	-6.23	-4.83
123.5	2417.44	1141	7051	-6.35	-4.84
124.5	2429.25	1156	7114	-6.36	-4.93
125.5	2441.06	1114	5913	-6.25	-4.78
126.5	2452.87	992	5194	-6.11	-4.69
127.5	2464.68	1009	5704	-6.26	-4.85
128.5	2476.49	1024	6024	-5.94	-4.61
129.5	2488.3	1134	7112	-6.07	-4.66
130.5	2500.11	1185	7067	-5.97	-4.72
131.5	2511.92	1048	6572	-5.83	-4.57
132.5	2523.73	1087	7075	-5.97	-4.61
133.5	2535.54	1070	7026	-6.11	-4.64
134.5	2547.35	1085	5716	-6.15	-4.62
135.5	2559.16	1060	6548	-6.22	-4.68
136.5	2570.97	1163	5862	-6.32	-4.78
137.5	2582.78	1085	7121	-6.32	-4.84
138.5	2594.59	1097	7058	-6.38	-4.89
139.5	2606.4	1151	7159	-6.59	-5.01
140.5	2618.21	1048	6194	-6.53	-4.85
141.5	2630.02	1068	6667	-6.67	-4.89
142.5	2641.83	1161	7067	-6.63	-4.89
143.5	2653.64	1148	5767	-6.55	-5.00
144.5	2665.45	1075	5751	-6.46	-4.87
145.5	2677.26	1170	5705	-6.67	-4.99
146.5	2689.07	1126	6712	-6.39	-4.68
147.5	2700.88	1038	5749	-6.49	-4.92
148.5	2712.69	990	4949	-6.49	-5.02
149.5	2724.5	1100	7089	-6.53	-4.99
150.5	2736.31	1053	6087	-6.56	-4.92
151.5	2748.12	1131	7079	-6.47	-4.91
152.5	2759.93	1146	7094	-6.26	-4.85
153.5	2771.74	1139	7139	-6.35	-4.97
154.5	2783.55	1195	7076	-6.41	-4.96
155.5	2795.36	1187	7064	-6.53	-5.11
156.5	2807.17	1143	5905	-6.40	-4.91
157.5	2818.98	1156	7146	-7.12	-5.30
158.5	2830.79	997	4986	-7.05	-5.38

Table A-2 continued.

Depth	Age Interpolation	Total CO$_2$ (μbar)	Measurement Sample Intensity m44 (mV)	δ^{13}C (‰ VPDB)[a]	δ^{18}O (‰ VPDB)[b]
159.5	2842.6	995	5921	-6.24	-4.77
160.5	2854.41	1038	6906	-6.31	-4.82
161.5	2866.22	1056	7083	-6.34	-4.87
162.5	2878.03	968	5256	-6.35	-4.97
163.5	2889.84	1119	7117	-6.37	-5.18
164.5	2901.65	1053	7081	-6.37	-5.10
165.5	2913.46	1046	5895	-6.46	-5.23
166.5	2925.27	997	5872	-6.52	-5.29
167.5	2937.08	438	952		
168.5	2948.89	604	1663		
169.5	2960.7	1143	6992	-6.49	-4.96
170.5	2972.51	1143	6812	-6.58	-4.96
171.5	2984.32	1136	7109	-6.39	-4.91
172.5	2996.13	1082	7133	-6.23	-4.85
173.5	3007.94	995	5773	-6.20	-4.78
174.5	3019.75	1129	7070	-6.26	-4.80
175.5	3031.56	1146	5974	-6.57	-4.92
176.5	3043.37	953	5066	-6.52	-4.82
177.5	3055.18	1080	7061	-6.58	-4.97
178.5	3066.99	1029	6532	-6.43	-5.07
179.5	3078.8	1043	7071	-6.45	-4.89
180.5	3090.61	1109	7123	-6.61	-4.95
181.5	3102.42	1024	6421	-6.50	-4.59
182.5	3114.23	1129	5925	-6.30	-4.64
183.5	3126.04	1136	5742	-6.42	-4.77
184.5	3138	1109	5924	-6.64	-4.94
185.5	3149.71	1117	7012	-6.79	-5.04
186.5	3161.42	1134	6532	-6.83	-4.80
187.5	3173.13	384	770		
188.5	3184.84	711	2312		
189.5	3196.55	931	4748	-6.90	-4.76
190.5	3208.26	1102	7124	-6.97	-4.68
191.5	3219.97	1070	7131	-7.04	-4.83
192.5	3231.68	1065	7149	-7.09	-4.86
193.5	3243.39	1100	7080	-6.83	-4.70
194.5	3255.1	1143	7159	-6.95	-4.84
195.5	3266.81	1090	7056	-7.14	-5.13
196.5	3278.52	963	5261	-7.10	-5.14
197.5	3290.23	1134	7126	-7.19	-5.23
198.5	3301.94	1070	7117	-7.08	-5.21
199.5	3313.65	816	3043	-6.78	-4.84

Table A-2 continued.

Depth	Age Interpolation	Total CO$_2$ (μbar)	Measurement Sample Intensity m44 (mV)	δ^{13}C (‰ VPDB)[a]	δ^{18}O (‰ VPDB)[b]
200.5	3325.36	1139	6686	-6.85	-5.00
201.5	3337.07	975	4390	-6.84	-5.03
202.5	3348.78	1100	5948	-6.63	-4.85
203.5	3360.49	999	4547	-6.85	-4.93
204.5	3372.2	1087	5365	-7.02	-4.94
205.5	3383.91	929	3642	-7.00	-4.89
206.5	3395.62	1112	4754	-6.89	-4.86
207.5	3407.33	1121	5843	-6.81	-4.76
208.5	3419.04	1085	5698	-6.91	-4.77
209.5	3430.75	1009	4728	-6.97	-4.89
210.5	3442.46	1012	4802	-7.14	-4.80
211.5	3454.17	970	4230	-7.04	-4.78
212.5	3465.88	965	4196	-7.06	-4.73
213.5	3477.59	933	3819	-7.01	-4.93
214.5	3489.3	1043	5401	-7.05	-5.03
215.5	3501.01	1065	5072	-6.95	-5.15
216.5	3512.72	1068	4805	-7.08	-5.28
217.5	3524.43	1170	4910	-6.98	-5.09
218.5	3536.14				
219.5	3547.85	1046	5833	-6.81	-5.24
220.5	3559.56	1053	6832	-6.73	-5.11
221.5	3571.27	965	4859	-6.85	-5.24
222.5	3582.98	1012	5702	-6.88	-5.10
223.5	3594.69	1056	6735	-6.91	-5.03
224.5	3606.4	1114	7092	-6.81	-4.79
225.5	3618.11	1075	7079	-6.79	-4.87
226.5	3629.82	992	5670	-6.78	-5.05
227.5	3641.53	1024	6301	-6.68	-4.94
228.5	3653.24	1026	6819	-7.02	-5.19
229.5	3664.95	1102	7130	-7.13	-5.30
230.5	3676.66	1021	6663	-6.97	-5.06
231.5	3688.37	1131	7147	-6.94	-4.90
232.5	3700.08	943	4265	-7.00	-5.02
233.5	3711.79	1134	7107	-7.14	-5.22
234.5	3723.5	995	5611	-7.21	-5.33
235.5	3735.21	948	4560	-7.02	-5.27
236.5	3746.92	1156	6013	-6.94	-5.08
237.5	3758.63	1195	7120	-7.10	-5.16
238.5	3770.34	995	4852	-7.13	-5.12

[a] ±1σ instrumental uncertainty of ±0.04 ‰ for δ^{13}C for normal-sized (1800 mV to 9000 mV m44 measurement sample

[b] ±1σ instrumental uncertainty of ±0.06 ‰ for δ^{18}O using method above

Table A-3. Combined Pleistocene oxygen and carbon isotopic ratios of 16CobbB2, measured on Kiel IV, MAT 253 carbonate device. Horizontal bar indicates growth hiatus.

Depth	Age Interpolation	Total CO$_2$ (μbar)	Measurement Sample Intensity m44 (mV)	δ^{13}C (‰ VPDB)[a]	δ^{18}O (‰ VPDB)[b]
0.25	99317.264	1070	5908	-8.36	-4.34
0.75	99386.408	1214	4554	-8.26	-4.35
1.25	99455.552	1214	4518	-8.28	-4.46
1.75	99524.696	1131	7098	-8.52	-4.45
2.25	99593.84	1029	5025	-8.72	-4.55
2.75	99662.984	826	2734	-8.16	-4.39
3.25	99732.128	1329	7328	-7.93	-4.61
3.75	99801.272	1207	4297	-7.78	-4.68
4.25	99870.416	1143	6838	-7.99	-4.49
4.75	99939.56	1197	6298	-7.97	-4.44
5.25	100008.704	1124	6886	-7.97	-4.50
5.75	100077.848	1231	4800	-7.92	-4.66
6.25	100146.992	1036	5112	-8.02	-4.75
6.75	100216.136	1148	7349	-7.88	-4.58
7.25	100285.28	1349	7365	-7.80	-4.52
7.75	100354.424	1136	7174	-7.90	-4.50
8.25	100423.568	1060	5506	-7.93	-4.46
8.75	100492.712	1224	4609	-7.98	-4.65
9.25	100561.856	1297	6245	-7.82	-4.55
9.75	100631	1224	4502	-7.77	-4.48
10.25	100700.144	1295	6286	-7.71	-4.44
10.75	100769.288	1263	5385	-8.01	-4.65
11.25	100838.432	1297	6469	-8.24	-4.72
11.75	100907.576	1261	5379	-8.23	-4.64
12.25	100976.72	1341	7392	-8.19	-4.57
12.75	101045.864	1234	4807	-8.27	-4.57
13.25	101115.008	1178	5984	-8.33	-4.46
13.75	101184.152	1295	6224	-8.34	-4.71
14.25	101253.296	1302	6570	-8.42	-4.86
14.75	101322.44	946	3860	-8.30	-4.75
15.25	101391.584	1314	6568	-8.24	-4.78
15.75	101460.728	1336	6215	-8.25	-4.62
16.25	101529.872	1075	5645	-8.23	-4.53
16.75	101599.016	1231	4784	-8.50	-4.84
17.25	101668.16	1185	7333	-8.35	-4.68
17.75	101737.304				
18.25	101806.448	1097	6116	-8.28	-4.52
18.75	101875.592	1310	6734	-8.25	-4.47
19.25	101944.736	1275	5639	-8.20	-4.46
19.75	102013.88	999	4529	-8.17	-4.38
20.25	102083.024	992	4595	-8.31	-4.35
20.75	102152.168	1187	7370	-8.38	-4.40
21.25	102221.312	811	2603	-8.32	-4.51
21.75	102290.456	1258	5387	-8.21	-4.35
22.25	102359.6	970	4234	-7.87	-2.95
22.75	102428.744	963	4067	-8.50	-4.38
23.25	102497.888	758	2222	-8.41	-4.34
23.75	102567.032	1041	5139	-8.45	-4.55
24.25	102636.176	1024	4902	-8.48	-4.65
24.75	102705.32	1112	6311	-8.53	-4.68

Table A-3 continued.

Depth	Age Interpolation	Total CO$_2$ (μbar)	Measurement Sample Intensity m44 (mV)	δ^{13}C (‰ VPDB)[a]	δ^{18}O (‰ VPDB)[b]
25.25	102774.464	951	3973	-8.45	-4.83
25.75	102843.608	1205	4265	-8.38	-4.81
26.25	102912.752	1065	5768	-8.55	-4.74
26.75	102981.896	833	2784	-8.48	-4.74
27.25	103051.04	1214	4511	-8.48	-4.98
27.75	103120.184	802	2509	-8.57	-5.03
28.25	103189.328	819	2663	-8.67	-5.12
28.75	103258.472	1226	4596	-8.67	-4.91
29.25	103327.616	1175	7059	-8.49	-4.79
29.75	103396.76	1097	6381	-8.63	-4.77
30.25	103465.904	1209	4375	-8.61	-4.91
30.75	103535.048	1002	4640	-8.56	-4.69
31.25	103604.192	980	4345	-8.54	-4.75
31.75	103673.336	1007	4674	-8.45	-4.82
32.25	103742.48	1090	6131	-8.55	-4.95
32.75	103811.624	963	4108	-8.57	-4.84
33.25	103880.768	1239	4989	-8.54	-4.98
33.75	103949.912	1021	4913	-8.56	-4.79
34.25	104019.056	1087	6102	-8.57	-4.80
34.75	104088.2	1158	6903	-8.51	-4.66
35.25	104157.344	855	2999	-8.61	-4.69
35.75	104226.488	1270	5491	-8.61	-4.62
36.25	104295.632	1141	7254	-8.58	-4.45
36.75	104364.776	1124	6751	-8.51	-4.37
37.25	104433.92	1087	6065	-8.53	-4.37
37.75	104503.064	1121	6643	-8.56	-4.29
38.25	104572.208	1095	6235	-8.31	-4.20
38.75	104641.352	1222	4377	-8.60	-4.39
39.25	104710.496	1207	4261	-8.66	-4.53
39.75	104779.64	992	4360	-8.63	-4.39
40.25	104848.784	611	1377	-8.63	-4.34
40.75	104917.928	1131	5952	-8.78	-4.52
41.25	104987.072	936	3802	-8.80	-4.80
41.75	105056.216	1029	4932	-8.84	-4.84
42.25	105125.36	1102	6317	-8.54	-4.75
42.75	105194.504	1104	6264	-8.74	-4.81
43.25	105263.648	1180	7346	-8.80	-4.72
43.75	105332.792	1019	4790	-8.74	-4.69
44.25	105401.936	1209	4300	-8.86	-4.86
44.75	105471.08	1043	5185	-8.81	-4.74
45.25	105540.224	819	2710	-8.82	-4.63
45.75	105609.368	1158	6064	-8.91	-4.59
46.25	105678.512	1126	6939	-8.87	-4.42
46.75	105747.656	1129	6884	-8.92	-4.57
47.25	105816.8	1124	6650	-8.99	-4.75
47.75	105885.944	1268	5500	-9.01	-4.82
48.25	105955.088	1200	7342	-8.98	-4.89
48.75	106024.232	1200	7359	-9.01	-4.99
49.25	106093.376	1202	4313	-9.06	-5.20
49.75	106162.52	1131	6932	-8.96	-4.95
50.25	106231.664	1068	5761	-8.95	-4.94
50.75	106300.808	1195	6226	-8.94	-4.85
51.25	106369.952	1253	4468	-8.68	-4.89
51.75	106439.096	1146	5533	-8.82	-4.66
52.25	106508.24	1192	7368	-8.65	-4.62

Table A-3 continued.

Depth	Age Interpolation	Total CO$_2$ (μbar)	Measurement Sample Intensity m44 (mV)	δ^{13}C (‰ VPDB)[a]	δ^{18}O (‰ VPDB)[b]
52.75	106577.384	1295	6253	-8.68	-4.59
53.25	106646.528	1126	6948	-8.73	-4.55
53.75	106715.672	1051	5267	-8.79	-4.58
54.25	106784.816	1185	7397	-8.59	-4.25
54.75	106853.96	1224	4708	-8.97	-4.85
55.25	106923.104	1219	4503	-9.06	-4.96
55.75	106992.248				
56.25	107061.392	1200	7361	-9.12	-4.87
56.75	107130.536	990	4444	-9.02	-4.86
57.25	107199.68	1161	7338	-9.08	-4.92
57.75	107268.824	1143	6022	-9.01	-4.85
58.25	107337.968	1231	4825	-9.22	-4.99
58.75	107407.112	1244	4962	-9.25	-4.99
59.25	107476.256	907	3478	-9.17	-4.81
59.75	107545.4	1126	6298	-9.13	-4.69
60.25	107614.544	1146	5889	-9.20	-4.71
60.75	107683.688	1219	4557	-9.27	-4.82
61.25	107752.832	1205	4308	-9.09	-4.77
61.75	107821.976	1212	4383	-9.08	-4.75
62.25	107891.12	1248	5079	-9.26	-4.74
62.75	107960.264	1112	6587	-9.48	-4.71
63.25	108029.408	1078	5852	-9.73	-4.82
63.75	108098.552	1217	4413	-9.88	-5.10
64.25	108167.696				
64.75	108236.84	1241	4861	-10.17	-5.31
65.25	108305.984	1256	5305	-10.24	-5.31
65.75	108375.128	1236	4855	-10.41	-5.38
66.25	108444.272	1258	5321	-10.53	-5.75
66.75	108513.416	1136	7146	-10.43	-5.86
67.25	108582.56	1158	5940	-10.30	-5.88
67.75	108651.704	1246	5319	-10.20	-6.03
68.25	108720.848	1219	4665	-10.32	-6.18
68.75	108789.992	1209	4452	-10.33	-6.19
69.25	108859.136				
69.75	108928.28	1214	4466	-10.40	-5.87
70.25	108997.424	1292	6318	-10.32	-5.25
70.75	109066.568	1285	6005	-10.26	-5.13
71.25	109135.712	1180	6153	-10.15	-5.28
71.75	109204.856	1151	5909	-9.97	-5.30
72.25	109274	1168	7316	-10.01	-5.30
72.75	109409.23	1241	4995	-10.09	-5.43
73.25	109544.46	1207	4348	-10.14	-5.53
73.75	109679.69	1209	4435	-10.16	-5.54
74.25	109814.92	1129	6975	-10.22	-5.42
74.75	109950.15	1236	4818	-10.27	-5.58
75.25	110085.38	1170	7312	-10.24	-5.45
75.75	110220.61	1139	6826	-10.25	-5.47
76.25	110355.84	1131	6947	-10.20	-5.49
76.75	110491.07	1173	6045	-10.11	-5.43
77.25	110626.3	941	3809	-10.15	-5.50
77.75	110761.53	982	4361	-10.12	-5.49
78.25	110896.76	1043	5235	-10.17	-5.53
78.75	111031.99	1239	4897	-10.33	-5.67
79.25	111167.22	1285	5989	-10.48	-5.78
79.75	111302.45	1270	5553	-10.42	-5.82

Table A-3 continued.

Depth	Age Interpolation	Total CO$_2$ (μbar)	Measurement Sample Intensity m44 (mV)	δ^{13}C (‰ VPDB)[a]	δ^{18}O (‰ VPDB)[b]
80.25	111437.68	1224	4591	-10.42	-5.91
80.75	111572.91	1222	4464	-10.29	-5.79
81.25	111708.14	1082	5863	-10.18	-5.52
81.75	111843.37	1234	4719	-10.17	-5.49
82.25	111978.6	1329	7364	-10.17	-5.33
82.75	112113.83	921	3622	-9.95	-5.01
83.25	112249.06	1195	7391	-9.90	-4.90
83.75	112384.29	1124	6155	-9.56	-5.00
84.25	112519.52	1205	3897	-9.78	-4.88
84.75	112654.75	1053	4797	-9.88	-4.76
85.25	112789.98	1202	3858	-9.86	-4.81
85.75	112925.21	1214	4072	-9.90	-4.75
86.25	113060.44	1139	6514	-10.10	-4.66
86.75	113195.67	1187	7121	-10.20	-4.74
87.25	113330.9	1212	2587	-10.17	-4.88
87.75	113466.13	1163	5152	-10.10	-4.87
88.25	113601.36	1253	5053	-10.26	-4.89
88.75	113736.59	1234	4737	-10.29	-4.89
89.25	113871.82	1136	3858	-10.15	-4.70
89.75	114007.05	1214	4229	-10.29	-4.86
90.25	114142.28	1190	7293	-10.32	-4.73
90.75	114277.51	1229	4499	-10.43	-4.82
91.25	114412.74	1173	7245	-10.55	-4.71
91.75	114547.97	1202	4010	-10.65	-4.74
92.25	114683.2	1222	2706	-10.54	-4.76
92.75	114818.43	1136	3860	-10.25	-4.67
93.25	114953.66	1165	4319	-10.23	-4.66
93.75	115088.89	1165	4796	-10.37	-4.63
94.25	115224.12	1187	4247	-10.34	-4.49
94.75	115359.35	1195	4207	-10.57	-4.48
95.25	115494.58	1246	4816	-10.91	-4.63
95.75	115630	1222	4311	-10.84	-4.72
96.25	115869.625	1195	7279	-10.51	-4.59
96.75	116109.25	1175	7222	-10.62	-4.64
97.25	116348.875	1161	3939	-10.88	-4.83
97.75	116588.5	1134	5986	-10.98	-4.87
98.25	116828.125	1119	5692	-10.96	-4.95
98.75	117067.75	1163	6862	-11.17	-4.96
99.25	117307.375	1141	6268	-11.23	-4.89
99.75	117547	1082	5078	-11.12	-4.89
100.25	117786.625	1080	5115	-11.20	-5.02
100.75	118026.25	1187	7249	-11.30	-5.01
101.25	118265.875	1197	4033	-11.50	-5.10
101.75	118505.5	1148	4497	-11.49	-5.21
102.25	118745.125	1012	4136	-11.39	-5.05
102.75	118984.75	1117	3476	-11.14	-4.81
103.25	119224.375	1214	3925	-11.51	-5.15
103.75	119464	1082	5164	-11.68	-5.24
104.25	119467.6	1151	6728	-11.86	-5.09
104.75	119471.2	1153	6742	-11.85	-5.14
105.25	119474.8	1185	7283	-11.81	-5.17
105.75	119478.4	1087	5316	-11.77	-5.28
106.25	119482	1104	5589	-11.82	-5.24
106.75	119485.6	1036	4421	-11.81	-5.09
107.25	119489.2	941	4294	-11.92	-5.26

Table A-3 continued.

Depth	Age Interpolation	Total CO$_2$ (μbar)	Measurement Sample Intensity m44 (mV)	δ^{13}C (‰ VPDB)[a]	δ^{18}O (‰ VPDB)[b]
107.75	119492.8	1178	4164	-11.81	-5.32
108.25	119496.4	1197	4189	-11.79	-5.21
108.75	119500	1075	4897	-11.88	-5.36
109.25	119503.6	1095	5259	-11.89	-5.28
109.75	119507.2	1217	3913	-11.96	-5.23
110.25	119510.8	1053	4531	-11.98	-5.02
110.75	119514.4	1100	5277	-11.99	-5.08
111.25	119518	1141	6216	-11.96	-5.09
111.75	119521.6	1102	5448	-11.92	-5.14
112.25	119525.2	1031	2581	-11.86	-5.07
112.75	119528.8	1202	3704	-12.04	-5.37
113.25	119532.4	1161	4916	-11.96	-5.17
113.75	119536	1146	3715	-11.98	-5.18
114.25	119571.25	1222	4061	-12.00	-5.55
114.75	119606.5	816	2269	-11.83	-5.39
115.25	119641.75	1153	3989	-11.73	-5.32
115.75	119677	1173	6402	-11.92	-5.18
116.25	119712.25	1161	7038	-11.97	-5.32
116.75	119747.5	1175	7298	-11.89	-5.49
117.25	119782.75	1183	4231	-11.78	-5.35
117.75	119818	1207	3649	-11.88	-5.30
118.25	119853.25	1161	6664	-11.90	-5.03
118.75	119888.5	1185	7077	-11.81	-5.22
119.25	119923.75	1114	5501	-11.76	-5.20
119.75	119959	1185	7293	-11.81	-5.34
120.25	119994.25	1200	6131	-11.72	-5.10
120.75	120029.5	1224	4085	-11.78	-5.12
121.25	120064.75	1163	4056	-11.90	-5.02
121.75	120100	1126	3539	-11.94	-5.10
122.25	120135.25	1031	4316	-11.87	-5.12
122.75	120170.5	1104	3364	-11.96	-5.23
123.25	120205.75	1192	4199	-11.85	-5.24
123.75	120241	1073	4945	-12.01	-5.40
124.25	120276.25	1119	5894	-12.11	-5.46
124.75	120311.5	1209	3827	-12.12	-5.54
125.25	120346.75	1087	5219	-11.98	-5.45
125.75	120382	1134	6191	-11.94	-5.53
126.25	120570.13	1141	6525	-12.04	-5.51
126.75	120758.26	1190	7213	-12.01	-5.74
127.25	120946.39	1151	3984	-12.00	-5.65
127.75	121134.52	1219	4082	-12.18	-5.93
128.25	121322.65	1214	3983	-11.99	-5.98
128.75	121510.78	1263	5063	-12.02	-5.52
129.25	121698.91	1231	4258	-12.08	-5.29
129.75	121887.04	1178	7274	-12.02	-5.25
130.25	122075.17	1236	4387	-12.03	-5.47
130.75	122263.3	1131	6180	-12.02	-5.49
131.25	122451.43	1151	6797	-12.04	-5.45
131.75	122639.56	1178	7231	-12.07	-5.50
132.25	122827.69	1236	2742	-12.06	-5.54
132.75	123015.82	1168	4617	-11.88	-5.57
133.25	123203.95	1234	4396	-12.03	-5.71
133.75	123392.08	1219	4206	-12.06	-5.77
134.25	123580.21	1141	3744	-11.97	-5.46
134.75	123768.34	1100	5615	-11.96	-5.38

Table A-3 continued.

Depth	Age Interpolation	Total CO₂ (μbar)	Measurement Sample Intensity m44 (mV)	δ¹³C (‰ VPDB)[a]	δ¹⁸O (‰ VPDB)[b]
135.25	123956.47	1195	4218	-11.96	-5.30
135.75	124144.6	1092	5325	-11.97	-5.59
136.25	124332.73	1222	4019	-11.95	-5.79
136.75	124520.86	1183	7302	-11.85	-5.68
137.25	124708.99	1192	4249	-11.74	-5.56
137.75	124897.12	1192	4260	-11.66	-5.47
138.25	125085.25	1190	7262	-11.65	-5.46
138.75	125273.38	1046	4316	-11.61	-5.43
139.25	125461.51	1217	3937	-11.73	-5.50
139.75	125649.64	1095	5291	-11.84	-5.40
140.25	125837.77	1192	7259	-11.96	-5.51
140.75	126025.9	1246	4691	-11.94	-5.56
141.25	126214.03	1205	3803	-11.98	-5.66
141.75	126402.16	1168	4558	-11.87	-5.52
142.25	126590.29	1192	5095	-11.84	-5.58
142.75	126778.42	1202	3826	-11.80	-5.63
143.25	126966.55	1165	4149	-11.54	-5.40
143.75	127154.68	1209	3956	-11.01	-5.47
144.25	127342.81	1205	3967	-10.44	-5.50
144.75	127530.94	1200	7308	-10.07	-5.62
145.25	127719.07	1121	5928	-10.31	-5.41
145.4	127907.2	1187	4768	-9.88	-5.67
145.55	128095.33	1058	2915	-10.33	-6.11
145.7	128283.46	1151	3959	-10.50	-6.18
145.85	128471.59	963)	3484	-10.54	-6.12
146	128659.72	1214	3942	-10.49	-6.00
146.15	128847.85	1148	6565	-10.63	-5.86
146.3	129036	1126	6077	-10.70	-5.76
146.45	129045.3	1082	5175	-10.72	-5.54
146.6	129054.6	1180	4288	-10.69	-5.25
146.75	129063.9	1019	4288	-10.62	-5.07
146.9	129073.2	1146	3919	-10.53	-5.00
147.05	129082.5	1024	4285	-10.56	-5.03
147.2	129091.8	1219	4255	-10.64	-5.01
147.35	129101.1	1180	7277	-10.64	-5.02
147.5	129110.4	1173	7288	-10.67	-5.14
147.65	129119.7	1195	4215	-10.60	-5.02
147.8	129129	1219	4407	-10.67	-5.30
147.95	129138.3	1161	4246	-10.60	-5.18
148.1	129147.6	1185	4955	-10.52	-5.23
148.25	129156.9	1109	3597	-10.44	-5.21
148.4	129166.2	1085	4001	-10.39	-5.27
148.55	129175.5	1153	3698	-10.39	-5.26
148.7	129184.8	1143	6926	-10.23	-5.33
148.85	129194.1	794	2141	-10.22	-5.44
149	129203.4	1100	5635	-10.10	-5.43
149.15	129212.7	1073	5159	-9.96	-5.38
149.3	129222	1095	5569	-9.84	-5.35
149.45	129231.3	1104	5761	-9.72	-5.35
149.6	129240.6	1107	5845	-9.54	-5.28
149.75	129249.9	1200	4245	-9.34	-5.04
149.9	129259.2	1053	4886	-9.33	-5.17
150.05	129268.5	1207	4029	-9.44	-5.05
150.2	129277.8	1187	7262	-9.37	-5.03
150.35	129287.1	1104	5850	-9.36	-5.03

108

Table A-3 continued.

Depth	Age Interpolation	Total CO₂ (μbar)	Measurement Sample Intensity m44 (mV)	δ¹³C (‰ VPDB)[a]	δ¹⁸O (‰ VPDB)[b]
150.5	129296.4	1112	5915	-9.38	-4.98
150.65	129305.7	1180	4233	-9.31	-4.82
150.8	129315	1134	3936	-9.27	-4.76
150.95	129324.3	1168	4750	-9.32	-4.90
151.1	129333.6	1190	4271	-9.27	-4.80
151.25	129342.9	1205	2476	-9.34	-4.94
151.4	129352.2	1234	2782	-9.29	-5.00
151.55	129361.5	1251	5006	-9.30	-4.98
151.7	129370.8	1139	6605	-9.22	-4.76
151.85	129380.1	1058	4857	-9.29	-4.71
152	129389.4	1200	7290	-9.30	-4.64
152.15	129398.7	1229	4252	-9.35	-4.74
152.3	129408	1097	5513	-9.30	-4.67
152.45	129417.3	1214	4021	-9.35	-4.69
152.6	129426.6	1183	5198	-9.26	-4.51
152.75	129435.9	1026	4367	-9.28	-4.71
152.9	129445.2	1153	3590	-9.10	-4.57
153.05	129454.5	1151	6863	-9.19	-4.71
153.2	129463.8	1082	5125	-9.24	-4.61
153.35	129473.1	1202	3862	-9.23	-4.69
153.5	129482.4	1058	4736	-9.17	-4.53
153.65	129491.7	1126	5982	-9.19	-4.54
153.8	129501	1185	4359	-9.12	-4.49
169.7	179596	1153	7092	-7.17	-4.63
170.2	179609.67	1060	4760	-6.99	-4.51
170.7	179623.34	1156	5368	-6.99	-4.41
171.2	179637.01	1156	4991	-7.06	-4.50
171.7	179650.68	1200	4667	-7.04	-4.42
172.2	179664.35	875	2659	-7.03	-4.54
172.7	179678.02	1209	3946	-7.16	-4.64
173.2	179691.69	1244	4612	-7.10	-4.66
173.7	179705.36	1205	3894	-7.16	-4.75
174.2	179719.03	1146	6654	-7.18	-4.76
174.7	179732.7	1031	4339	-7.17	-4.78
175.2	179746.37	1170	6760	-7.22	-4.81
175.7	179760.04	1080	5085	-7.19	-4.85
176.2	179773.71	1048	4574	-7.19	-4.81
176.7	179787.38	1146	5292	-7.20	-4.70
177.2	179801.05	1038	4395	-7.20	-4.83
177.7	179814.72	1107	5585	-7.18	-4.79
178.2	179828.39	1131	6017	-7.19	-4.88
178.7	179842.06	1151	6610	-7.17	-4.88
179.2	179855.73	1200	5818	-6.75	-4.47
179.7	179869.4	1224	4243	-7.27	-5.03
180.2	179883.07	1146	6396	-7.25	-5.00
180.7	179896.74	1180	6255	-7.23	-5.10
181.2	179910.41	1173	5863	-7.09	-5.14
181.7	179924.08	1190	5447	-7.08	-5.19
182.2	179937.75	1212	3951	-7.12	-5.26
182.7	179951.42	1170	4845	-7.11	-5.15
183.2	179965.09	1224	4182	-7.20	-5.33
183.7	179978.76	1192	4198	-7.14	-5.15
184.2	179992.43	1161	6892	-7.12	-5.14
184.7	180006.1	1131	6104	-7.11	-5.25
185.2	180019.77	1190	7226	-7.08	-5.30

Depth	Age Interpolation	Total CO$_2$ (µbar)	Measurement Sample Intensity m44 (mV)	δ^{13}C (‰ VPDB)[a]	δ^{18}O (‰ VPDB)[b]
185.7	180033.44	1146	6521	-7.14	-5.34
186.2	180047.11	1109	5754	-7.09	-5.36
186.7	180060.78	1139	6051	-7.12	-5.30
187.2	180074.45	1090	5299	-7.11	-5.24
187.7	180088.12	1102	5267	-7.17	-5.18
188.2	180101.79	1134	6248	-7.14	-5.09
188.7	180115.46	1075	4939	-6.00	-4.08
189.2	180129.13	1187	6779	-7.11	-5.09
189.7	180142.8	1029	4270	-7.14	-5.16
190.2	180156.47	1065	4861	-7.14	-5.26
190.7	180170.14	1170	5669	-7.09	-5.15
191.2	180183.81	1168	5341	-7.12	-5.14
191.7	180197.48	1217	4135	-7.18	-5.31
192.2	180211.15	1134	4642	-7.15	-5.17
192.7	180224.82	1141	4437	-7.08	-5.10
193.2	180238.49	1078	5160	-6.98	-5.11
193.7	180252.16	1085	5115	-6.99	-5.03
194.2	180265.83	1112	5702	-7.01	-4.96
194.7	180279.5	1202	3775	-7.07	-4.97
195.2	180293.17	1168	6863	-7.02	-4.98
195.7	180306.84	1051	4611	-7.01	-5.04
196.2	180320.51	1097	5412	-6.96	-4.91
196.7	180334.18	1217	4001	-6.95	-4.84
197.2	180347.85	1158	5481	-6.97	-4.78
197.7	180361.52	1114	4493	-7.00	-4.83
198.2	180375.19	1219	4102	-7.14	-5.12
198.7	180388.86	1192	5870	-7.01	-4.98
199.2	180402.53	1236	4492	-7.17	-5.22
199.7	180416.2	1187	7145	-7.10	-5.08
200.2	180429.87	1146	6564	-7.09	-5.14
200.7	180443.54	1222	4138	-7.10	-5.14
201.2	180457.21	1187	6085	-7.17	-5.00
201.7	180470.88	1226	4290	-7.29	-5.04
202.2	180484.55	1165	5317	-7.25	-4.67
202.7	180498.22	1178	4924	-7.37	-4.45
203.2	180511.89	1207	3963	-7.50	-4.72
203.7	180525.56	1185	4397	-7.34	-4.57
204.2	180539.23	1131	6283	-7.30	-4.58
204.7	180552.9	1212	3995	-7.35	-4.50
205.2	180566.57	1239	4486	-7.35	-4.43
205.7	180580.24	1246	4660	-7.24	-4.29
206.2	180593.91	1114	5785	-7.12	-4.29
206.7	180607.58	1178	6560	-7.08	-4.21
207.2	180621.25	1200	6034	-7.22	-4.14
207.7	180634.92	1051	4480	-7.39	-4.22
208.2	180648.59	1029	4303	-7.42	-4.22
208.7	180662.26	931	3127	-7.32	-4.25
209.2	180675.93	948	3316	-7.42	-4.31
209.7	180689.6	985	3737	-7.65	-4.44
210.2	180703.27	1043	4509	-7.61	-4.37
210.7	180716.94	760	1817	-7.68	-4.56
211.2	180730.61	1026	4240	-7.64	-4.70
211.7	180744.28	877	2677	-7.48	-4.62
212.2	180757.95	850	2479	-7.31	-4.46
212.7	180771.62	1068	4942	-7.30	-4.46

Table A-3 continued.

Depth	Age Interpolation	Total CO$_2$ (μbar)	Measurement Sample Intensity m44 (mV)	δ^{13}C (‰ VPDB)[a]	δ^{18}O (‰ VPDB)[b]
213.2	180785.29	902	2872	-7.28	-4.43
213.7	180798.96	1014	4099	-7.36	-4.58
214.2	180812.63	1046	4589	-7.39	-4.49
214.7	180826.3	836	2293	-7.43	-4.44
215.2	180839.97	1024	4278	-7.50	-4.42
215.7	180853.64	914	3000	-7.60	-4.35
216.2	180867.31	960	3452	-7.64	-4.32
216.7	180880.98	914	3012	-7.71	-4.29
217.2	180894.65	836	2391	-7.76	-4.28
217.7	180908.32	992	3752	-7.89	-4.52
218.2	180921.99	1004	3947	-7.89	-4.52
218.7	180935.66	782	2021	-7.90	-4.72
219.2	180949.33	1012	4043	-7.86	-4.84
219.7	180963	1046	4536	-7.73	-4.83
220.2	180976.67	887	2735	-7.68	-4.53
220.7	180990.34	489	825	-7.94	-5.00
221.2	181004.01	694	1481	-7.85	-4.73
221.7	181017.68	1090	5357	-7.74	-4.62
222.2	181031.35	1151	6200	-7.56	-4.43
222.7	181045.02	1114	5675	-7.62	-4.39
223.2	181058.69	1131	5358	-7.84	-4.48
223.7	181072.36	1058	4646	-7.95	-4.54
224.2	181086.03	1165	7163	-7.80	-4.45
224.7	181099.7	1095	5381	-7.64	-4.56
225.2	181113.37	1183	7176	-7.45	-4.42
225.7	181127.04	1112	5729	-7.49	-4.34
226.2	181140.71	997	3860	-7.47	-4.29
226.7	181154.38	1161	6001	-7.68	-4.35
227.2	181168.05	1163	5689	-7.78	-4.48
227.7	181181.72	1183	5266	-7.77	-4.46
228.2	181195.39	1153	6913	-7.69	-4.36
228.7	181209.06	1100	5414	-7.50	-4.35
229.2	181222.73	1102	5597	-7.44	-4.37
229.7	181236.4	1043	4521	-7.58	-4.49
230.2	181250.07	1043	4483	-7.66	-4.35
230.7	181263.74	1131	5525	-7.63	-4.22
231.2	181277.41	1104	5061	-7.60	-4.35
231.7	181291.08	1068	4691	-7.74	-4.32
232.2	181304.75				
232.7	181318.42	1109	5753	-7.86	-4.64
233.2	181332.09	1153	6772	-7.68	-4.57
233.7	181345.76				
234.2	181359.43	1161	7157	-7.50	-4.54
234.7	181373.1	1048	4613	-7.52	-4.42
235.2	181386.77	1161	7092	-7.55	-4.35
235.7	181400.44	1114	5872	-7.55	-4.44
236.2	181414.11	47	6477	-7.73	-4.58
236.7	181427.78	1080	5232	-7.86	-4.69
237.2	181441.45	1158	5807	-7.78	-4.67
237.7	181455.12	47	4737	-7.72	-4.59
238.2	181468.79	49	4018	-7.81	-4.66
238.7	181482.46	1043	4496	-7.72	-4.44
239.2	181496.13	1151	6619	-7.80	-4.54
239.7	181509.8	1202	4149	-7.91	-4.41
240.2	181523.47	1190	6929	-7.77	-4.32

Table A-3 continued.

Depth	Age Interpolation	Total CO$_2$ (μbar)	Measurement Sample Intensity m44 (mV)	δ^{13}C (‰ VPDB)[a]	δ^{18}O (‰ VPDB)[b]
240.7	181537.14				
241.2	181550.81	1185	6397	-7.77	-4.45
241.7	181564.48	1153	6001	-7.82	-4.44
242.2	181578.15	1183	5523	-7.97	-4.64
242.7	181591.82				
243.2	181605.49	1024	4185	-7.96	-4.65
243.7	181619.16				
244.2	181632.83	1141	6354	-7.72	-4.26
244.7	181646.5	1205	3850	-7.69	-4.50
245.2	181660.17	1161	6934	-7.63	-4.31
245.7	181673.84	0	5672	-7.67	-4.34
246.2	181687.51	1222	4045	-7.73	-4.53
246.7	181701.18	1226	4279	-7.66	-4.80
247.2	181714.85	1161	6018	-7.60	-4.96
247.7	181728.52	1205	3786	-7.50	-4.82
248.2	181742.19	1158	6927	-7.38	-4.86
248.7	181755.86	1165	7257	-7.27	-4.64
249.2	181769.53	1065	4820	-7.35	-4.77
249.7	181783.2	1114	5696	-7.30	-4.78
250.2	181796.87	1065	4884	-7.26	-4.89
250.7	181810.54	1043	4452	-7.57	-5.35
251.2	181824.21	980	3626	-7.40	-5.02
251.7	181837.88	1197	4183	-7.35	-4.84
252.2	181851.55	1195	4151	-7.16	-4.84
252.7	181865.22				
253.2	181878.89	1139	6742	-7.36	-4.99
253.7	181892.56				
254.2	181906.23	880	2698	-7.38	-4.86
254.7	181919.9	1053	4714	-7.27	-4.77
255.2	181933.57	1175	7275	-7.00	-4.16
255.7	181947.24	1178	7280	-7.19	-4.77
256.2	181960.91	1168	7243	-7.29	-4.80
256.7	181974.58	1173	7056	-7.36	-4.79
257.2	181988.25	1148	6782	-7.47	-4.83
257.7	182001.92	1107	3344	-7.41	-4.64
258.2	182015.59	1087	5335	-7.27	-4.78
258.7	182029.26	1185	7253	-7.36	-5.00
259.2	182042.93	1136	6290	-7.39	-5.17
259.7	182056.6	1139	6479	-7.28	-5.10
260.2	182070.27	1151	6765	-7.31	-5.11
260.7	182083.94	1173	7298	-7.26	-5.20
261.2	182097.61	1151	3838	-7.22	-5.06
261.7	182111.28	1141	3707	-7.23	-5.11
262.2	182124.95	1197	4227	-7.21	-5.03
262.7	182138.62	1139	3798	-7.13	-4.99
263.2	182152.29	1197	4800	-7.25	-5.14
263.7	182165.96	1175	4315	-7.22	-5.10
264.2	182179.63	1095	5479	-7.27	-5.10
264.7	182193.3	1175	7284	-7.26	-5.10
265.2	182206.97	1170	7232	-7.27	-5.09
265.7	182220.64	1202	4047	-7.26	-5.22
266.2	182234.31	1217	4024	-7.18	-5.18
266.7	182247.98	1185	7212	-7.03	-5.07
267.2	182261.65	1214	3888	-7.01	-5.17
267.7	182275.32	1126	5952	-6.92	-5.07

Table A-3 continued.

Depth	Age Interpolation	Total CO$_2$ (μbar)	Measurement Sample Intensity m44 (mV)	δ^{13}C (‰ VPDB)[a]	δ^{18}O (‰ VPDB)[b]
268.2	182289	1109	5725	-6.82	-4.90
268.7	182303.8	892	2790	-6.74	-4.85
269.2	182318.6	1136	6450	-6.63	-4.77
269.7	182333.4	1165	7217	-6.57	-4.74
270.2	182348.2	1175	4197	-6.39	-4.72
270.7	182363	1029	4426	-6.36	-4.76
271.2	182377.8	1175	4162	-6.30	-4.89
271.7	182392.6	1068	5053	-6.35	-5.09
272.2	182407.4	1124	3608	-6.58	-5.14
272.7	182422.2	1143	4575	-6.67	-5.09
273.2	182437	1217	4172	-6.43	-4.85
273.7	182451.8	1222	4236	-6.42	-4.55
274.2	182466.6	1102	5623	-6.54	-4.48
274.7	182481.4				
275.2	182496.2				
275.7	182511	1085	5254	-6.14	-4.45
276.2	182525.8	1158	6915	-6.34	-4.40
276.7	182540.6	1043	4465	-6.78	-4.72
277.2	182555.4	1060	4710	-7.23	-5.05
277.7	182570.2	1197	4197	-7.38	-5.04
278.2	182585	1100	5405	-7.36	-5.00
278.7	182599.8	1102	5369	-7.51	-5.07
279.2	182614.6	1119	5614	-7.63	-5.19
279.95	182629.4	1175	7029	-7.85	-5.19
280.7	182644.2	1153	6453	-7.93	-4.99
281.45	182659	1034	4147	-8.06	-4.95
282.2	182673.8	1163	6614	-8.08	-4.92
282.95	182688.6	0	4999	-8.16	-4.97
283.7	182703.4	1075	4800	-8.36	-5.34
284.45	182718.2	1136	3586	-8.31	-4.93
285.2	182733	1075	2987	-8.23	-4.80
285.95	182747.8	1197	4574	-8.36	-4.81
286.7	182762.6	1102	5416	-8.40	-4.97
287.45	182777.4	1051	4508	-8.48	-4.79
288.2	182792.2	1168	6945	-8.60	-4.85
288.95	182807	1197	7342	-8.49	-4.90
289.7	182821.8	1195	7284	-8.44	-4.64
290.45	182836.6	1207	3724	-8.68	-4.66
291.2	182851.4	1019	4055	-8.82	-4.54
291.95	182866.2	1134	6012	-8.93	-4.62
292.7	182881	1100	5345	-9.23	-4.32
293.45	182895.8	1007	3906	-9.56	-4.15
294.2	182910.6	1163	6929	-9.57	-4.30
294.95	182925.4	1092	5773	-8.62	-4.33
295.7	182940.2	1305	6232	-8.95	-4.22
296.45	182955	1165	7346	-9.33	-3.97
297.2	182969.8	1026	4804	-9.50	-4.07
297.95	182984.6	1226	4534	-9.50	-4.17
298.7	182999.4	1095	5982	-9.62	-4.18
299.45	183014.2	1185	7350	-9.64	-4.32
300.2	183029	1297	5102	-9.78	-4.41
300.95	183043.8				
301.7	183058.6	1183	7363	-9.72	-4.29
302.45	183073.4	1229	4527	-9.79	-4.43
303.2	183088.2	1031	4884	-9.75	-4.36

Table A-3 continued.

Depth	Age Interpolation	Total CO₂ (μbar)	Measurement Sample Intensity m44 (mV)	δ¹³C (‰ VPDB)[a]	δ¹⁸O (‰ VPDB)[b]
303.95	183103	1097	5903	-9.70	-4.33
304.7	183224.2	1048	5062	-9.76	-4.33
305.45	183345.4	1251	4785	-9.82	-4.44
306.2	183466.6	645	1589	-9.68	-4.18
306.95	183587.8	1075	5525	-9.83	-4.47
307.7	183709	1029	4783	-9.74	-4.40
308.45	183830.2	1288	5520	-9.73	-4.51
309.2	183951.4	1244	4687	-9.73	-4.56
309.95	184072.6	1019	4595	-9.67	-4.45
310.7	184193.8	736	1999	-9.50	-4.29
311.45	184315	1346	7257	-9.39	-4.35
312.2	184436.2	1143	6914	-9.17	-4.05
312.95	184557.4	1251	4741	-9.00	-3.84
313.7	184678.6	1095	5804	-8.89	-3.45
314.45	184799.8	1214	4088	-8.96	-3.48
315.2	184921	1239	4522	-8.94	-3.44
315.95	185042.2	1351	5886	-8.76	-3.22
316.7	185163.4	1082	5510	-8.56	-3.17
317.45	185284.6	1185	6895	-8.42	-3.26
318.2	185405.8	1253	4723	-8.26	-3.29
318.95	185527	1141	6201	-8.29	-3.25
319.7	185648.2	1241	4519	-8.44	-3.34
320.45	185769.4				
321.2	185890.6	1200	7330	-8.49	-3.13
321.95	186011.8	1134	6714	-8.88	-3.41
322.7	186133	1183	7356	-9.00	-3.49
323.45	186254.2	1073	5465	-8.93	-3.44
324.2	186375.4	1236	4404	-8.93	-3.48
324.95	186496.6	1209	4037	-8.94	-3.52
325.7	186617.8	1231	4351	-8.99	-3.66
326.45	186739	1158	7352	-8.95	-3.52
327.2	186860.2	1004	4645	-8.99	-3.63
327.95	186981.4	1034	5084	-9.05	-3.65
328.7	187102.6	1234	4726	-8.96	-3.87
329.45	187223.8	1153	6037	-8.67	-3.63
330.2	187345	716	2041	-8.58	-3.61
330.95	187466.2	753	2193	-8.76	-3.51
331.7	187587.4	914	3539	-8.65	-3.35
332.45	187708.6	828	2760	-8.53	-3.26
333.2	187829.8	929	3682	-8.33	-3.16
333.95	187951	907	3383	-8.53	-3.21
334.7	188072.2	1126	6777	-8.59	-3.21
335.45	188193.4	814	2662	-8.73	-3.31
336.2	188314.6	973	4171	-8.81	-3.38
336.95	188435.8	1239	4817	-8.99	-3.60
337.7	188557	1165	7375	-9.00	-3.64
338.45	188678.2	1139	7089	-9.08	-3.95
339.2	188799.4	1087	6051	-9.07	-4.17
339.95	188920.6	1060	5528	-8.99	-4.07
340.7	189041.8	472	960	-8.54	-4.08
341.45	189163	848	2914	-8.70	-4.17
342.2	189284.2	931	3636	-8.65	-4.21
342.95	189405.4	1139	7167	-8.67	-4.15
343.7	189526.6	831	2735	-8.69	-4.09
344.45	189647.8	772	2288	-8.71	-4.21

114

Table A-3 continued.

Depth	Age Interpolation	Total CO$_2$ (μbar)	Measurement Sample Intensity m44 (mV)	δ^{13}C (‰ VPDB)[a]	δ^{18}O (‰ VPDB)[b]
345.2	189769	846	2921	-9.00	-4.19
345.95	189890.2	1080	5722	-8.90	-4.26
346.7	190011.4	1146	7240	-8.78	-4.06
347.45	190132.6	1002	4533	-8.70	-3.79
348.2	190253.8	1246	4911	-8.54	-3.80
348.95	190375	1200	4130	-7.93	-4.32
349.7	190496.2				
350.45	190617.4	907	3318	-7.40	-4.40
351.2	190738.6	872	3054	-7.55	-4.57
351.95	190859.8	1168	7357	-7.64	-4.74
352.7	190981	826	2651	-7.63	-4.81
353.45	191102.2	1261	5133	-7.66	-4.91
354.2	191223.4	1068	5459	-7.47	-4.81
354.95	191344.6	1029	4809	-7.47	-4.96
355.7	191465.8	804	2524	-7.33	-5.15
356.45	191587	1202	4377	-7.24	-5.28
357.2	191708.2	1207	4239	-7.11	-5.19
357.95	191829.4	1109	6415	-7.04	-5.20
358.7	191950.6	1175	7318	-6.79	-5.12
359.45	192071.8	1126	7298	-6.71	-5.17
360.2	192193	1212	4238	-6.82	-5.27
360.95	192314.2	1253	4956	-6.83	-5.20
361.7	192435.4	1104	6141	-6.71	-5.01
362.45	192556.6	1034	4939	-6.64	-4.89
363.2	192677.8	1102	5036	-6.70	-4.90
363.95	192799	1200	7392	-6.73	-4.92
364.7	192920.2	1280	5537	-6.89	-5.06
365.45	193041.4	1263	5091	-7.04	-5.08
366.2	193162.6	1222	4468	-7.10	-5.06
366.95	193283.8	1246	4850	-7.12	-5.08
367.7	193405	1239	4798	-7.20	-5.12
368.45	193526.2	1004	4525	-7.25	-5.08
369.2	193647.4	1134	6788	-7.25	-5.09
369.95	193768.6	1244	4893	-7.30	-5.29
370.7	193889.8	1131	6435	-7.25	-5.12
371.45	194011	1185	7343	-7.23	-5.14
372.2	194132.2	1241	4818	-7.35	-5.27
372.95	194253.4	1236	4708	-7.35	-5.25
373.7	194374.6	1256	5196	-7.26	-4.98
374.45	194495.8	1285	5753	-7.26	-5.02
375.2	194617	1297	6415	-7.19	-4.96
375.95	194738.2	1302	6591	-7.20	-5.01
376.7	194859.4	1205	4289	-7.28	-5.18
377.45	194980.6	1192	7411	-7.32	-5.11
378.2	195101.8	951	4016	-7.36	-5.12
378.95	195223	1175	7350	-7.28	-4.95
379.7	195344.2	1207	4194	-7.38	-5.09
380.45	195465.4	1102	6277	-7.36	-4.99
381.2	195586.6	1180	7341	-7.27	-4.89
381.95	195707.8	1170	7321	-7.27	-4.98
382.7	195829	1219	4477	-7.35	-5.09
383.45	195950.2	1051	5285	-7.42	-5.06
384.2	196071.4	1207	4286	-7.59	-5.20
384.95	196192.6	1222	4509	-7.55	-5.16
385.7	196313.8	1007	4617	-7.43	-5.16

Table A-3 continued.

Depth	Age Interpolation	Total CO$_2$ (μbar)	Measurement Sample Intensity m44 (mV)	δ^{13}C (‰ VPDB)[a]	δ^{18}O (‰ VPDB)[b]
386.45	196435	1109	7400	-7.47	-5.35
387.2	196556.2	1197	7356	-7.46	-5.21
387.95	196677.4	1268	5512	-7.60	-5.32
388.7	196798.6	1236	4915	-7.84	-5.31
389.45	196919.8	391	7321	-7.85	-5.15
390.2	197041	1085	6846	-7.82	-5.24
390.95	197162.2	1085	7344	-7.91	-5.30
391.7	197283.4	577	7362	-8.00	-5.36
392.45	197404.6	531	6944	-8.16	-5.46
393.2	197525.8	259	6286	-8.35	-5.41
393.95	197647	1134	7156	-8.35	-5.43
394.7	197768.2	1126	6907	-8.34	-5.41
395.45	197889.4	1214	4422	-8.47	-5.49
396.2	198010.6	1175	7332	-8.59	-5.53
396.95	198131.8	1183	7354	-8.59	-5.52
397.7	198253	990	6039	-8.29	-5.41
398.45	198374.2	904	7319	-8.42	-5.49
399.2	198495.4	933	5323	-8.45	-5.53
399.95	198616.6	953	6889	-8.44	-5.50
400.7	198737.8	1231	4790	-8.41	-5.43
401.45	198859	1141	7334	-8.35	-5.28
402.2	198980.2	1219	4482	-8.39	-5.40
402.95	199101.4	1165	7327	-8.30	-5.38
403.7	199222.6	1180	7354	-8.32	-5.39
404.45	199343.8	1168	7330	-7.97	-5.19
405.2	199465	1212	4429	-8.58	-5.49
405.95	199586.2	1209	4402	-8.73	-5.43
406.7	199707.4	1214	4440	-8.82	-5.40
407.45	199828.6	1224	4633	-8.91	-5.45
408.2	199949.8	1170	6821	-8.92	-5.07
408.95	200071	1285	5975	-9.08	-4.98
409.7	200192.2	1241	4835	-9.20	-4.95
410.45	200313.4	1236	5485	-9.12	-4.72
411.2	200434.6	1200	7327	-9.14	-4.85
411.95	200555.8	1180	7350	-8.90	-4.78
412.7	200677	1224	4628	-8.58	-4.81
413.45	200798.2	1151	7325	-8.11	-4.63
414.2	200919.4	1209	4323	-7.75	-4.57
414.95	201040.6	1168	7334	-7.74	-4.60
415.7	201161.8	1161	5798	-7.89	-4.65
416.45	201283	1266	5576	-7.87	-4.73
417.2	201404.2	1248	5056	-7.90	-4.61
417.95	201525.4	1173	7385	-7.65	-4.36
418.7	201646.6	1200	7333	-7.50	-4.24
419.45	201767.8	1217	4534	-7.54	-4.39
420.2	201889				
420.95	202010.2	1195	7326	-7.47	-4.25
421.7	202131.4	1222	4826	-7.59	-4.45
422.45	202252.6	1192	7389	-7.54	-4.29
423.2	202373.8	1234	5082	-7.56	-4.40
423.95	202495	1207	4357	-7.71	-4.43
424.7	202616.2	1173	7309	-8.27	-4.59
425.45	202737.4	1170	7363	-8.70	-4.87
426.2	202858.6	1151	7320	-8.84	-4.98
426.95	202979.8	894	7373	-8.90	-5.21

Table A-3 continued.

Depth	Age Interpolation	Total CO$_2$ (μbar)	Measurement Sample Intensity m44 (mV)	δ^{13}C (‰ VPDB)[a]	δ^{18}O (‰ VPDB)[b]
427.7	203101	1200	7377	-8.92	-4.97
428.45	203222.2	1148	7334	-8.97	-5.04
429.2	203343.4	792	7181	-9.09	-5.08
429.95	203464.6	1185	6825	-9.23	-5.08
430.7	203585.8	1021	5530	-9.23	-5.15
431.45	203707	1060	7349	-9.21	-5.16
432.2	203828.2	1234	4815	-9.28	-5.03
432.95	203949.4	1183	7408	-9.27	-5.10
433.7	204070.6	1058	7392	-9.22	-5.13
434.45	204191.8	977	4307	-9.21	-4.96
435.2	204313	977	4280	-9.17	-4.96
435.95	204434.2				
436.7	204555.4	885	3324	-9.23	-5.05
437.45	204676.6	1100	6250	-9.19	-5.10
438.2	204797.8	1187	7109	-9.25	-5.17
438.95	204919	526	2471	-9.27	-5.07
439.7	205040.2	782	6377	-9.25	-4.98
440.45	205161.4	977	4281	-9.30	-4.96
441.2	205282.6				
441.95	205403.8	980	4254	-9.24	-5.28
442.7	205525	828	2722	-9.20	-5.09
443.45	205646.2				
444.2	205767.4	919	3534	-9.29	-5.11
444.95	205888.6	1053	5354	-9.29	-5.15
445.7	206009.8	1009	4656	-9.31	-5.17
446.45	206131	1129	7330	-9.20	-5.02
447.2	206252.2	709	1961	-9.15	-4.97
447.95	206373.4	638	1595	-9.06	-4.86
448.7	206494.6	865	3129	-9.09	-4.96
449.45	206615.8	758	2296	-9.04	-5.07
450.2	206737	655	4473	-9.00	-4.93
450.95	206858	755	2266	-8.98	-5.00
451.7	206979.2	806	2644	-8.93	-4.89
452.45	207100.4	911	3561	-8.91	-4.98
453.2	207221.6				
453.95	207342.8	1087	6580	-9.00	-5.17
454.7	207464	1078	5929	-9.03	-5.11
455.45	207585.2	889	5316	-9.00	-5.07
456.2	207706.4	853	2929	-8.87	-4.92
456.95	207827.6	941	3863	-8.68	-4.93
457.7	207948.8	889	3337	-8.60	-5.01
458.45	208070	999	4609	-8.51	-4.89
459.2	208191.2	850	2904	-8.52	-5.03
459.95	208312.4	750	2235	-8.42	-5.03
460.7	208433.6	741	2162	-8.48	-4.98

[a] ±1σ instrumental uncertainty of ±0.04 ‰ for δ^{13}C for normal-sized (1800 mV to 9000 mV m44 measurement sample intensity) sampleson long-term, replicate (n = 6/day) analyses of the VPDB carbonate isotope standards NBS-19 and IAEA-603

[b] ±1σ instrumental uncertainty of ±0.06 ‰ for δ^{18}O using method above